EVOLUTION OF DEFORMATION TWINS AND DISLOCATIONS NEAR GRAIN BOUNDARIES IN COMMERCIAL PURITY TITANIUM

By

Leyun Wang

A DISSERTATION

Submitted to
Michigan State University
in partial fulfillment of the requirements
for the degree of

DOCTOR OF PHILOSOPHY

Materials Science Engineering

2011

ABSTRACT

EVOLUTION OF DEFORMATION TWINS AND DISLOCATIONS NEAR GRAIN BOUNDARIES IN COMMERCIAL PURITY TITANIUM

By

Leyun Wang

Deformation of bulk polycrystalline materials often results in the development of dislocation slip bands and deformation twins in individual grains. Evolution of deformation microstructures is closely tied to the plasticity and service conditions of the material.   This study employed two modern characterization tools, Electron Backscattered Diffraction (EBSD) and Differential Aperture X-ray Microscopy (DAXM), to study deformation twins and dislocations developed in deformed polycrystalline Ti. Through extensive EBSD characterization, it was found that many $\{10\bar{1}2\}<\bar{1}011>$ T1 twins nucleated from grain boundaries through a slip transfer process: dislocations gliding on a prismatic slip system stimulated twin nucleation in a neighboring grain. This slip transfer twin nucleation mechanism requires a good geometric alignment between the active slip system in one grain and the stimulated twinning system in the neighboring grain, represented by a high slip transfer parameter m'. The value of m' dictates which twinning system will be activated and suggests at which grain boundaries slip-stimulated twin nucleation will occur. Another important scenario for twin nucleation features pairs of twins that are connected with each other at grain boundaries. Statistical analysis of existing examples of paired twins indicates that the two operating twinning systems often have a good geometric alignment (high m'), and at least one of them must have a high Schmid factor. Paired twins are more often observed at low angle grain boundaries than at high angle grain boundaries. This finding was interpreted using the m' rule. DAXM is a non-destructive technique for characterizing

subsurface microstructure, which reveals grain size, grain boundary inclination, and dislocation content. A method that relates the direction of peak streak in Laue patterns with local geometrically necessary dislocations (GNDs) was established. This method was used to analyze residual GNDs near grain boundaries. Combining high-resolution EBSD and DAXM, a

comprehensive study of $\{11\bar{2}1\} < \bar{1}\,\bar{1}\,26 >$ T2 twins was conducted. Most T2 twins nucleated at grain boundaries with one or more tensile twins formed from the same place in the neighboring grain. Significant orientation gradients were observed in some T2 twins. Small T1 twins, transition regions with intermediate orientations, surface ledges, and microcracks were often observed near T2 twin boundaries. <c+a> dislocations, whose Burgers vector belong to the T2 twinning plane, were also identified in the vicinity of some T2 twins. Overall, this work provides new knowledge of microscopic deformation mechanisms in Ti, especially with regard to twinning, which can be incorporated into crystal plasticity constitutive models. In addition, the research methodology developed in this work is beneficial for other metallurgical studies.

ACKNOWLEDGEMENTS

I would like to thank my advisor, Dr. Thomas Bieler, who provided me with the opportunity to perform this work and to present my work in publications and many technical conferences. I will always remember his dedication and enthusiasm in leading me to the right track, from building ambitious but viable research plans, overcoming technical hurdles, to establishing a sound academic attitude. He always encourages me thinking out of the box instead of being constrained by established theories. I am very grateful for his introduction of me to many external institutions and researchers. In addition, I also appreciate the internship opportunity at Max-Planck-Institut für Eisenforschung (MPIE) he arranged for me in the past three summers. (The living expenses during the three visits in Düsseldorf were kindly provided by MPIE.)

Next I would like to thank my co-advisor, Dr. Martin Crimp, for the guidance he gave me throughout the years. Being highly capable and demanding in technical English, he has greatly helped me in most of the published papers I have written and the presentations I have given. Many technical discussions/debates with him inspired me to explore and identify new knowledge that otherwise I would have never thought about. His expertise on electron microscopy is also very helpful for my research work.

I express my gratitude to my thesis committee of Dr. David Grummon, Dr. Donald Morelli, and Dr. Farhang Pourboghrat, for their constructive suggestions in the completion of my degree. I

TABLE OF CONTENTS

LIST OF TABLES

LIST OF FIGURES

Chapter 1

Introduction

Deformation mechanisms at the microscopic scale control the mechanical behavior of metals. More than 70 years ago, three scientists [Orowan (1934), Polanyi (1934), Taylor (1934)] successfully explained metal plasticity using the dislocation gliding mechanism. Researchers later found that many metallurgical phenomena, such as strain hardening, recovery, recrystallization, and high temperature creep, could all be explained by dislocation theories. Apart from dislocations, there is another important microscopic lattice invariant deformation mechanism — deformation twinning, also known as mechanical twinning. It is known that the general deformation of a polycrystal needs five independent deformation systems [Von Mises (1928), Kocks (1970)]. In crystals of low symmetry such as hexagonal metals, the number of available slip systems is limited. As an alternative shear mechanism, twinning provides extra deformation systems that are needed in lower symmetry metals [Hirth et al. (1982), Christian et al. (1995)]. In the past several decades, dislocation slip and twinning have drawn attention from scientists in different disciplines. Physicists use various atomic potentials to study the nucleation and movement of dislocations and twins. Chemists investigate the interaction between dislocations and solute atoms in the solid. Mechanical engineers incorporate slip and twinning into plasticity models. Materials scientists characterize dislocations and twins using different microscopic techniques that enables new theories to be identified that can interpret the observations.

Transmission electron microscopy (TEM) is a well established technique to characterize

dislocations and twins. Variation of diffraction intensity near dislocations and twins provides

contrast for these features to make them visible in the imaging mode [Williams et al. (1996),

Hull et al. (2001)]. The active slip systems for observed dislocations are usually identified by tilt

experiments using the invisibility criterion ($\mathbf{g} \cdot \mathbf{u} = 0$) [Hirsch et al. (1965), Williams et al. (1996)].

Active twinning systems are identified by analyzing diffraction patterns under the selected area

diffraction (SAD) mode. The major disadvantage of TEM is the painstaking sample preparation.

Important features in the original microstructure may be lost during this process. Because the

specimen must be destroyed to make TEM samples, it excludes opportunities for further

investigation. To characterize dislocations and twins more efficiently, alternative techniques

must be used.

In this work, two promising techniques are used: Electron Backscattered Diffraction (EBSD) and

Differential Aperture X-ray Microscopy (DAXM). Both techniques are relatively new:

Commercialized EBSD systems have a history of less than two decades [Dingley et al. (1992),

Adams et al. (1993), Schwarz et al. (2000)]. DAXM was developed in Argonne National Lab

and became open to general users only a few years ago [Larson et al. (2002), Liu et al. (2004)].

For both techniques, dedicated computer software is used to index diffraction patterns and

present useful results. The basic use of these two techniques is to measure crystal orientations in

bulk materials based on Kikuchi patterns (for EBSD) and Laue patterns (for DAXM). However,

other information such as elastic strain, plastic strain, and dislocation density can also be

obtained using these two techniques. In this work, new knowledge of dislocations and twinning

in polycrystalline Ti was gained using EBSD and DAXM. These findings would not have been made without these two techniques.

EBSD is very suitable for analyzing deformation twins in a statistical manner. Twinning in polycrystals has a significant impact on the mechanical properties of the material. Unlike the activation of slip systems, twin nucleation is less dependent on the Schmid law [Capolungo et al. (2009), Beyerlein et al. (2010)]. Researchers are seeking other rules that can account for, or even predict twin nucleation in polycrystals. An orientation map measured by EBSD allows quick identification of the active twinning systems of many twin instances in hundreds of grains, provided that the twins are wide enough. With statistical observation, a slip-stimulated twin nucleation mechanism at grain boundaries was identified. Under this mechanism, twin nucleation seems to be controlled by the magnitude of the slip transfer parameter, m', which describes the alignment between deformation systems in neighboring grain pairs. At the same time, paired twins formed in adjacent grains from the same place at the grain boundary were also noticed. A few crystallographic and geometric rules were identified that can account for the occurrence of most paired twins. These two works demonstrated that in polycrystals twin nucleation depends not only on the orientation of the parent grain, but also on the orientation and deformation history of neighboring grains.

DAXM is a powerful tool to characterize subsurface microstructure and plastic strain. Surface characterization using an electron beam source is convenient, but the microstructure underneath the surface is also important, where there is more constraint by neighboring grains. A few fundamental questions have long puzzled the metallurgy research community: Do boundaries

between two grain pairs of the same orientations, but with different subsurface inclinations behave differently under stress? What is the relationship between surface slip bands and subsurface dislocations left in the grain? These questions cannot be answered without an effective technique to characterize subsurface structure in bulk materials. The high energy synchrotron source and its related DAXM technique provide a means to investigate these questions. In this work, DAXM was used to measure subsurface microstructure in Ti. A theory that relates the peak shape in Laue patterns with the dislocation content in the material will be presented. Using this theory, subsurface geometrically necessary dislocations (GNDs) and their slip systems can be identified. The identified GNDs near grain boundaries and twin boundaries help us understand some important issues in metallurgy such as the formation of in-grain orientation gradients and strain accommodation around deformation twins.

The new knowledge on dislocation activities and twinning in polycrystalline Ti uncovered in this work will be very useful in crystal plasticity, a theory that relates the macroscopic loading response of a polycrystal with the microscopic deformation processes such as slip and twinning. A promising technique is crystal plasticity finite element modeling (CPFEM). By computationally loading a finite element mesh based on the real microstructure, local deformation history (stress, strain, texture, etc.) in the material can be predicted. The accuracy of such prediction depends on the constitutive laws being used, which must capture the real behavior of dislocations and twins in the material. Crystal plasticity will be briefly reviewed in Chapter 2, but it does not belong to the main scope of this thesis.

The outline of this thesis is below. Chapter 2 is for background and literature review. EBSD and DAXM methods are introduced and compared with other diffraction techniques. Common slip and twinning modes in Ti and other hexagonal metals will be shown. The role of twinning in crystal plasticity modeling will also be discussed. Chapter 3 gives the details of all experiments and analysis method involved in this work. Chapter 4 describes how the correlation between slip in one grain and twinning in the neighboring grain was noticed, and how this correlation later leads to a slip-stimulated twin nucleation mechanism. In Chapter 5, formation of twin pairs at grain boundaries, another important source of twin nucleation, will be examined. A set of geometric and crystallographic conditions need to be met for paired twins to form. In Chapter 6, DAXM was used to characterize subsurface grain structure and residual dislocations in bulk Ti samples. The results are compared with surface observations. In Chapter 7, one specific twinning mode in Ti that has received little attention previously is examined in detail with the combination of EBSD and DAXM. Chapter 8 is a brief discussion based on the results. Chapter 9 summarizes this work and future research opportunities will be discussed.

Chapter 2

Background and literature review

2.1 Electron Backscattered Diffraction

2.1.1 EBSD and other diffraction techniques

Most structural materials are polycrystalline metals. Distribution of grain orientations (i.e.

texture) in many ways determines the mechanical as well as other physical and chemical

properties of the material. Traditionally, polycrystal textures are determined by X-ray or neutron

diffraction [Bunge et al. (1982), Kocks et al. (1998)]. In an X-ray diffraction experiment, the

sample is sequentially tilted so that diffraction on a particular crystal plane (e.g. (001) plane)

from all the grains can be recorded. The intensity distribution around a diffraction peak (hkl)

represents the collective distribution of a crystal plane (hkl). The result is often plotted into a

(hkl) pole figure, the stereographic projection of the collective distribution of (hkl) plane normals

in the sample space. With three or more pole figures of different crystal planes, the orientation

distribution function (ODF) that defines the sample texture can be determined by the spherical

harmonic method or other methods [Bunge (1983), Kocks et al. (1998)].

The X-ray method is actually an indirect way to measure textures, and it does not reveal the

spatial distribution of grains, which is critical to many material properties. For example, large

grains could have a different effect on the overall properties if they are clustered or randomly

scattered throughout the material. To determine the spatial distribution of grains, a method that

is also able to measure individual grain orientations is needed. The texture, i.e. the collective

distribution of crystal orientations in a polycrystal, can be easily determined from a table that records the orientation of individual grains. A few diffraction techniques have this ability.

Transmission electron diffraction is capable of measuring grain orientations, but the inconvenience of sample preparation renders the technique unsuitable for extensive measurements. Techniques based on the scanning electron microscope (SEM) are more effective. Three of them will be discussed next: electron channeling patterns (ECP), Kossel X-ray diffraction, and electron backscattered diffraction (EBSD).

Electron channeling patterns were first studied in late 1960s [Coates (1967), Booker et al. (1967)]. In a SEM when the incident beam is near the Bragg condition with respect to a crystallographic plane (hkl), "Kikuchi like" bands (channeling bands) are observed due to the effects of beam scanning or rocking. For example, Figure 2.1 shows ECPs from one grain in a Ti sample. The four patterns were obtained when the sample normal was tilted at 0°, 3°, 9° and 14° from the incident beam. The formation of channeling bands can be interpreted by the superposition of Bloch waves [Hirsch et al. (1965), Schulson (1977), Joy et al. (1982)]. For a channeling band, the two bordering lines correspond to back-scattered electrons (by the (hkl) plane) and forward-scattered electrons (by the $(\bar{h}\,\bar{k}\,\bar{l})$ plane), respectively. Between these two lines, the band is usually brighter than the background due to a negative deviation vector s_g (i.e. deviation from the exact Bragg condition) there. Meanwhile the outside edges of a channeling band, where $s_g > 0$, appear darker. Channeling bands and their intersections (i.e. zone axes) can be indexed in a way similar to the indexing of Kikuchi bands in TEM. The underlying crystal

orientation is determined by comparing the indexed ECP with patterns calculated by computer software [Schmid et al. (1989)]. Although the ECP method is much more convenient than TEM in terms of sample preparation, the analysis process is time-consuming. First, it takes time to set the Bragg condition for the incident beam and a crystal plane in the grain. Second, the angular range of an ECP is about 14° [Dingley et al. (1992)], and it takes much effort to find a low-index zone axis within such a small angular range. Presently, few people use electron channeling patterns to determine grain orientations.

Instead of falling into oblivion, the electron channeling technique has recently been used to observe dislocations and twins in bulk samples [Ng et al. (1998), Ahmed et al. (2006), Gutierrez-Urrutia et al. (2009)]. When the incident beam satisfies the Bragg condition with a crystal (i.e. the beam sits on the edge of a channeling band), the backscattered electron yield is very sensitive to small orientation changes of that plane. Because dislocations disturb the local lattice and plane orientation, variation of backscattered electron intensity near dislocations will be detected in the form of variations in backscattered electron intensity when the beam scans across the surface. When the SEM is switched from diffraction mode to imaging mode, the orientation gradients surrounding these dislocations can be observed from the variations in channeling contrast. This technique is referred to as electron channeling contrast imaging (ECCI). Details can be found in the literature [Simkin et al. (1999), Crimp et al. (2001, 2006)].

Kossel X-ray diffraction uses X-ray photons generated during the interaction between the electron beam of a SEM and the sample surface [Goldstein et al. (2003)]. The X-ray production region occurs up to about 1μm underneath the surface. Bragg diffraction of these X-rays on

crystal planes forms a pair of Kossel cones as shown in Figure 2.2. One diffraction cone (back-scattered) is on the same side as the electron beam, while the other cone (forward-scattered) is on the opposite side. Kossel patterns are recorded on X-ray sensitive films. Indexing Kossel patterns allows grain orientations to be determined. Inokuti and Doherty (1977) once used this technique to study microstructure in iron deformed by rolling. Kossel X-ray diffraction has a high angular resolution of 0.1°, but its popularity suffers heavily from the low spatial resolution (typically 10μm) and poor contrast.
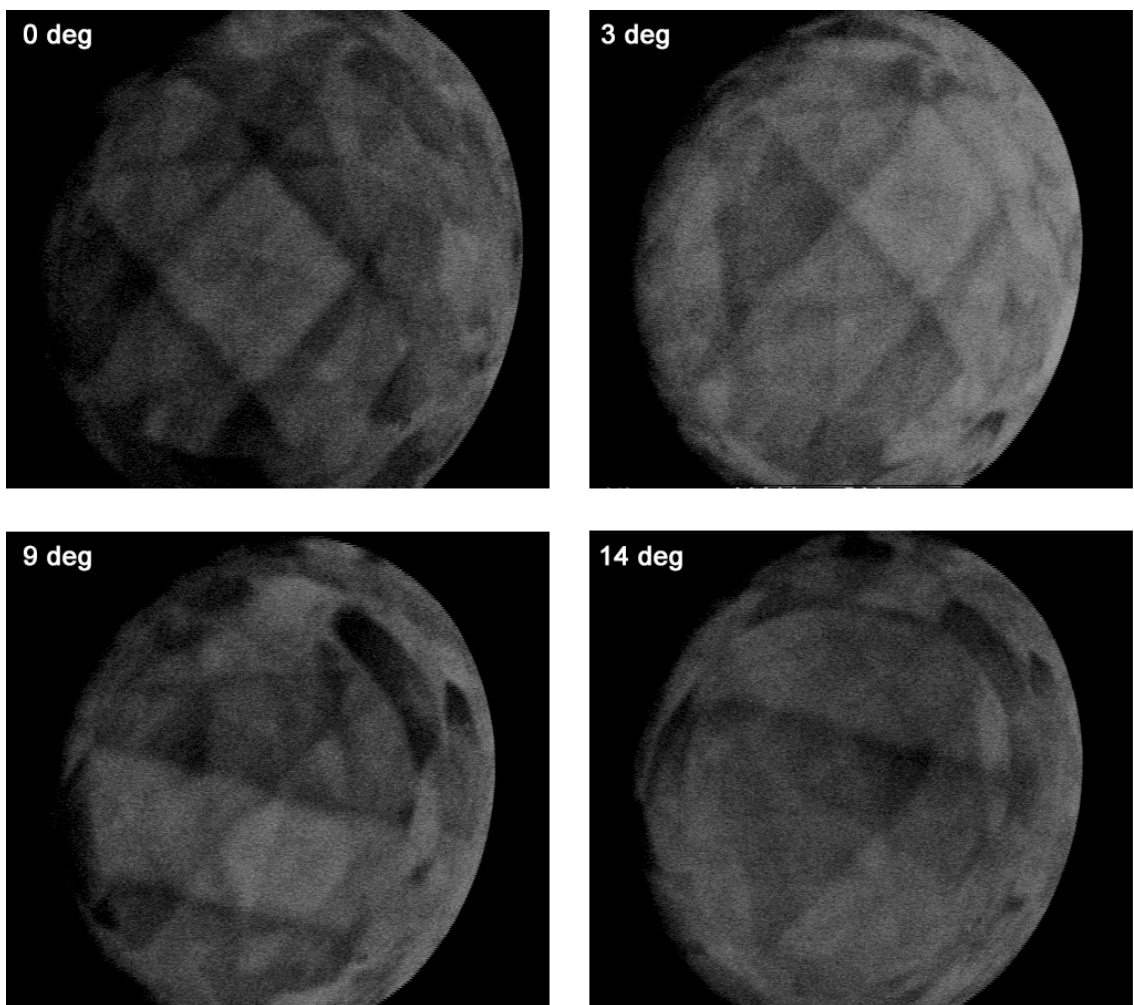
Figure 2.1 Electron channeling patterns from a grain in Ti at different sample tilt angles.
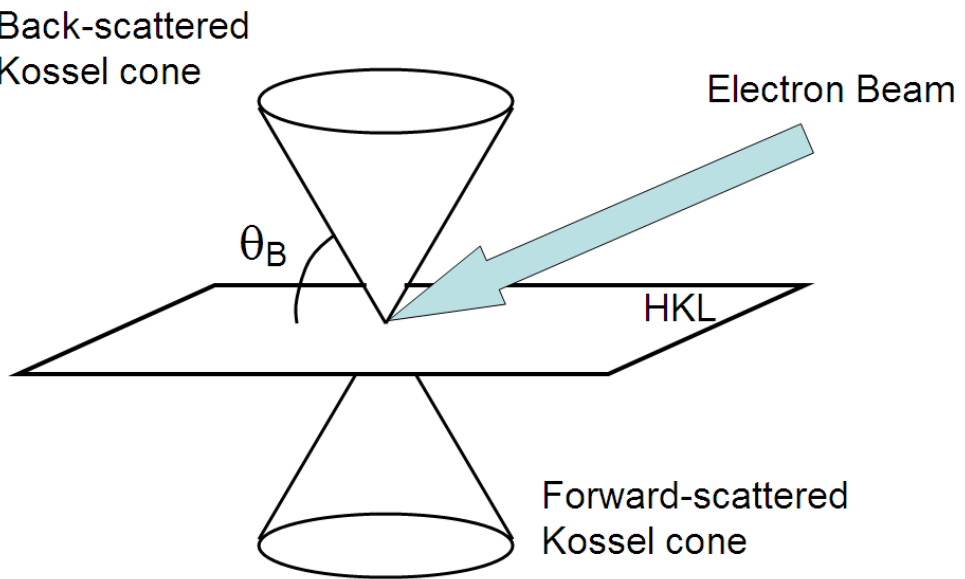
Figure 2.2 Kossel X-ray diffraction and Kossel cones. (For interpretation of the references to color in this and all other figures, the reader is referred to the electronic version of this dissertation.)

Electron backscattered diffraction was first studied by Alam et al. (1954). They observed bands of diffracted electrons when the sample surface normal is at a large angle from the incident beam, which they referred to as "high angle Kikuchi patterns". In the 1970s, Venables and coworkers [Venables et al. (1973, 1977)] obtained these patterns in an SEM and coined the name electron backscattered patterns (EBSP) to describe them. In the 1980s, Dingley and Babakishi (1986) developed an interactive computer system that allows the operator to rapidly index real-time EBSD patterns in the SEM for lattice orientation. The operator manually identified two or more zone axes in the pattern, and then the computer quickly calculated the lattice orientation. This important development laid the foundation for EBSD to later become a technique for rapid orientation determination. Since the beam-sample interaction depth is so small (~ 10nm), the sample surface must be clean and free of strain in order to obtain quality EBSD patterns [Dingley et al. (1992)].

EBSD patterns are essentially Kikuchi patterns. Incident electrons are scattered into all directions once they enter the sample. Some of these scattered electrons will travel at the Bragg angles to certain (hkl) planes and then be Bragg diffracted by these planes. Since the scattered electrons are traveling in all directions, the diffracted beam will lie on one of the two cones known as Kikuchi cones [Goldstein et al. (2003)]. The interception of a pair of Kikuchi cones by photosensitive films or CCD camera screens forms a Kikuchi band (Figure 2.3), and several intersecting Kikuchi bands constitutes a typical EBSD pattern. Although formation of EBSD patterns (Bragg scattering of divergent electrons) is analogous to the formation of Kossel patterns (Bragg scattering of divergent X-rays), the EBSD technique has a much better spatial

resolution (~ 0.2μm) because the scattered electrons come from a much smaller interaction volume around the initial beam-sample interaction point.

Since the late 1990s, commercial EBSD systems have been available, such as OIM^{TM} by EDAX-TSL and HKL Channel 5 by Oxford Instrument [Schwarz et al. (2000)]. Presently, these commercial systems are able to acquire and index hundreds of EBSD patterns per second and solve the underlying crystal orientations concurrently with acquisition [Nowell et al. (2006), Wright et al. (2008), Schwarzer et al. (2010)]. This process can be divided into three steps: (1) detecting Kikuchi bands from the pattern, (2) indexing zone axes, and (3) determining crystal orientation by the positions of identified zone axes.

Kikuchi bands in an EBSD pattern are readily recognized by human eyes. Figure 2.4 shows an EBSD pattern from Fe-1%Si. In the right image, Kikuchi bands are marked by white dashed lines. In the EBSD software, Kikuchi bands are detected by the technique of Hough transformation, a tool for detecting lines in a digital image [Shapiro et al. (2001)]. For any line in a 2D image, there is a unique pair of $(\bar{r}, \bar{\theta})$ corresponding to it: $\bar{r}$ is the distance between the line and the image origin O, $\bar{\theta}$ is the angle between vector $\bar{r}$ and axis OX, as shown in Figure 2.5 (a). The line equation can be written as

$$y = \left(-\frac{\cos\bar{\theta}}{\sin\bar{\theta}} \right) x + \frac{\bar{r}}{\sin\bar{\theta}} \tag{2.1}$$

Rearranging this equation,

$$\bar{r} = x\cos\bar{\theta} + y\sin\bar{\theta} \tag{2.2}$$

13

All lines passing through a point (x_0, y_0) have their corresponding $(\bar{r}, \bar{\theta})$ pairs satisfy the following equation

$$r = x_0 \cos\theta + y_0 \sin\theta \tag{2.3}$$

If x_0, y_0 are constants, then Equation 2.3 is essentially a sinusoidal curve in the $(\mathbf{r}, \boldsymbol{\theta})$ plane (often referred to as Hough space), which is illustrated in Figure 2.5 (b). In Hough space, the sinusoidal curves of collinear points in the image space intersect at the $(\bar{r}, \bar{\theta})$ for that line. For each pixel (x_0, y_0) in an image, the computer determines if there is enough evidence that pixel is on the edge of a line by comparing its intensity with the intensity of neighboring pixels. If so, a sinusoidal curve for that pixel is plotted in Hough space following Equation 2.3. When an EBSD pattern is mapped in this way, each Kikuchi line (edge of a Kikuchi band) will be transformed into a single point that has intensity greater than the background in Hough space. By detecting these "bright points" in Hough space, Kikuchi lines and their positions in the pattern are identified by EBSD software. As a demonstration of Hough transformation, Figure 2.6 shows the Hough transformation results of some simple shapes. Here, the Hough transformation is implemented by a Matlab code. From Figure 2.6, a line in the image space always corresponds to a bright point in the Hough space; an intersection in the image space always corresponds to a dark sinusoidal curve passing these bright points. Hough transformation results for a circle and an ellipse can be easily differentiated from a line, both by human eyes and by a computer.
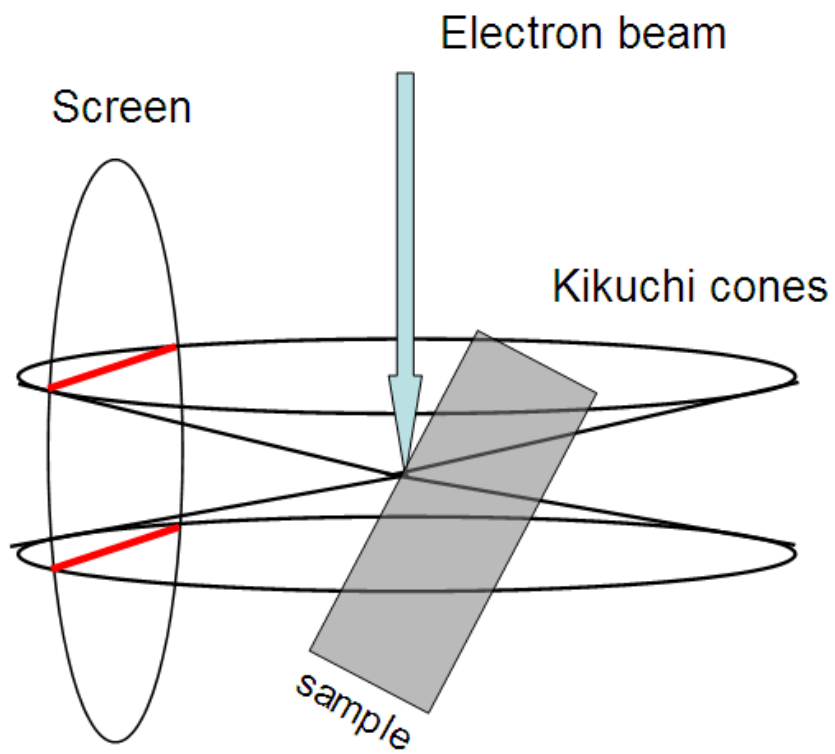
Figure 2.3 Kikuchi cones and Kikuchi bands
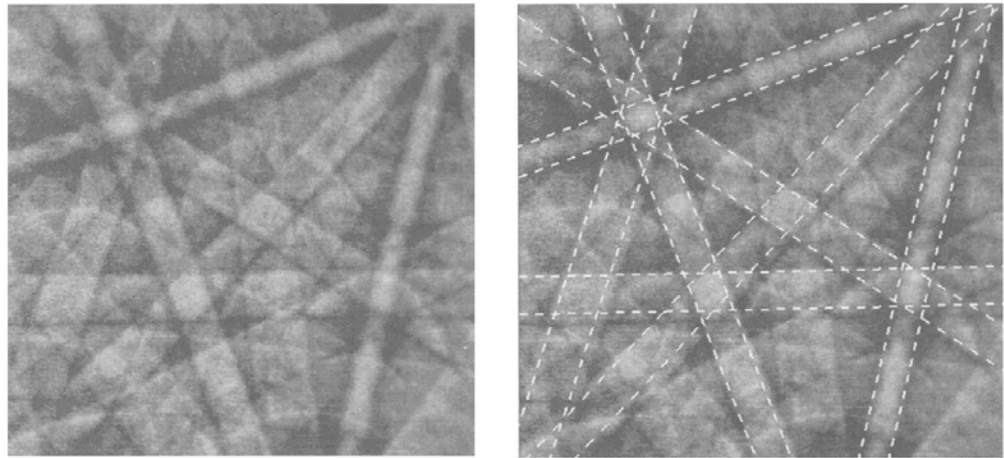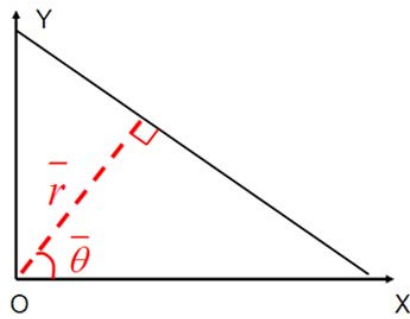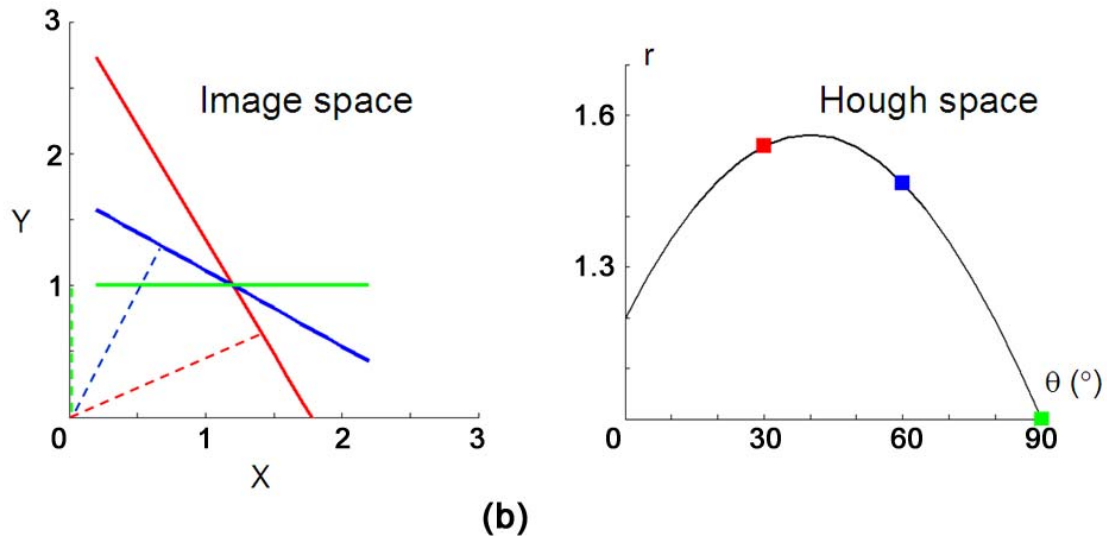
Figure 2.4 An EBSD pattern of Fe-1%Si with Kikuchi bands identified by human eyes

[Adams et al. (1993)]

Figure 2.5 (a) The $(\bar{r}, \bar{\theta})$ pair that corresponds to a line. (b) Lines passing through a point in the image are transformed to points on a sinusoidal curve in Hough space.
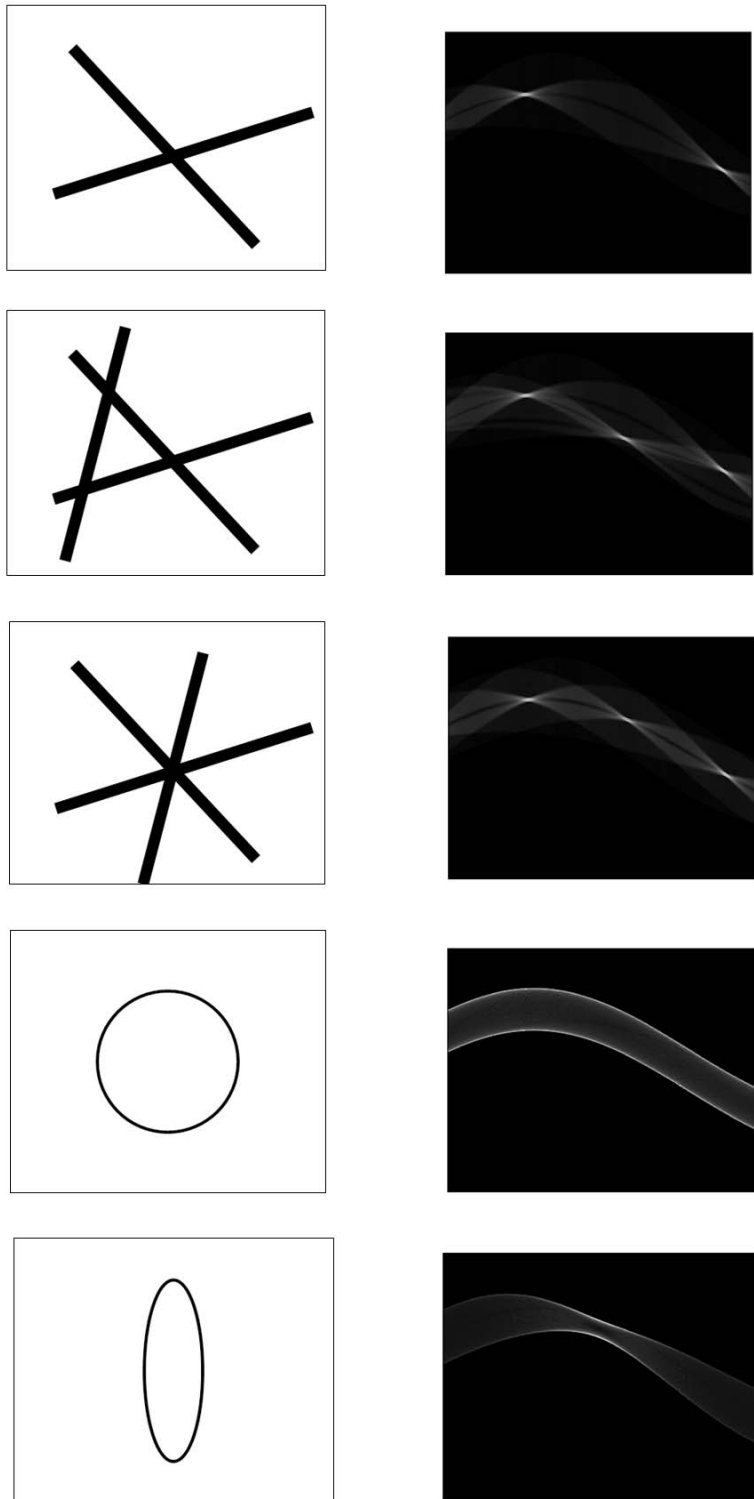
Figure 2.6 Some simple shapes and their Hough transformations

Once Kikuchi bands are identified in an EBSD pattern, zone axes can be located as the intersections of two or more Kikuchi bands. The next step is zone axis indexation. The software measures the mutual angles between three zone axes. The results are compared with a standard set of interzone axes angles for the particular crystal, and the computer searches for all possible combinations of three zone axis indices until a consistent match between experimental and theoretical interzone axes angles is established [Dingley et al. (1992)].

The final step is determining crystal orientation from the indexed zone axes. One technical issue is how to guarantee that the pattern source point in the specimen is at the same height as the pattern center in the phosphor screen. This is done by instrument calibration. Usually a single crystal Si wafer with [001] axis perpendicular to the surface is used. The wafer is mounted in a precision pre-inclined holder such that the beam strikes the specimen at an angle of $70.6° \pm 0.5°$ with respect to the surface normal [Dingley et al. (1992)]. Since the angle between [001] and [114] in pure silicon is $19.4°$, some minor adjustment on the working distance will make the [114] zone axis appear at the exact pattern center. The EBSD system is thus calibrated once the working distance is recorded. This calibrated working distance should be used in all subsequent experiments so that the positions of indexed zone axes in the EBSD pattern can be accurately transformed to crystal directions in the specimen. From this, calculation of the rotation matrix and thus, the crystal orientation is not difficult.

In the EBSD experiment, the electron beam scans across a 2D region from the sample surface by a chosen step size. At each beam step, an EBSD pattern is acquired, indexed, and converted to a crystal orientation as described above. After the experiment, a map of crystal orientations from

the scanned region is obtained. This is the basic idea of orientation imaging microscopy (OIM) [Adams et al. (1993)]. An orientation map by OIM reveals the geometry and orientations of individual grains at the surface of a polycrystal. Many statistical analyses can be performed based on an orientation map, such as texture, grain size distribution, and grain boundary misorientation distribution. The results can be either condensed into a chart or shown directly in a map (e.g. inverse pole figure map, grain boundary misorientation map, etc.). EBSD and its affiliated OIM system have become more and more important in modern metallurgical research.

2.1.2 Orientation representation and OIM

Crystal orientations measured by EBSD must be properly represented. In this section some fundamental concepts in crystallography, including Euler angles, rotation matrix, misorientation, pole figure (PF), and inverse pole figure (IPF) are reviewed.

In OIM, grain orientations are often expressed in Euler angles. The most widely used definition of Euler angles was proposed by Bunge (1983) to describe the rotation operation between the sample coordinate system and the crystal coordinate system. Bunge Euler angles (φ_1, Φ, φ_2) are defined as follows: First, let the Cartesian crystal coordinate system coincide with the sample (lab) coordinate system. The crystal is sequentially rotated by φ_1 around the crystal [001] axis, by Φ around the crystal [100] axis, and then by φ_2 around the crystal [001] axis. In continuum mechanics, a rotation matrix is used to transform vectors and tensors from one coordinate system to another [Reddy (2008)]. The crystal rotation matrix with respect to the sample coordinate system can be calculated from its Euler angles (φ_1, Φ, φ_2) as

20

$$\mathbf{g} = \begin{bmatrix} \cos\varphi_2 & \sin\varphi_2 & 0 \\ -\sin\varphi_2 & \cos\varphi_2 & 0 \\ 0 & 0 & 1 \end{bmatrix} \begin{bmatrix} 1 & 0 & 0 \\ 0 & \cos\Phi & \sin\Phi \\ 0 & -\sin\Phi & \cos\Phi \end{bmatrix} \begin{bmatrix} \cos\varphi_1 & \sin\varphi_1 & 0 \\ -\sin\varphi_1 & \cos\varphi_1 & 0 \\ 0 & 0 & 1 \end{bmatrix} \qquad (2.4)$$

A column vector $\mathbf{v} = \begin{bmatrix} v1 \\ v2 \\ v3 \end{bmatrix}$ defined in the crystal coordinate system (e.g. crystal direction, crystal

plane normal) is transformed into a column vector $\mathbf{V} = \begin{bmatrix} V1 \\ V2 \\ V3 \end{bmatrix}$ defined in the sample coordinate

system by the rotation matrix:

$$\begin{bmatrix} V1 \\ V2 \\ V3 \end{bmatrix} = \mathbf{g}^T \cdot \begin{bmatrix} v1 \\ v2 \\ v3 \end{bmatrix} \qquad (2.5)$$

A 2nd order tensor $\tilde{\mathbf{t}}$ defined in the crystal coordinate system (e.g. elastic strain, dislocation

tensor) is transformed into a 2nd order tensor $\tilde{\mathbf{T}}$ defined in the sample coordinate system by the

rotation matrix:

$$\tilde{\mathbf{T}} = \mathbf{g}^T \cdot \tilde{\mathbf{t}} \cdot \mathbf{g} \qquad (2.6)$$

Given the Euler angles of a grain, the direction of the Burgers vector and the slip plane normal of

any slip system in the sample coordinate system can be calculated using Equations (2.4) and

(2.5). Given the rotation matrix of two grains, $\mathbf{g_A}$ and $\mathbf{g_B}$, the misorientation matrix between

them is

$$\Delta\mathbf{g} = \mathbf{g_B} \cdot \mathbf{g_A^T} \qquad (2.7)$$

The misorientation angle θ and rotation axis **r** between the two grains can be extracted from the misorientation matrix [Kocks et al. (1998)]:

$$\theta = \arccos[\frac{1}{2}(\Delta g_{11} + \Delta g_{22} + \Delta g_{33} - 1)]$$

$$\mathbf{r} = [n_1, n_2, n_3] = \frac{[\Delta g_{23} - \Delta g_{32}, \Delta g_{31} - \Delta g_{13}, \Delta g_{12} - \Delta g_{21}]}{\sqrt{(\Delta g_{23} - \Delta g_{32})^2 + (\Delta g_{31} - \Delta g_{13})^2 + (\Delta g_{12} - \Delta g_{21})^2}}$$

(2.8)

Due to crystalline symmetry, multiple sets of Euler angles can describe the same grain orientation. For hexagonal metals, the following twelve sets of Euler angles are equivalent:

φ_1	Φ	φ_2
φ_1	Φ	$\varphi_2 + 60°$
φ_1	Φ	$\varphi_2 + 120°$
φ_1	Φ	$\varphi_2 + 180°$
φ_1	Φ	$\varphi_2 + 240°$
φ_1	Φ	$\varphi_2 + 300°$
$\varphi_1 + 180°$	$180° - \Phi$	$-\varphi_2$
$\varphi_1 + 180°$	$180° - \Phi$	$60° - \varphi_2$
$\varphi_1 + 180°$	$180° - \Phi$	$120° - \varphi_2$
$\varphi_1 + 180°$	$180° - \Phi$	$180° - \varphi_2$
$\varphi_1 + 180°$	$180° - \Phi$	$240° - \varphi_2$
$\varphi_1 + 180°$	$180° - \Phi$	$300° - \varphi_2$

Out of the 12 sets of Euler angles, the OIM indexing system picks one to represent a crystal orientation.

The orientation distribution is often plotted in the form of pole figures and inverse pole figures. A pole figure is a stereographic plot that shows the distribution of a specified crystal direction in the sample coordinate system. An inverse pole figure is a stereographic plot that shows the distribution of a specified sample reference direction in the crystal coordinate system.

As an example, Figure 2.7 shows a Ti microstructure characterized by OIM. Grain orientations are represented by individual unit cells superimposed on the inverse pole figure map, where each grain is assigned a color based on how a chosen sample direction is oriented in that grain's

crystal coordinate system. In Figure 2.7, grains with their $\{0001\}$, $\{10\bar{1}0\}$, and $\{2\bar{1}\bar{1}0\}$ plane normals (poles) close to the horizontal (labeled as TD) direction have colors tending toward red, blue, and grain, respectively. A $\{0001\}$ pole figure of this region is also shown, where the $\{0001\}$ pole of every grain is plotted in the sample coordinate system (RD-TD-ND). Besides pole figures and inverse pole figures, there are many other methods to represent orientation information in OIM, and will be further explained in later chapters.

2.1.3 Study of orientation gradients by EBSD

Among many applications, the high spatial resolution of EBSD makes it an ideal tool to study in-grain orientation gradients (i.e. inhomogeneous orientation distribution in a single grain, mostly observed after deformation). Development of orientation gradients can have both an intrinsic origin — a positive reorientation field divergence that often leads to grain fragmentation into cell blocks [Raabe et al. (2002)], or an extrinsic origin — influence from neighboring grains that often leads to continuous, long-range lattice rotation from grain boundary to grain interior [Delannay et al. (2003)]. In polycrystals, the latter effect can be pronounced [Mishra et al. (2009)], and it essentially results from the accumulation of dislocations near the grain boundary [Ma et al. (2006a, 2006b)]. The density of accumulated dislocations can be estimated by the measured amount of orientation gradients [Pantleon (2008), Demir et al. (2009), Calcagnotto et

al. (2010)]. Instead of accumulation in front of the grain boundary, sometimes dislocations may pass through the grain boundary and then glide on a slip system in the neighboring grain (i.e. slip transfer). Among many factors, the alignment between the activated slip systems in the two grains is very important for slip transfer (an effective means to reduce local strain energy) to occur. Luster and Morris (1995) proposed a geometric parameter *m'* to measure this alignment. *m'* $= \cos \psi \cdot \cos \kappa$, where ψ is the angle between slip plane normals and κ is the angle between Burgers vectors. High *m'* generally favors slip transfer. The two twin nucleation mechanisms that will be discussed in Chapter 4 and Chapter 5 further extend the concept of slip transfer.
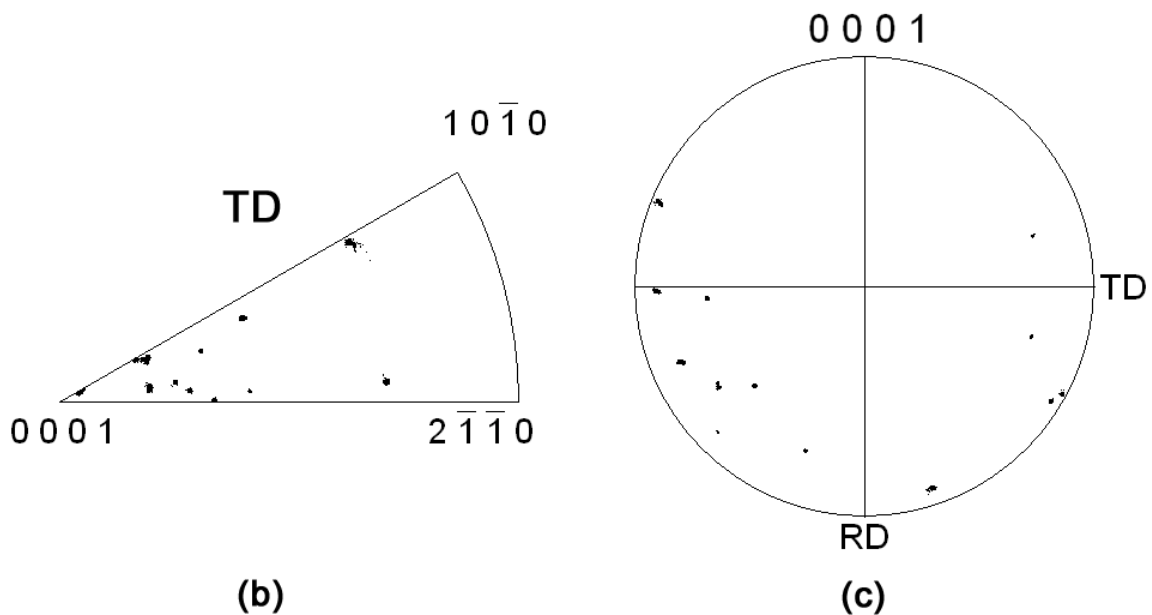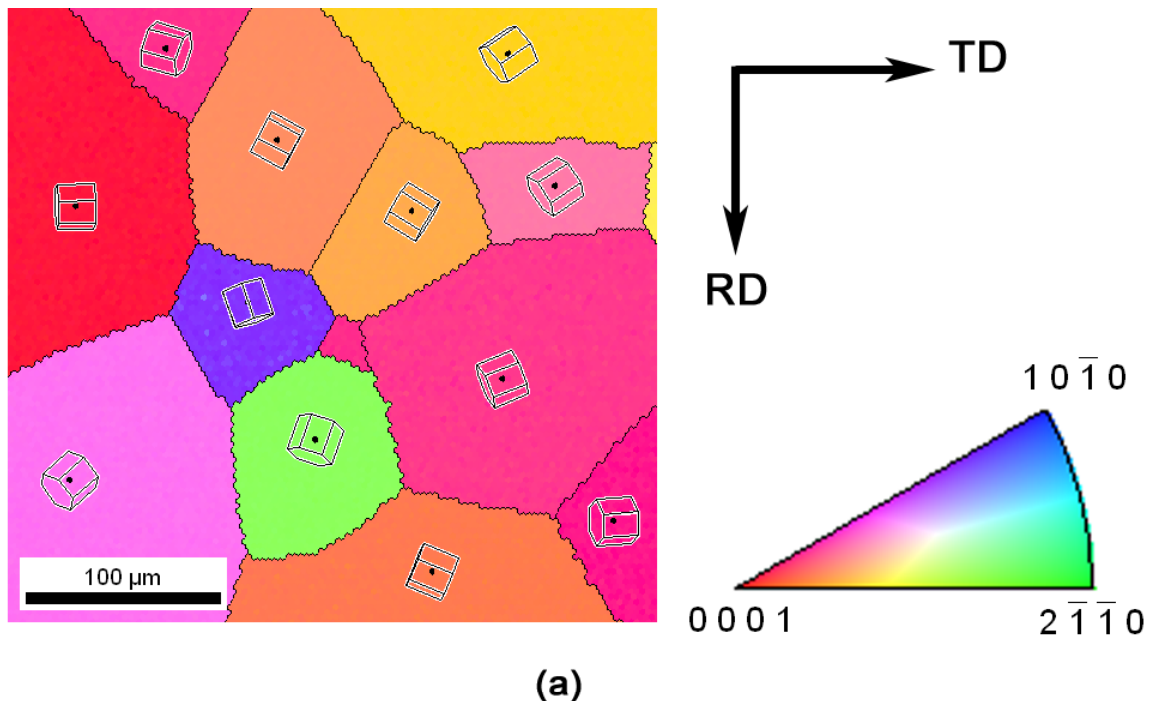
Figure 2.7 (a) A TD inverse pole figure map of a Ti microstructure. (b) TD inverse pole figure. (c) {0001} pole figure.

2.2 Differential Aperture X-ray Microscopy

EBSD and other electron beam techniques only characterize surface microstructure. To characterize subsurface microstructure and its evolution during deformation, a beam source that is more powerful than electron is necessary. The development of the ultra-brilliant third-generation synchrotron X-ray source [Mills (2002)], together with advances in X-ray optics, has created intense polychromatic X-ray microbeam (diameter ~0.5μm) that can penetrate the sample down to several hundred microns beneath the surface [Ice et al. (2007)]. Diffracted X-rays from all the volume elements (voxels) along the beam path are superimposed into a convoluted Laue pattern recorded by a CCD camera. The so-called Differential Aperture X-ray Microscopy (DAXM) is a technique that combines precise mechanical control and image processing to extract point-to-point diffraction information from each voxel along the beam path.

A Pt wire (diameter=50μm) is used as the differential aperture. The beam and the specimen are fixed while the wire traverses stepwise above the sample surface at a height <0.3mm. Laue diffraction patterns are collected on the CCD screen at each step of the wire. After a CCD image with the wire at position (n) has been recorded, the wire is stepped to position (n + 1) where the next CCD image is collected. The source of the differential intensity [I(n) - I(n + 1)] in each pixel of the detector can be uniquely assigned to length segments along the beam using the position of the wire and the position of individual CCD pixels. Figure 2.8 is a simplified demonstration of this scheme. After the wire finishes its traverse, special software is used to extract the "reconstructed" Laue pattern for each voxel along the beam path. That reconstructed Laue pattern (or depth-resolved Laue pattern) represents the diffraction solely from that voxel [Larson et al. (2002), Liu et al. (2004, 2005)]. Each reconstructed Laue pattern is indexed online

by comparing the angle between diffraction peaks in the pattern with an established set of inter-pole angles for that crystal. After that, the crystal orientation of the voxel is determined from the positions of the indexed diffraction peaks in the Laue pattern. These computation procedures are usually completed by powerful computer servers equipped with multiple processers.

In a deformed sample, presence of dislocations leads to both lattice curvature and lattice stretch. Therefore in the reciprocal space, diffraction can happen along directions that do not strictly satisfy the Bragg condition. As a result, Laue patterns often display broadened peaks. The shape of broadened peaks depends on local dislocation content. Larson et al. (2007) demonstrated that the absolute dislocation density tensor can be directly calculated by measuring individual components in the lattice curvature tensor and the strain tensor. Barabash and Ice took a different approach [Barabash et al. (2001, 2003), Ice et al. (2007)]. They noticed that in most cases, peak broadening is unsymmetrical: the peak has an elongated direction ξ and a narrow direction ν. ξ and ν are perpendicular to each other, and both of them are perpendicular to the reciprocal vector **g** of the diffraction plane. They found that the peak width in the narrow direction depends on the total dislocation density, while the peak width in the elongated direction only depends on the unpaired dislocations (geometrically necessary dislocations, GNDs). By numerical calculation, they proposed that a set of edge GNDs having Burgers vector **b**, slip plane normal **n**, and line direction $\tau=\mathbf{b}\times\mathbf{n}$, will cause reflection (hkl) to elongate in direction

$\xi = \dfrac{\tau \times \mathbf{g}_{hkl}}{|\tau \times \mathbf{g}_{hkl}|}$. From the observed peak streak direction, the active slip system in the material can be identified. To date, this method of peak streak analysis has been mostly used for identifying dislocations in cubic materials [Barabash et al. (2001, 2003, 2009), Maass et al. (2007)], and all of these studies use the assumption that the GNDs are of edge type. The

27

accuracy of this peak streak analysis needs further assessment by comparing with results from other characterization methods, such as surface slip band geometry. The assumption of edge GNDs also needs to be evaluated critically.
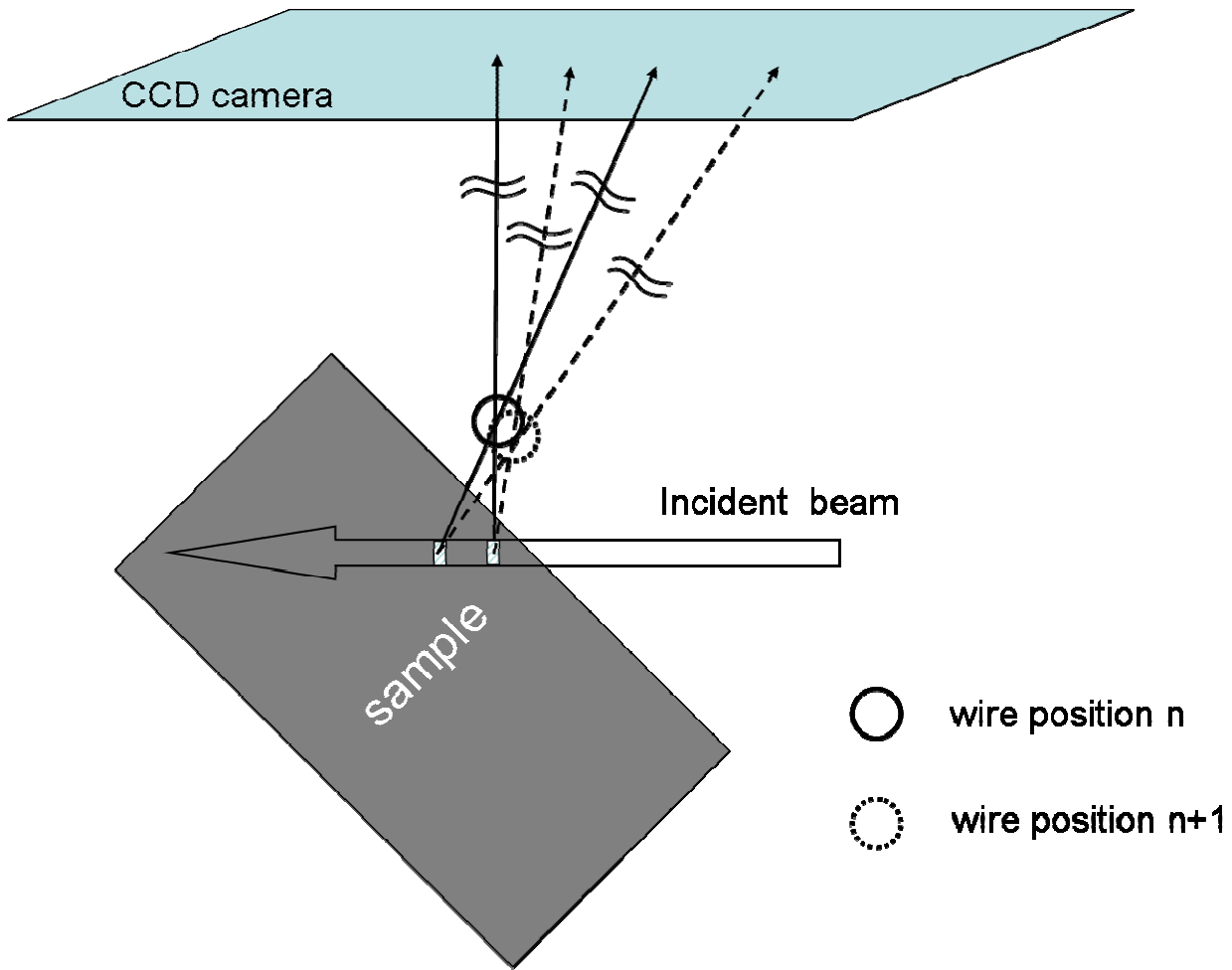
Figure 2.8 A simple scheme of DAXM. The Pt wire move above the sample surface to block a fraction of diffraction from each voxel along the beam path. Depth-resolved Laue pattern from each voxel is later solved by a computer based on the recorded pixel-by-pixel differential intensities at all wire steps.

2.3 Slip and Twinning Modes in Hexagonal Ti

Titanium is a hexagonal metal, whose crystal structure is shown in Figure 2.9. The c/a ratio of pure Ti is 1.588, smaller than Cd (1.886), Zn (1.856), Mg (1.624), Co (1.623), Zr (1.593), but greater than Ru (1.583), Y (1.572), and Be (1.568) [Yoo (1981)]. During plastic deformation, dislocations are formed and glide on different crystal planes. **a** and **c+a** directions in Figure 2.9 are the two most common dislocation Burgers vectors in Ti and other hexagonal metals. At room temperature, four slip modes have been observed in Ti. They are summarized in Figure 2.10. Many studies have shown that the primary slip mode in Ti is $\{10\bar{1}0\} < 1\bar{2}10 >$ prismatic <a> slip [Yoo (1981), Bridier et al. (2005)]. Experiments on high-purity titanium indicated that the critical resolved shear stress (CRSS) for prismatic slip is much lower than that of other slip modes: $\{0001\} < 1\bar{2}10 >$ basal <a> slip, $\{10\bar{1}1\} < 1\bar{2}10 >$ pyramidal <a> slip, and

$\{10\bar{1}1\} < 2\bar{1}\bar{1}3 >$ pyramidal <c+a> slip at room temperature [Tan et al. (1998), Williams et al. (2002), Zaefferer (2003)]. Due to crystal symmetry, each slip mode contains several equivalent variants: 3 for prismatic <a> slip, 3 for basal <a> slip, 6 for pyramidal <a> slip, and 12 for pyramidal <c+a> slip. Many crystal plasticity simulation studies give estimation of CRSS of the different slip modes [Fundenberger et al. (1997), Salem et al. (2005), Wu et al. (2007), Wang L et al. (2011)]. The results vary with each other, and they are listed in Table 2.1.

In polycrystalline Ti, grains with their c-axes nearly perpendicular to the applied uniaxial stress (tensile or compressive) are often referred to as "soft grains" because of their orientation generally ensures a high Schmid factor for one or more of the three prismatic slip systems

[Dunne et al. (2007)]. Such soft grains usually display a single set of distinct prismatic slip bands following deformation. In contrast, "hard grains" have their c-axes nearly parallel to the applied stress, and prismatic slip is difficult to activate due to very low Schmid factors. To accommodate the local strains that develop during the deformation of a polycrystal, hard grains often activate pyramidal <c+a> slip or deformation twinning [Yoo et al. (2002), Salem et al. (2003)].

Table 2.1 CRSS of different slip modes in α-Ti estimated by crystal plasticity simulation

	basal <a> (MPa)	prismatic <a> (MPa)	pyramidal <c+a> (MPa)	pyramidal <a> (MPa)
Fundenberger (1997) (relative values)	3~6	1	6~15	3~6
Salem (2005)	49	37	197	NA
Wu (2007)	150	30	120	NA
Wang (2011)	120	60	180	NA
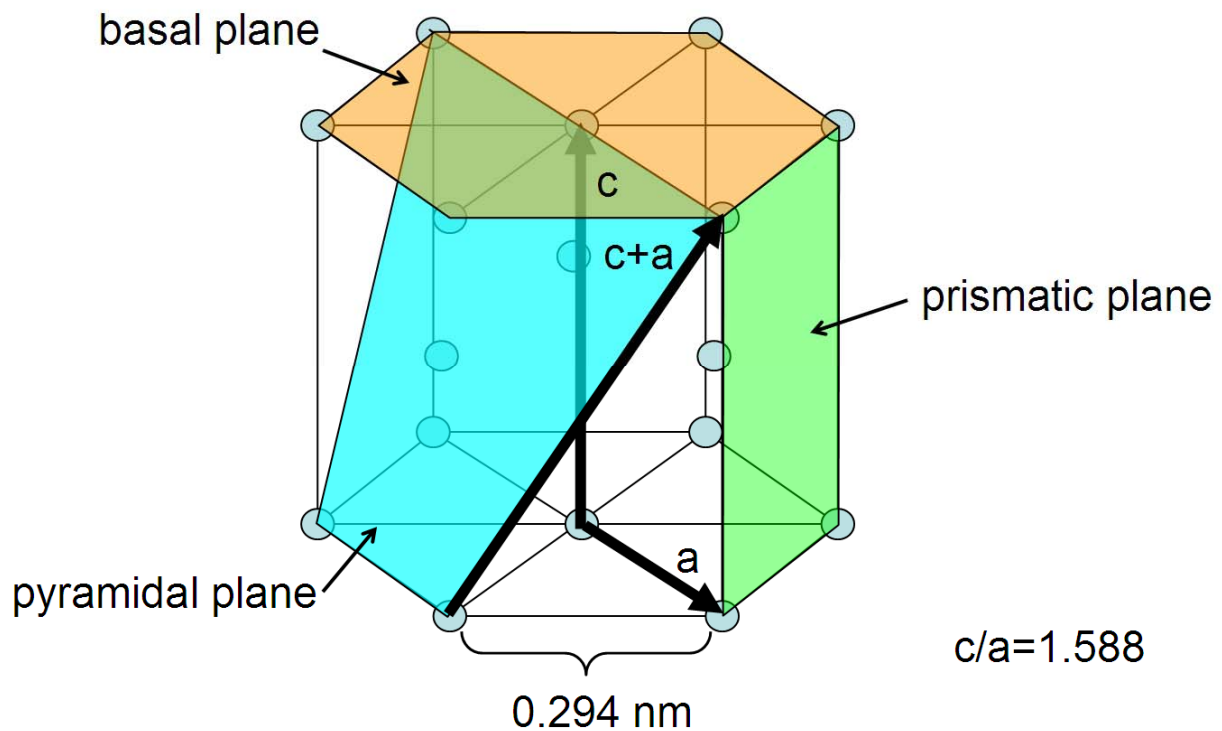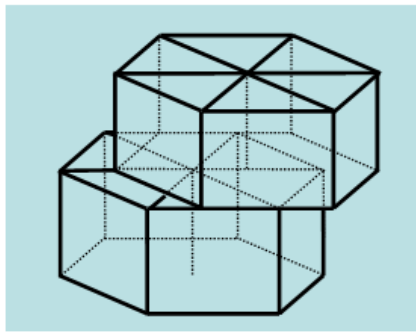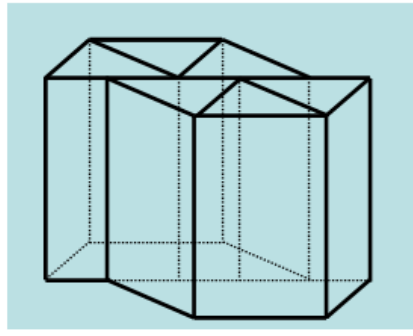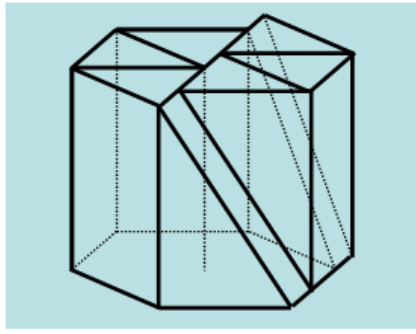
Figure 2.9 Hexagonal lattice of Ti with some important crystal directions and crystal planes.
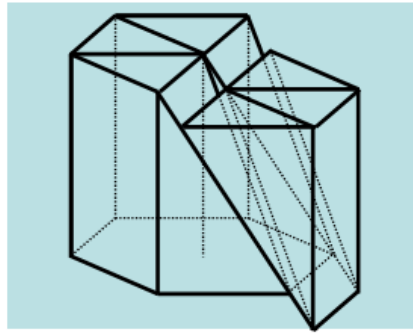
Figure 2.10 Four slip modes have been commonly observed in Ti at room temperature. Their slip planes and slip directions are shown here.

Apart from dislocation slip, twinning is another important microscopic deformation mechanism for metals. It happens when part of the atoms in the crystal lattice shear on a certain crystal plane (K1) along a certain direction (η1). The K1 plane is called the twinning plane, and it will become the symmetrical plane between the sheared part (twin) and the unsheared part (matrix, or parent grain). η1 is called the twinning direction. Besides K1, there is another undistorted plane (K2, conjugate twinning plane) after twinning. The normals of K1 and K2 define the plane of shear, denoted by P, and the intersection of K2 and P is the conjugate twinning direction η2. Figure 2.11 summarizes the four twinning elements K1, η1, K2, and η2. A particular twinning mode in the lattice is defined when K1 and η2 (K2 and η1) are fixed, but more often all the four twinning elements are specified along with the scalar magnitude s of the shear [Christian et al. (1995)].

Twins are more frequently observed in hexagonal metals than in cubic metals because of the lower symmetry of the former. To a large extent, the c/a ratio (γ) of a hexagonal metal determines what kinds of twinning modes will exist in that metal. Table 2.2 lists the four twinning modes that have been observed in Ti. T1 and T2 refer to tensile or extension twinning, because generally these two twinning modes can be activated only in such grains that have their c-axis strained in tension. Similarly, C1 and C2 refer to compressive or contraction twinning. The twinning shear, s, depends on γ and its value can be calculated for each twinning mode using the equations in Table 2.2. Figure 2.12 summarizes all four twinning modes, including the twinning plane and twinning direction of each mode. At room temperature, T1

($\{10\bar{1}2\} < \bar{1}011 >$) is the most frequently observed twinning mode in Ti and other hexagonal

metals with similar c/a ratio, such as Mg and Zr [Song et al. (1995a, 1995b), Bingert et al. (2002), Stanford et al. (2008a), Beyerlein et al. (2010b)]. The lattice relationship between the matrix and a T1 twin is often represented in a $<1\bar{2}10>$ projection plot, such as in Figure 2.13. The matrix lattice and the twin lattice are symmetrical around the $(10\bar{1}2)$ twinning plane. The twinning dislocation of T1 ($\mathbf{b_{T1}}$) is so called zonal dislocation because it spreads on four consecutive $(10\bar{1}2)$ planes. Propagation of twinning dislocations on the twinning plane and subsequent "atomic shuffling" (not shown in the figure) transform the matrix lattice into the twin lattice [Christian et al. (1995)].

Though less frequent than T1 twins, T2 twins ($\{11\bar{2}1\}<\bar{1}\bar{1}26>$) were also observed in many hexagonal metals, such as Co [Vaidya et al. (1980)], Zr [Bhattacharyya et al. (2009), Capolungo et al. (2009b)], Ti [Stanford et al. (2008a), Bozzolo et al. (2010)], and a Mg-based alloy [Stanford (2008b)]. The atomic projection for T2 twinning is also shown in Figure 2.13. The twinning dislocation of T2 ($\mathbf{b_{T2}}$) spreads on two consecutive $(11\bar{2}1)$ planes. The large shear of T2 twins makes them potential damage nucleation sites in the material. Vaidya and Mahajan examined T2 twins in Co by identifying dislocations near the twin boundary with transmission electron microscopy (TEM), and pointed out that the accommodation and formation of T2 twins were accompanied by <c+a> dislocations gliding on the T2 twinning plane. Other than this paper, there are few works investigating T2 twinning.

Table 2.2 Deformation twinning modes in Ti

Mode	K1	η1	K2	η2	s	Misorientation*
T1	$\{10\bar{1}2\}$	$<\bar{1}011>$	$\{\bar{1}012\}$	$<10\bar{1}1>$	$\dfrac{\gamma^2-3}{\sqrt{3}\gamma}=0.174$	85°
T2	$\{11\bar{2}1\}$	$<\bar{1}\bar{1}26>$	$\{0001\}$	$<11\bar{2}0>$	$\dfrac{1}{\gamma}=0.630$	35°
C1	$\{11\bar{2}2\}$	$<11\bar{2}3>$	$\{11\bar{2}4\}$	$<22\bar{4}3>$	$\dfrac{2(\gamma^2-2)}{3\gamma}=0.219$	65°
C2	$\{10\bar{1}1\}$	$<10\bar{1}\bar{2}>$	$\{10\bar{1}3\}$	$<30\bar{3}2>$	$\dfrac{4\gamma^2-9}{4\sqrt{3}\gamma}=0.099$	54°

T: Tensile; C: Compressive

* Angle between the c-axes of the matrix and the twin
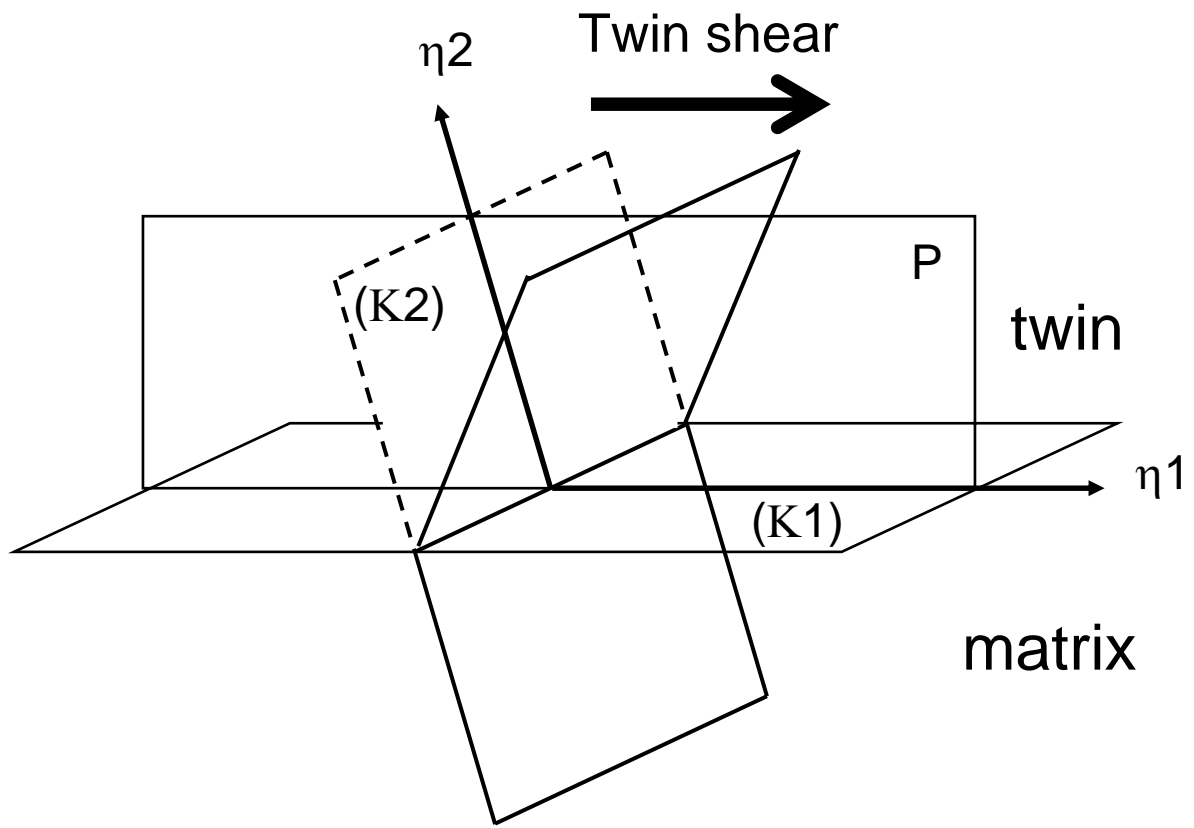
Figure 2.11 The four twinning elements: K1 (twinning plane), K2 (conjugate twinning plane), η1 (twinning direction), and η2 (conjugate twinning direction).

Tensile

(T1)

$\{10\bar{1}2\}<\bar{1}011>$

(T2)

$\{11\bar{2}1\}<\bar{1}\bar{1}26>$

Compressive

(C1)

$\{11\bar{2}2\}<11\bar{2}\bar{3}>$

(C2)

$\{10\bar{1}1\}<10\bar{1}\bar{2}>$
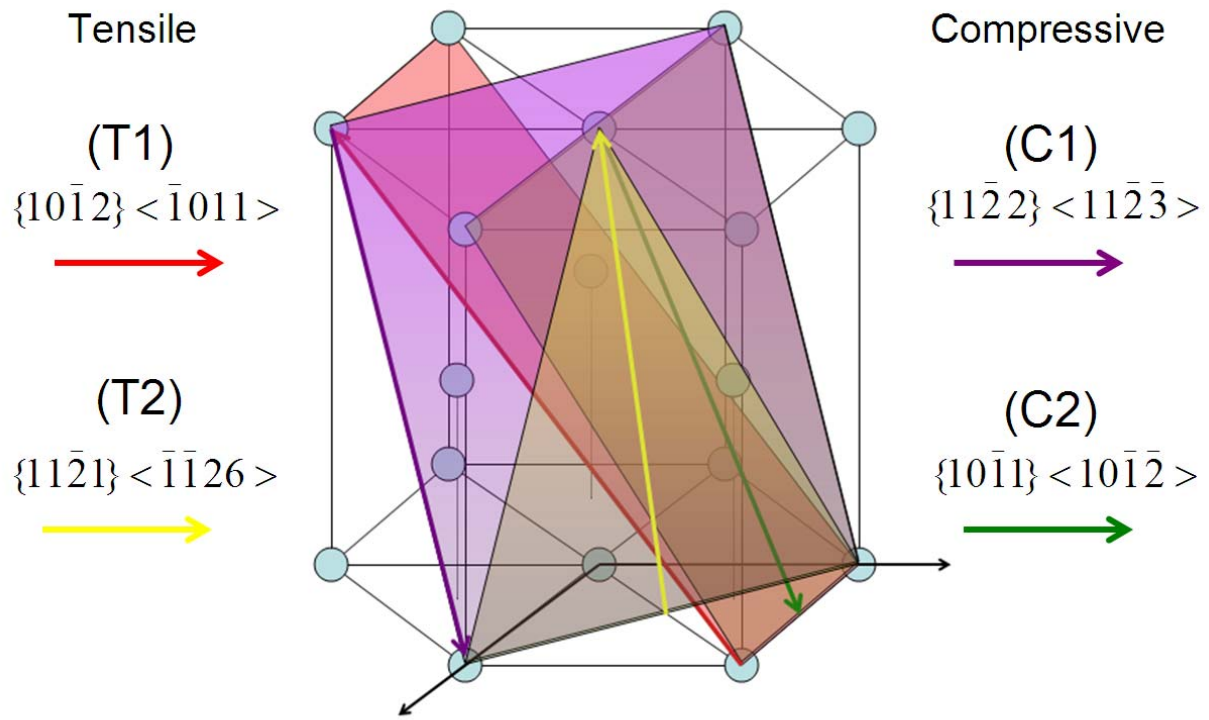
Figure 2.12 Twinning plane and twinning direction of the four twinning modes in Ti.
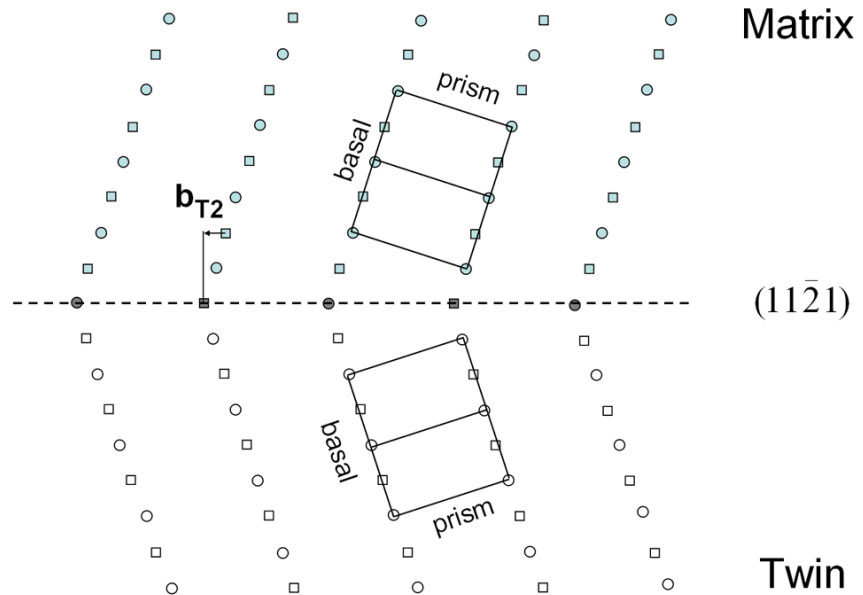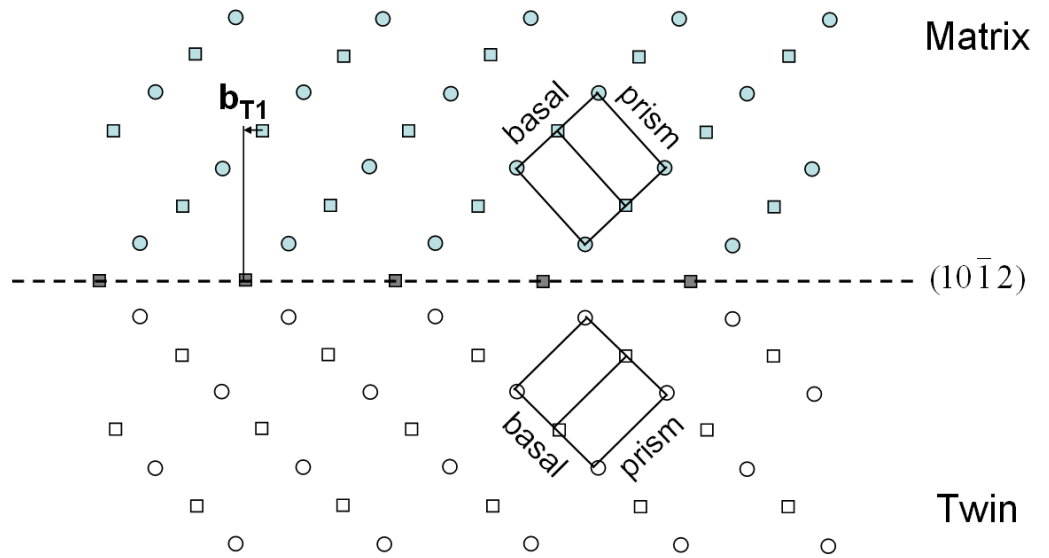
Figure 2.13 The atomic projections show T1 and T2 twinning for hexagonal Ti .

2.4 The Role of Twinning in Crystal Plasticity

Plastic anisotropy of polycrystals arises from two causes: anisotropy of the single crystal properties (e.g. discrete slip/twinning systems) and crystallographic texture. The constitutive equations that describe the deformation of real polycrystals, often being referred to as crystal plasticity, are much more complex than those for isotropic materials.

The two simplest polycrystalline deformation models are the Taylor and Sachs models. The Taylor model assumes a uniform strain rate in the entire polycrystal [Taylor (1934)]. This assumption ensures inter-grain compatibility and provides an upper bound to the stress. The Sachs model, on the other hand, assumes a uniform stress state in the entire polycrystal and allows each grain to deform independently from its neighbors, to provide a lower bound to the stress [Sachs (1928)]. The Taylor model has been used more often. Kalidindi et al. (1992) implemented a Taylor-type model with a set of constitutive equations that employ a power-law visco-plastic flow rule from Asaro and Needleman (1985) as well as a phenomenological slip system hardening scheme. This model is very successful for predicting macroscopic stress-strain relationship and texture evolution for cubic materials like Cu [Bronkhorst et al. (1992)] and Al [Kalidindi et al. (2004)]. To ensure compatibility everywhere, the Taylor model requires at least five operative slip systems in each grain. This requirement is not difficult to meet for cubic materials with high symmetry. For hexagonal materials, however, the lack of deformation modes with low activation stress makes the Taylor model less suitable because deformation of a cluster of grains shows that some strain much more than others. Even so, some still use Taylor-type models to simulate hexagonal materials [Salem et al. (2005), Wu et al. (2007)].

Two, more rigorous, approaches are the self-consistent method and the finite element method. The self-consistent method treats grains as inclusions embedded in a Homogeneous Effective Medium (HEM). Each grain is assumed to be representative of all the grains with the same orientation, and the HEM represents the average of the entire grain aggregate. The method is called "self-consistent" because the assumed HEM is adjusted so that its overall response to external loading conditions is the same as the aggregate of all individual grains. The grain interaction that occurs in a real polycrystal is simplified in the model as the interaction between each grain as an Eshelby inclusion and the HEM [Lebensohn et al. (1993), Kocks et al. (1998)]. With its statistical nature, the self-consistent method is able to calculate the stress-strain response and texture evolution from a large volume (thousands of grains). A disadvantage of this method is that it neglects local effects between particular neighboring grains. Whether or not this omission will significantly affect the computational results remains unclear and need to be analyzed case by case.

The Crystal plasticity finite element method (CPFEM), on the other hand, is very suitable for describing local effects between grains. It uses the real grain aggregate (often characterized by EBSD) to generate a finite element mesh. Each grain is then divided into many small elements. By applying local compatibility and stress equilibrium conditions for each node (connecting points between neighboring elements) and using an iterative approach, the step-wise deformation history in each element can be calculated. The distribution and evolution of stress, strain, crystal orientation and individual slip system activities can be easily displayed for the simulated grain aggregate and compared with surface characterization results [Becker et al. (1995), Delaire et al. (2000), Raabe et al. (2001, 2004), Kalidindi (2004), Musienko et al. (2007), Bieler et al. (2009),

Roters et al. (2010), Yang et al. (2011)]. The disadvantage of CPFEM is the high computing

cost. As the result, most CPFEM studies simulate grain aggregates with only several tens of

grains.

Operation of deformation systems at the grain level is the key idea for any crystal plasticity

model, regardless of the method used (Taylor, self-consistent, or CPFEM). The visco-plastic

flow rule used in many models is essentially based on the Schmid law: when the resolved shear

stress on a slip system exceeds the CRSS, that slip system is activated and starts to contribute to

the total shear. This scheme has been used in many works to also describe twin nucleation and

subsequent propagation by assigning a CRSS for each twinning mode [Meyers et al. (2001),

Tome et al. (2001), Salem et al. (2005), Kaschner et al. (2006), Wu et al. (2007), Bieler et al.

(2009), Yang et al. (2011)]. However, it has been known that twin nucleation, especially in

hexagonal metals, is highly sensitive to the local microstructure, and the very existence of a

uniform CRSS for twinning is doubtful [Christian et al. (1995)]. Recent statistical studies of T1

twinning in Zr [Capolungo et al. (2009b)] and Mg [Beyerlein et al. (2010b)] show that the

distribution of twinning Schmid factors of the observed twins is quite broad and the activated

twin variant, in many cases, is not the one with the highest Schmid factor. Because deformation

twinning is as important as dislocation slip for hexagonal metals, a more physics-based twin

nucleation model is needed to replace the conventional CRSS-based model for better predicting

the constitutive response and microstructrual evolution of hexagonal metals.

For the most frequently observed T1 twinning mode in hexagonal metals, various atomic-level

mechanisms have been proposed by topographical analysis or atomistic simulation since the

1950s [Thompson et al. (1952), Serra et al. (1996, 1999), Li et al. (2009), Wang J et al. (2009a, 2009b)]. Most of these mechanisms still need experimental validation and they do not take the grain boundary into account. In reality, most twins nucleate at grain boundaries [Capolungo et al. (2009b), Beyerlein et al. (2010b)], probably because grain boundaries can provide the source for multiple twinning dislocations that are necessary for a stable twin nucleus [Christian et al. (1995), Wang J et al. (2009a, 2009b)]. A recent atomistic simulation work studied the role of a grain boundary in twin nucleation [Wang J et al. (2010)]. It suggests the following twin nucleation scheme: interaction of a dislocation pile-up with an array of pre-existing grain boundary defects (GBDs) causes dissociation of GBDs into twinning partials, which coalesce to form a twin nucleus with zonal dislocations (coordinated clusters of partial dislocations). This scheme is shown in Figure 2.14.

Although this grain boundary nucleation scheme has not yet been validated by experiment (probably by high resolution TEM), Beyerlein et al. (2010a) turned this scheme into a probabilistic twin nucleation theory and implemented it into a multi-scale self-consistent constitutive model. In this model, twin nucleation is treated as a random event that follows a Poisson distribution. The rate of twin nucleation increases with the surface area of a grain (proportional to square of the grain size) and local stress. For Zr, this new model gives a more precise stress-strain predication than the former model using a CRSS-based treatment of twin nucleation, especially at low temperature, where twin activity is more pronounced (Figure 2.15). This model also agrees with EBSD characterization results by successfully predicting the increase of twin fraction with strain and the distribution of twinning Schmid factors of all observed twins. Despite making many simplifications, this pioneering work shows that a crystal

plasticity model using a more physics-based twin nucleation model would outperform a crystal plasticity model that simply treats twin nucleation in a CRSS-based law. This underscores the importance and urgency of identifying physics-based twin nucleation mechanisms in hexagonal polycrystals.
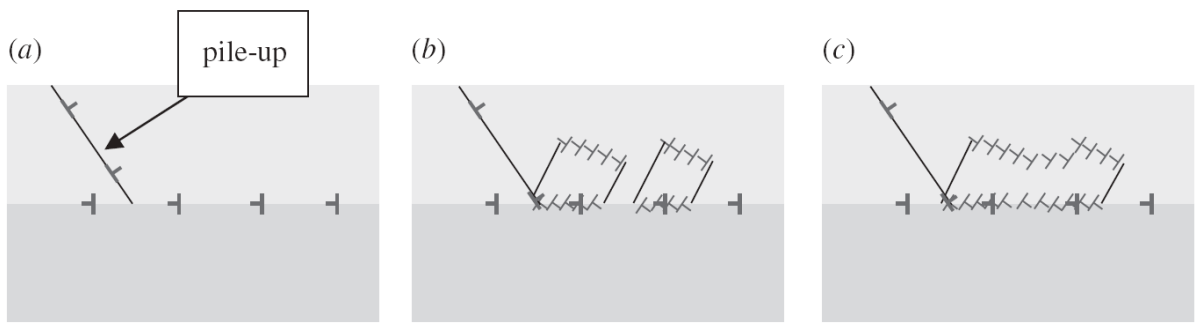
Figure 2.14 Schematic process of twin nucleation from a grain boundary: (a) interaction of a dislocation pile-up with an array of grain boundary defects (GBDs). (b) Dissociation of GBDs into twinning partials. (c) Multiple twinning partials combine into a stable twin nucleus [Beyerlein et al. (2010a)].
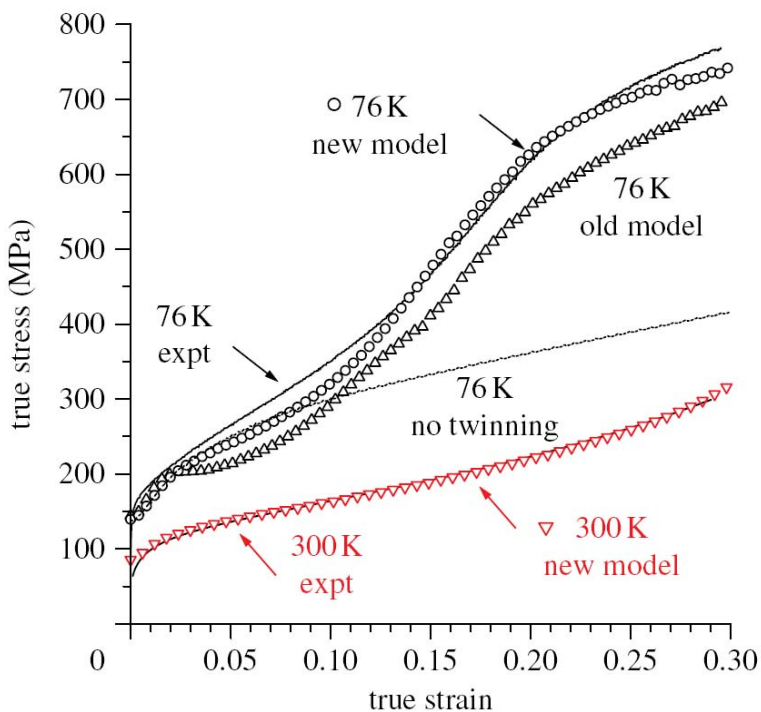
Figure 2.15 Comparison of the predicted and measured stress–strain response of Zr at 76K (black) and room temperature (red). At 76K, the new model using probabilistic twin nucleation theory performs better than the old model using CRSS-based twin nucleation theory [Beyerlein et al. (2010a)].

2.5 Literature Review Summary

Plastic deformation of metals at the microscopic scale is mediated by dislocation slip and twinning. EBSD and DAXM provide opportunities to study dislocations and twins in bulk materials. For example, from surface observations of slip bands/twins in a given grain, an EBSD scan allows quick identification of the likely slip/twinning systems. EBSD is also convenient to characterize in-grain orientation gradients. Reconstructed Laue patterns measured with DAXM can be used to analyze subsurface dislocation content if the diffraction peaks are streaked, though the reliability of this method is still being evaluated.

Hexagonal materials have slip and twinning modes that are more complex than cubic materials. In Ti, there are four common slip modes, with the prismatic slip being the one with the lowest CRSS. In addition, there are four twinning modes. Understanding of twinning in hexagonal metals is limited, even for T1 twinning, the most frequently observed mode. As a general rule, twins are more likely to form in those grains with a high twinning Schmid factor. However, not all grains with a high twinning Schmid factor actually nucleate twins. Recent investigations, by both statistical observations and atomistic simulation, suggest that the grain boundary structure plays an important role in twin nucleation. However, it is still unclear what type of grain boundaries is favorable for twin nucleation. Compared to T1 twins, knowledge of other twinning modes are even less well understood. For example, though T2 twins have been observed in different hexagonal metals, their nucleation, propagation, and interaction with matrix dislocations have hardly been studied.

In order to find out what type of grain boundaries are favorable for T1 twin nucleation, a statistically significant number of observations are needed, which can be achieved with EBSD. Though much less common than T1 twins, T2 twins are also important to investigate because the large twin shear they carry could lead to dramatic strain incompatibility at grain boundaries, which may alter the activated deformation systems in the region. Because T2 twins are usually thin, high resolution electron imaging and fine step EBSD are needed to uncover their mechanistic details and related deformation accommodation processes around them. Multiple instances of T2 twins need to be analyzed in order to determine if there are conditions that consistently favor their formation. In addition to SEM and EBSD, DAXM can also be employed to characterize the subsurface structure of twins. Peak streak analysis will allow the dislocations near the twin boundaries to be analyzed, which will provide understanding of how the matrix accommodates twinning.

Most current CPFE models still use CRSS-based laws to describe twinning, and the interaction between dislocations and twins is treated in a simple hardening law. Once the picture of twin nucleation, and the way twins are accommodated in the matrix, are more clearly understood, CPFE models can be significantly improved.

This dissertation will examine the origins of twin nucleation and the accommodation processes around them. After the details of EBSD and DAXM experiments are given in Chapter 3, Chapter 4 and Chapter 5 examine two types of grain boundaries that are favorable for T1 twin nucleation. Unlike other works that focus more on the character of the grain boundary (i.e. grain boundary misorientation, etc.), this work focuses on the crystallographic relationships of slip and

twinning systems between grains on either side of the grain boundary. In particular, the role of slip transfer on twin nucleation will be assessed. In Chapter 6, DAXM and the associated peak streak analysis is applied to two examples to characterize dislocations near grain boundaries. Chapter 7 focuses on T2 twinning in Ti. Fine characterization of T2 twins using high resolution EBSD and DAXM reveals unusual surface topology, orientation gradients, and residual dislocations around T2 twins that have not been noted before. The difference between T2 and T1 twins in their nucleation, growth and morphology will be interpreted. Chapter 8 will discuss the impact of this work to the field and some related research opportunities. Chapter 9 summarizes the thesis as well as some future works.

Chapter 3

Experiment and Analytical Methods

3.1 Samples and EBSD Experiments

Commercial purity grade 1 Ti (softest, unalloyed) samples with dimensions of

$25mm \times 3mm \times 2.5mm$ (W $\times$ H $\times$ D) were cut from a 12 mm thick plate using Electrical

Discharge Machining (EDM), and used for all works in this thesis. In order to obtain a smooth

surface for SEM imaging and EBSD analysis, samples were mechanically polished, ending with

a colloidal silica suspension. Most of the SEM imaging and EBSD analysis was performed in a

Camscan 44FE scanning electron microscope equipped with an orientation imaging microscopy

(OIM) system (EDAX/TSL, Draper, UT). Some high quality images and EBSD scans were

obtained using a JEOL 6500 SEM at Max-Planck-Institut für Eisenforschung in Düsseldorf,

Germany.

All samples were deformed by four-point bending with the polished surface facing upward.

Most investigations were focused on the surface center, where the stress was shown to be

uniform tension in a continuum elastic-plastic finite element analysis [Wagenknecht et al.

(2008)]. The tensile strain is estimated using the surface curvature of the bent sample. The

microstructure after deformation was often characterized by SEM imaging and EBSD analysis

with the sample remaining in the bending stage. Two imaging modes, backscattered electron

(BSE) mode and secondary electron (SE) mode, were used. For the EBSD scans, the sample was

tilted 70° from the incident electron beam. The scan step size was chosen based on the

resolution needed, mostly between 0.5μm to 2μm. OIM software (OIM 5.31) is used for both data acquisition and data analysis.

With an orientation map, the active slip and twinning systems that correspond to the observed slip bands and twins in individual grains can be determined. If grain orientation is known, then the orientation of any slip or twinning planes in that grain can be calculated using Eq. 2.5. For a grain that displays slip bands, the active slip system must have its slip plane's surface trace parallel to the slip bands. If multiple slip systems satisfy this trace analysis, then their Schmid factors and relative CRSS values need to be compared with each other in order to identify the most likely active slip system. For deformation twins, the operating twinning system must also have its twinning plane's surface trace nearly parallel to the twin boundary. However, the situation was sometimes complicated by the curvature of the twin boundaries. To confirm the operating twinning system, the crystallographic character of the twins were checked by comparing their orientations with that of the parent grains: the twin orientation is uniquely related to the parent grain by a 180° rotation around the parent grain twinning plane (K1) normal or twinning shear direction (η1) [Christian et al. (1995)].

3.2 DAXM Experiment and Laue Pattern Indexing

The synchrotron X-ray source and the DAXM device used in this work are on beamline 34-ID-E at the Advanced Photon Source (APS) at Argonne National Laboratory. A pair of Kirkpatrick-Baez (KB) mirrors was used to generate a polychromatic X-ray microbeam that is about 0.5 μm × 0.5 μm. This microbeam penetrated the sample surface from a 45° inclination angle and

generated Laue patterns from regions up to several hundred microns beneath surface along the

beam path. The Laue patterns were collected by an X-ray CCD camera located at 90° to the

incident beam.   The geometry of the beam, the sample, and the CCD camera were shown in

Figure 2.8. Using the differential aperture (Pt wire) and processing the differentiated images by

computer, Laue patterns from individual volume elements (voxels) along the beam path are

reconstructed.

Figure 3.1 shows a Laue pattern from a voxel ~10μm beneath the surface in a Ti sample. All

reflections in this pattern were identified and indexed by the computer. Different crystal planes

have different interplanar spacing and their corresponding reflections are generated by different

beam wavelength (energy) mixed in the polychromatic microbeam. Crystal planes for hexagonal

metals are commonly written in 4-digit indices, but the software at APS gives a 3-digit index for

each peak that does not consider crystalline symmetry. As a result, the $(34\bar{1})$ peak in the lower

part of the pattern can actually represent any one of the following twelve symmetrical planes in

Ti: $(43\bar{7}1)$, $(4\bar{7}31)$, $(3\bar{7}41)$, $(34\bar{7}1)$, $(\bar{7}341)$, $(\bar{7}431)$, $(\bar{4}3\bar{7}\bar{1})$, $(\bar{4}7\bar{3}\bar{1})$, $(\bar{3}7\bar{4}\bar{1})$, $(\bar{3}47\bar{1})$,

$(7\bar{3}\bar{4}\bar{1})$, $(7\bar{4}3\bar{1})$. These 12 symmetrical crystal planes correspond to the 12 choices of

equivalent Euler angles in hexagonal crystals that were discussed in section 2.1. The Laue

pattern in Figure 3.1 came from a surface grain whose orientation was measured by EBSD to be

$(\varphi_1, \Phi, \varphi_2)$ = (35°, 88°, 147°). Assuming this orientation and using Equations (2.4) and (2.5), it

was found that the direction of pole $(3\bar{7}41)$ matches the actual position of the $(34\bar{1})$ reflection

in the pattern. Therefore, peak indices can be converted from 3-digit to 4-digt as: $(34\bar{1})$ →

$(3\bar{7}41)$, $(421) \rightarrow (4\bar{6}2\bar{1})$ and so forth. In fact, the whole Laue pattern can be calculated by projecting different plane poles onto the CCD screen. Figure 3.2(a) shows the 4-digit indices for some reflections in the pattern in Figure 3.1. Figure 3.2(b) shows a calculated Laue pattern based on $(\varphi_1, \Phi, \varphi_2) = (35°, 88°, 147°)$. The calculated pattern matches the experimental pattern very well, which in turn, validates the above index conversion practice.
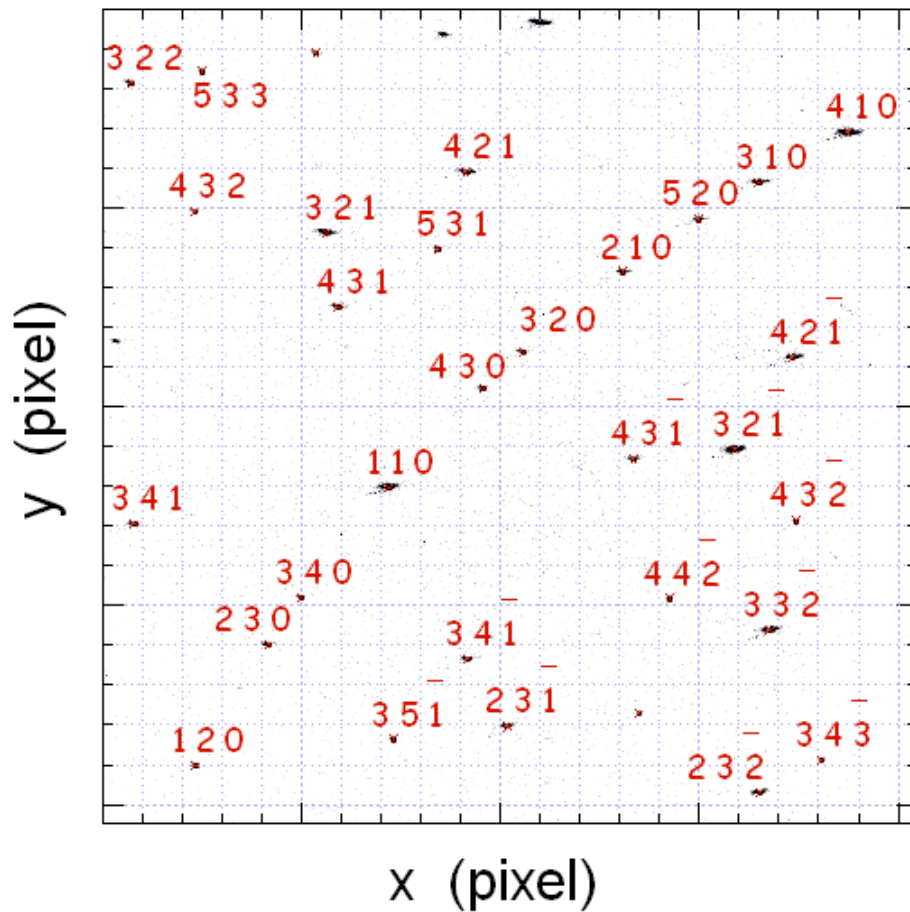
Figure 3.1 Automatic indexing results of the Laue pattern from a voxel ~10μm beneath the surface of a Ti sample.
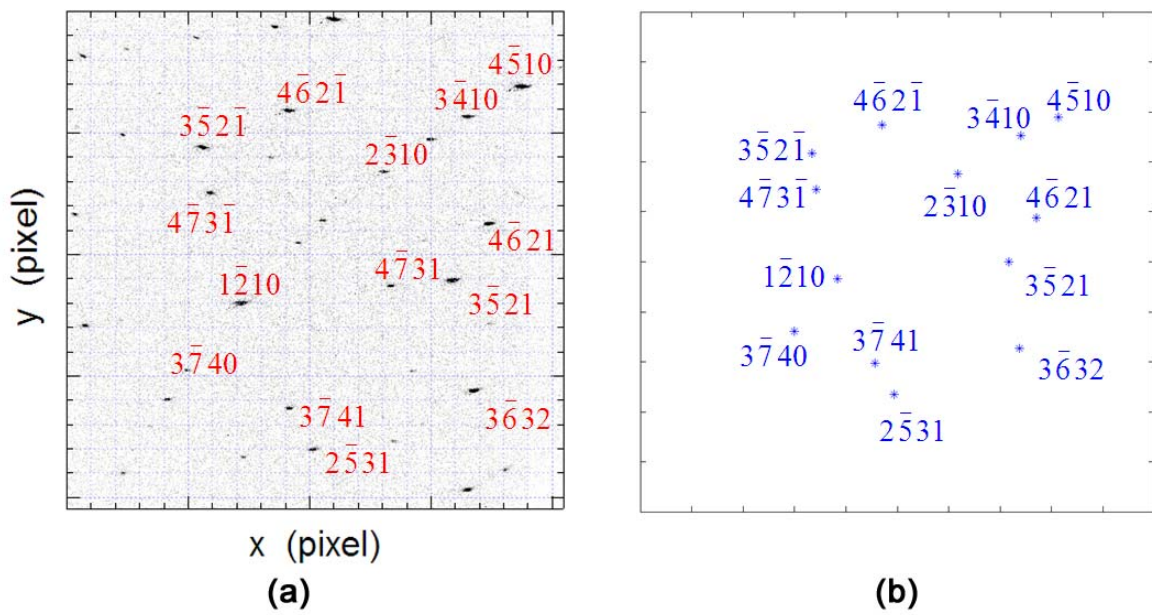
Figure 3.2 (a) Peak indexed in 4-digit for the pattern shown in Figure 3.1. (b) Calculated Laue

pattern based on the crystal orientation of the voxel.

3.3 Analyzing Dislocation Content from Streaked Peaks

A dislocation free sample generates diffraction peaks as sharp points. As most atoms occupy their ideal positions in the lattice, diffraction occurs only when the scattering vector $\mathbf{s}$ is equal or very close to a reciprocal lattice vector $\mathbf{g_{hkl}}$. After deformation, atoms are displaced from their ideal positions so that diffraction can occur even if $\mathbf{s}$ deviates from $\mathbf{g_{hkl}}$. As a result, diffraction peaks from a deformed sample are usually broadened (symmetrically or asymmetrically), also known as diffuse scattering. The intensity distribution in a broadened diffraction peak is strongly affected by the arrangement of local lattice defects such as dislocations.

If the deformation is not too large, scattering vectors $\mathbf{s}$ close to a reciprocal lattice vector $\mathbf{g_{hkl}}$ will follow the structure factor f to generate coherent radiation with intensity I, which can be written as [Krivoglaz (1996)]

$$
\begin{aligned}
I(\mathbf{s}) &= \left| \sum_{j=1}^{N} f \exp(2\pi i \mathbf{s} \cdot \mathbf{r_j}) \right|^2 = \left| \sum_{j=1}^{N} f \exp(2\pi i \mathbf{s} \cdot (\mathbf{R_j} + \mathbf{u_j})) \right|^2 \\
&= \sum_{j,j'=1}^{N} f^2 \exp(2\pi i \mathbf{s} \cdot (\mathbf{R_j} - \mathbf{R_{j'}})) \exp(2\pi i \mathbf{s} \cdot (\mathbf{u_j} - \mathbf{u_{j'}}))
\end{aligned}
\tag{3.1}
$$

Here $\mathbf{R_j}$ (and $\mathbf{R_{j'}}$) and $\mathbf{r_j}$ (and $\mathbf{r_{j'}}$) are the radius vector of the j-th (and j'-th) unit cell before and after deformation, $\mathbf{u_j}$ (and $\mathbf{u_{j'}}$) is the vector of the displacements of the first atom in the j-th (and j'-th) unit cell, and N is the total number of unit cells. The most important parameter in equation (3.1) is $\mathbf{u_j}$, which can be viewed as the sum of the displacement fields from nearby dislocations upon the j-th unit cell. Direct utilization of Equation (3.1), however, can be very complicated, which requires many numerical approximations [Krivoglaz (1996), Kaganer et al. (1997)].

Geometrically necessary dislocations (GNDs) have a much more pronounced influence on scattering than statistically stored dislocations (SSDs) [Ice et al. (2007)]. GNDs are associated with a strain gradient and lattice rotations in the material. When the plane normal of the crystal plane (*hkl*) rotates in 3D space, its Laue peak will appear as a streak that can be understood as the intersection of the rotating trace of $\mathbf{g_{hkl}}$ with the Ewald sphere. For a lattice rotation that is not too large, the shape of a diffraction peak often appears as a straight streak. The direction of streaked peaks depends on the lattice rotation direction, which is related to the nature of local GNDs. Based on these assumptions, a simplified method to estimate Laue streaked peaks direction in a rotated lattice due to a set of GNDs is proposed.

The most effective way to describe GNDs is using Nye's tensor [Nye (1953), Arsenlis et al. (1999)]. Generally, if n types of GNDs exist in a given volume, then Nye's tensor can be written as

$$\widetilde{\boldsymbol{\alpha}} \equiv \sum_{k=1}^{n} \rho_k \mathbf{b^k} \otimes \boldsymbol{\tau^k} \tag{3.2}$$

$\mathbf{b^k}$ and $\boldsymbol{\tau^k}$ are Burgers vector and line vector of the kth set of GNDs with density ρ_k. In Cartesian coordinates, assuming there is only one set of GNDs (Burgers vector $\mathbf{b}$, line vector $\boldsymbol{\tau}$, dislocation density ρ), Nye's tensor simplifies as

$$\alpha_{ij} = \rho b_i \tau_j \tag{3.3}$$

Nye's tensor can be related to the lattice curvature by the following equation [Nye (1953)]:

$$\kappa_{ij} = \alpha_{ji} - \frac{1}{2}\delta_{ij}\alpha_{kk} \tag{3.4}$$

where κ_{ij} is the curvature tensor describing the magnitude of the rotation around the i-axis for a small position change in the j-direction ($\kappa_{ij} = \dfrac{d\theta_i}{dx_j}$). For convenience, a "dislocation coordinate system" is defined where the three orthogonal axes x_1, x_2, and x_3 are along the Burgers vector **b**, slip plane normal **n**, and the tangent direction **t**=**b**×**n**, respectively. In this "dislocation coordinate system", the only non-zero term in the Nye's tensor for a set of edge GNDs is α_{13}=ρ, so the only non-zero term in the curvature tensor is κ_{31} =ρ according to Eq. (3.4). Similarly, the only non-zero term in the curvature tensor for a set of screw dislocations is κ_{11}=α_{11}=ρ. The curvature tensor κ_{ij} is related to the lattice rotation tensor ω_{ij} as [Arsenlis et al. (1999), Pantleon (2008)]:

$$\omega_{ij} = -\varepsilon_{ijk}\theta_k = -\varepsilon_{ijk}\kappa_{kl}x_l \qquad (3.5)$$

In the above defined "dislocation coordinate system", for a set of edge GNDs, ω_{12}= $-\omega_{21}$= ρx_1, ω_{13}= ω_{31}=ω_{23}= ω_{32}=0. For a set of screw GNDs, ω_{12}= $-\omega_{21}$= $\rho x_3/2$, ω_{23}= $-\omega_{32}$= $-\rho x_1/2$, ω_{31}= $-\omega_{13}$= $\rho x_2/2$. Before the lattice rotation tensor **ω** can be used, it must be transformed into a tensor **Ω** in the sample coordinate system using the rotation matrix

$$\mathbf{A} = \begin{bmatrix} b_X & b_Y & b_Z \\ n_X & n_Y & n_Z \\ t_X & t_Y & t_Z \end{bmatrix} \qquad (3.6)$$

Here, b_X, b_Y, and b_Z are the three components of **b** along the X, Y, and Z directions in the sample coordinate system. Similar definitions apply for **n** and **t**. Finally, the rotation trace of **g**_{hkl} is given by:

$$\xi = \Omega \cdot \mathbf{g_{hkl}} = \mathbf{A}^T \omega \mathbf{A} \cdot \mathbf{g_{hkl}} \tag{3.7}$$

The actual streaked peaks direction is the projection of ξ on the detector screen. For edge GNDs,

ξ calculated using (3.7) is equivalent to the previously proposed equation $\xi = \dfrac{\tau \times \mathbf{g}_{hkl}}{|\tau \times \mathbf{g}_{hkl}|}$

[Barabash et al. (2001, 2003)].

Eq. (3.7) can be used to predict the theoretical streak direction at any reflection (*hkl*) for any

dislocation content, which in turn, can help us analyze local active slip system. For each of the

24 regular slip systems in Ti (Figure 2.10), theoretical peak streak direction can be calculated

based on edge or screw dislocations on that slip system. Out of the 48 possibilities, the one that

gives correct streak direction for *all* diffraction peaks should account for the actual dislocation

content. Sometimes slip systems beyond those defined in Figure 2.10 must also be considered;

especially when none of the 24 regular slip systems gives a perfect fit (examples will be seen in

Chapter 7).

Chapter 4

Twin Nucleation by Slip Transfer at Grain Boundaries

Slip bands and deformation twins were observed in Ti samples deformed by 4 point bending in SEM. Active slip and twinning systems were identified using EBSD. The role of strain transfer in the activation of deformation twinning at grain boundaries was characterized from particular observations to a general twin nucleation mechanism. It is found that for soft/hard grain pairs, prismatic <a> dislocations, which is easily activated in the soft grain, can stimulate nucleation of T1 twins in the neighboring hard grain when the slip system has a good geometric alignment with the twinning system. This alignment was described by a slip transfer parameter, *m'* [Luster et al. (1995)]. For this slip-stimulated twin nucleation mechanism, the magnitude of *m'*, rather than twinning Schmid factor, dictates twin nucleation in the hard grain. The results in this chapter indicates that twin nucleation in polycrystals depends not only on the orientation of the parent grain, but also on the deformation history of neighboring grains. The content in this chapter was published in a journal paper [Wang L., Yang Y., Eisenlohr P., Bieler T.R., Crimp M.A., Mason D.E., 2010. Twin Nucleation by Slip Transfer across Grain Boundaries in Commercial Purity Titanium. Metall. Mater. Trans. A, 41, 421-430.] A reprint permit has been obtained from the journal.

4.1 Samples

This work used two samples, B-0 and B-45, cut from a commercial purity Ti plate.   Figure 4.1

shows the {0001} and {10$\bar{1}$0} pole figures of these two samples, as measured by EBSD. In both

samples, the texture measurements came from a 2.5mm × 2.5mm area at the surface center. The

maximum texture strength was about 8 times random intensity in both samples. (The value is

estimated from the intensity peak value in the {0001} pole figures, which has some variation

from region to region). In the B-0 sample, the density of {0001} poles was high in a 30° cone

centered along the tensile axis, which means B-0 had a large fraction of "hard grains". The B-45

sample was cut so that the cone axis of {0001} poles were oriented ~ 45° from the tensile axis,

resulting in more "soft grains" than in B-0. The {10$\bar{1}$0} pole figures show a fiber texture with

the fiber axis along the tensile axis for B-0, such that there is a lack of prismatic plane normals

along the tensile axis. It is evident that there are very few grains with c-axes within 45° of the

specimen normal direction. The two samples were deformed by four-point bending along their

longitudinal direction to achieve a surface tensile strain of ~ 2% for B-45, and ~ 8% for B-0.
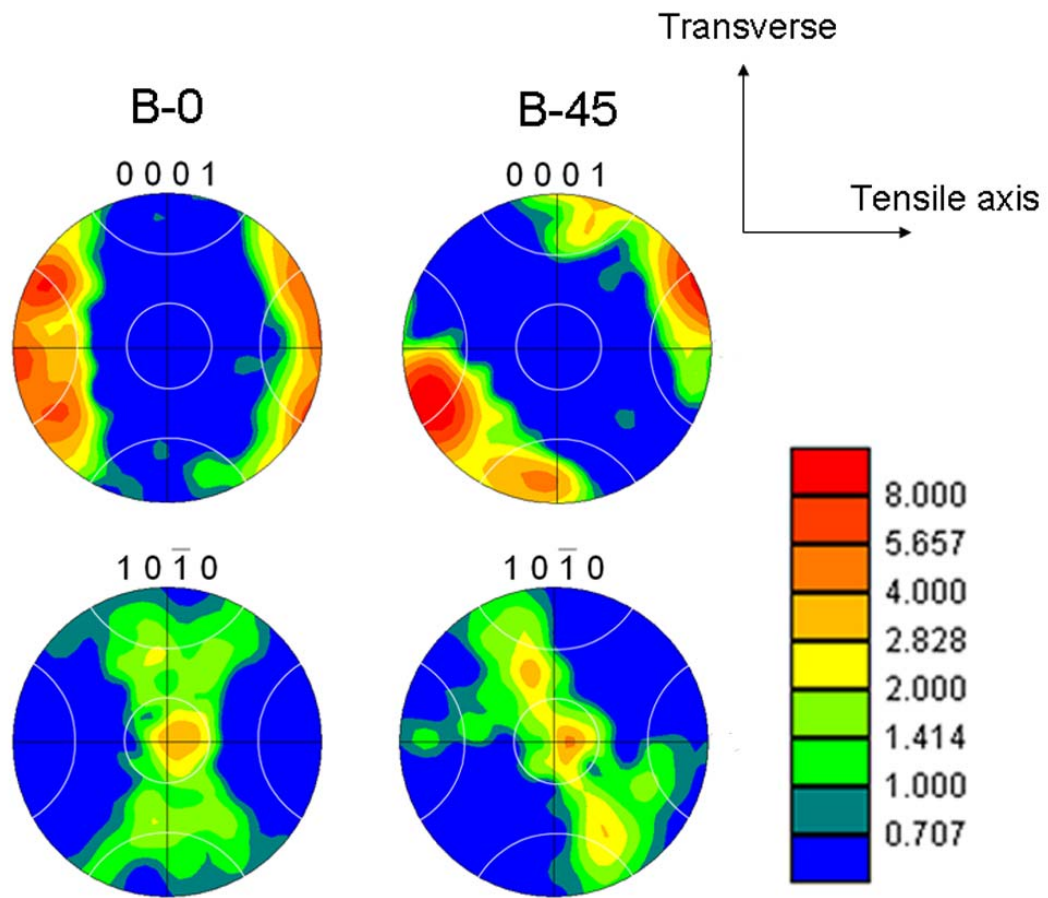
Figure 4.1 {0001} and {10$\bar{1}$0} pole figures from samples B-0 and B-45. B-45 is a "softer" orientation sample than B-0. 30° cones are superimposed on these stereographic projections along the major axes.

4.2 Identification of Active Deformation Systems

Figure 4.2(a) shows an image of the microstructure of sample B-45, where slip-stimulated twin nucleation was first noticed. The corresponding orientation map (Figure 4.2(b)) shows soft grains with colors towards blue and green and hard grains towards red. In most of the soft grains, such as grains 1, 3, 4, 6, and 16, distinct slip bands were aligned with the plane trace of the prismatic slip system with the highest Schmid factor (with respect to the tensile axis). In a few grains displaying multiple slip bands, two prismatic slip systems with similarly high Schmid factors were observed (e.g. grains 5 and 10). In some soft grains, such as grains 7, 11, and 13, the prismatic slip lines were less distinct. In grain 17, three distinct slip traces were observed: two prismatic (with relatively low Schmid factors of 0.21 and 0.17) and one basal slip (Schmid factor of 0.45). Although absent in this microstructure, pyramidal slip was also observed occasionally; these slip lines are generally not as distinct as prismatic slip lines. In some grains, no slip lines were visible, suggesting these particular grains did not carry much plastic deformation or that deformation was less concentrated in slip bands (for example grains 8, 12 and 18).

Besides slip bands, lenticular deformation twins were also observed in a number of grains, including 2, 7, 14, and 15. These were evident in both the SEM image and the orientation map. (The deformation twin in grain 7 was too thin to be detected in this orientation map, but it was later confirmed in an orientation map with a smaller step size) Grains 2, 14, and 15 were hard grains, with their c-axes nearly parallel to the tensile axis. Trace and crystallographic analysis revealed that *all* of the characterized deformation twins in samples B-45 and B-0 were T1 twins

($\{10\bar{1}2\} < \bar{1}011 >$). This result is not surprising, given the global tensile stress on the two samples.

Figure 4.2(c) shows the {0001} (c-axis) discrete pole figures extracted from the rectangular area outlined in the orientation map in Figure 4.2(b) before and after deformation. Before deformation, the c-axis pole of each grain is a small spot in the pole figure. Following deformation, the orientations of most grains did not change significantly, but the spots for c-axis poles broadened by varying amounts, suggesting that orientation gradients developed in the grains. For example, the spot of grain 2 became very large after deformation, so one would expect a significant spread of orientation within grain 2, which is directly observed from the channeling contrast variation in the SEM image (Figure 4.2(a)). The c-axis poles of grains 1, 2, 3, 14, and 15 are marked in both pole figures. The c-axes of grains 1 and 3 were close to the sample transverse direction and almost normal to the tensile axis; consequently, these two grains were typical soft grains and trace analysis indicates they deformed by prismatic slip. The c-axes of grains 2, 14, and 15 were close to the tensile axis and were therefore hard grains. The c-axis poles of the twins formed in grains 2, 14, and 15 are marked with circles in the pole figure of the deformed state (Figure 4.2(c)). The c-axes angles of each parent/twin grain pair were 85° ($\pm1°$, the angular resolution of EBSD), consistent with the orientation relationship of T1 twinning listed in Table 2.2.
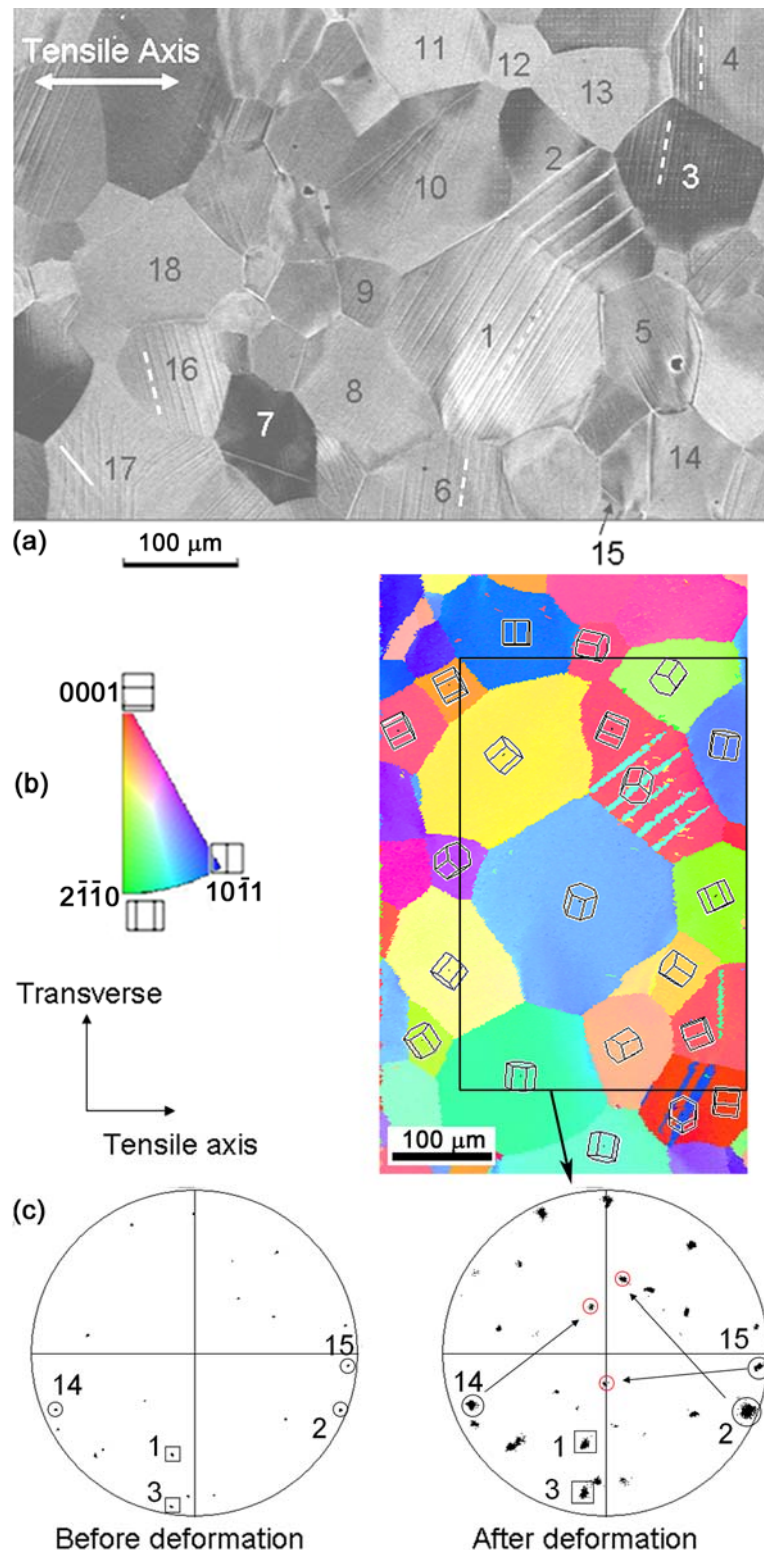
Figure 4.2 A region in B-45: (a) Prismatic slip traces and T1 deformation twins were observed

in the backscattered electron image. Distinct slip bands in most soft grains were well aligned

with the slip plane trace of the prismatic slip system with the highest Schmid factor (white dotted lines). Some non-prismatic slip modes were also identified, such as the basal slip trace in grain 17 (white solid line). (b) Lenticular T1 twins were clearly observed in the orientation map. (c) Discrete pole figures extracted from the rectangular area outlined in the orientation map before and after deformation. After deformation, orientation gradients were observed in all grains (spots of c-axis poles broadened) and additional spots resulting from twins are consistent with the known crystal rotation for T1 twins (arrows).

In sample B-0, prismatic slip was still the most evident slip mode, but because of its large fraction of hard orientations and larger imposed strain, basal and pyramidal slip traces were also observed in grains with a low Schmid factor for prismatic slip. The operation of these hard slip systems requires a higher resolved shear stress, but their operation may have precluded fracture by accommodating local strain incompatibilities. T1 twins were also occasionally observed in B-0.

4.3 Correlation Between Slip and Twins at Grain Boundaries

The deformation twins in grain 2 are thick at the boundary with grain 1, and gradually taper to a point when approaching the boundary with grain 3 (Figure 4.3), suggesting that the deformation twins were nucleated from the 1–2 grain boundary and then grew towards the 2–3 grain boundary. Intense prismatic slip in grain 1 impacts this boundary where the twins nucleated, with the prismatic slip plane traces in grain 1 being about 20° from twin plane traces in grain 2. This type of relationship between prismatic slip in soft grains and deformation twinning in hard grains has been observed in a number of cases. To assess if prismatic slip is a precursor to deformation twinning in a neighboring grain, the Luster-Morris parameter for slip transfer was evaluated [Luster et al. (1995)]:

$$m' = \cos \psi \cdot \cos \kappa \tag{4.1}$$

where ψ is the angle between the active dislocation slip plane normal ($\mathbf{n_d}$) in the soft grain (grain 1) and the operating twinning plane normal ($\mathbf{n_t}$) in the hard grain (grain 2); κ is the angle between the dislocation Burgers vector ($\mathbf{b_d}$) and the twinning Burgers vector ($\mathbf{b_t}$). Figure 4.4 illustrates this geometric relationship.

Based on the orientations of grain 1 and grain 2 (Euler angles $(\varphi_1, \Phi, \varphi_2)$= (257°, 65°, 288°) and

(339°, 87°, 196°), respectively), *m'* values between the identified prismatic slip system in grain 1

and all six T1 twinning systems in grain 2 were calculated. (The Euler angle is based on the

following coordinate system: x — transverse, y — tensile axis, z — sample normal.) Table 4.1

lists ψ, κ, and *m'*, as well as the twinning Schmid factor (m_t) for each twinning system.

Although the operating twinning system, $(10\bar{1}2)[\bar{1}011]$, had the second highest Schmid factor, it

had the highest *m'*: the plane normals ($\mathbf{n_d}$ and $\mathbf{n_t}$) were closely aligned, as were the Burgers

vectors ($\mathbf{b_d}$ and $\mathbf{b_t}$). Note that the range of *m'* (0 to 1) is twice that of the range of m_t (0 to 0.5).
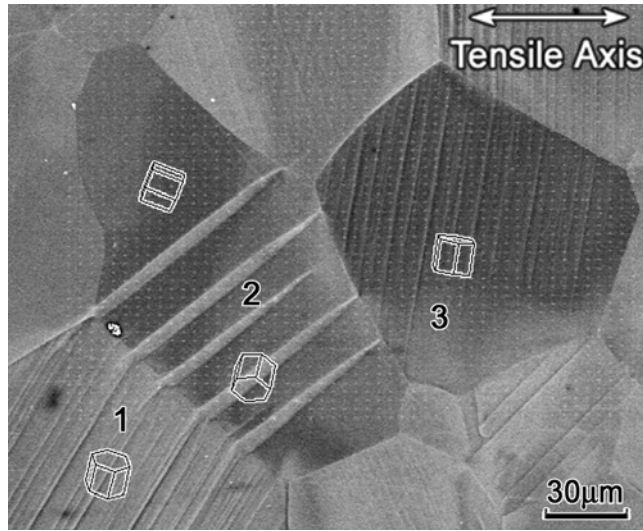
Figure 4.3 Higher resolution image from Figure 4.2 suggesting that deformation twins in grain 2
appear to have been nucleated at the grain boundary with grain 1. The prismatic slip bands in
grain 1 and the deformation twins in grain 2 are correlated.

Table 4.1 Geometric deformation system analysis for grains 1 and 2 in Figure 4.3

T1 Twinning systems	m_t	ψ	κ	m'
$(0\bar{1}12)[01\bar{1}1]$	0.440	80.4°	86.4°	0.010
$(10\bar{1}2)[\bar{1}011]*$	0.430	18.8°	8.6°	**0.936**
$(01\bar{1}2)[0\bar{1}11]$	0.407	20.5°	35.7°	0.761
$(1\bar{1}02)[\bar{1}101]$	0.403	55.9°	52.1°	0.344
$(\bar{1}012)[10\bar{1}1]$	0.389	81.0°	83.5°	0.018
$(\bar{1}102)[1\bar{1}01]$	0.333	57.2°	74.9°	0.141
* operating twinning system				
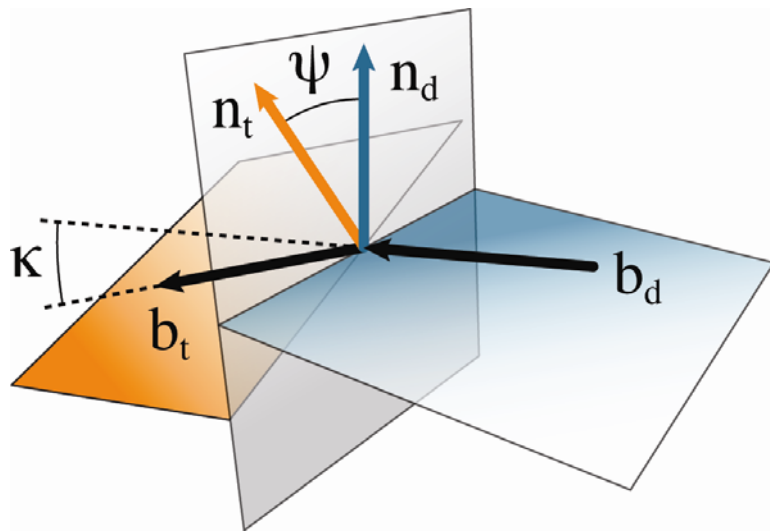
Figure 4.4 Geometric relationship between the dislocation slip system in a soft grain and the twinning system in the neighboring hard grain (d = dislocation, t = twin).

Another example of this slip–twinning correlation, found in sample B-0, is shown in Figure 4.5. The same argument as used above, i.e. the large thickness end of the twin close to the 41–42 boundary, and thickness that tapers to a point close to the opposite (upper) boundary, strongly suggests that the deformation twins in grain 42 nucleated at the grain boundary with grain 41. The prismatic slip bands in grain 41 appear to be almost parallel to the two T1 twins formed in grain 42. In this case the operating $(10\bar{1}2)[\bar{1}011]$ twinning system had the lowest twinning Schmid factor m_t (though the value is larger than 0.45) but the highest m', much higher than that of the other five T1 twinning systems (see Table 4.2).

Soft/hard grain pairs where T1 twins developed in the hard grain correlated with the prismatic slip bands in the neighboring soft grain will be referred to as S+T grain pairs (Soft+Twinning). Nine S+T pairs in sample B-45 and two in sample B-0 have been identified. In each of the 11 S+T grain pairs, the operating twinning system in the hard grain *always* had the highest m' among the six T1 twinning systems.

While a high m' indicates that two deformation systems have their plane normals and Burgers vectors close to each other, which may facilitate deformation transmission across the grain boundary [Luster et al. (1995), Davidson et al. (2007)], the cases thus far involve twinning systems with relatively high Schmid factors. It has often been assumed that deformation twins with a low Schmid factor are difficult to nucleate, especially in a small parent grain [Chun et al. (2005)]. Figure 4.6, however, indicates that nucleation of deformation twins can be triggered by neighboring localized slip activity even under less favorable conditions. In this example found in B-45, grain 52 had its c-axis oriented about 45° from the tensile axis, so all the six T1

71

twinning systems had relatively low Schmid factors (<0.25, see Table 4.3). Nevertheless, well developed deformation twins were observed in this grain, which was adjacent to a soft grain displaying distinct prismatic slip bands (grain 51). Once again, a high *m'* suggests that twin nucleation results from the local change in the stress state close to the grain boundary arising from localized prismatic slip.
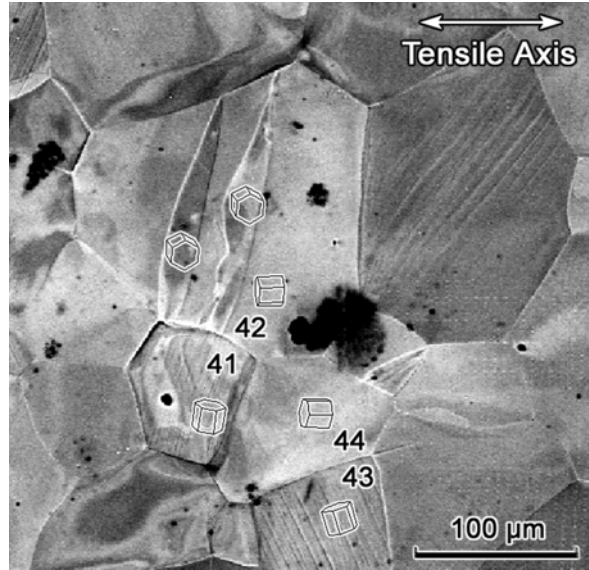
Figure 4.5 Grains 41 and 43 in sample B-0 show prismatic slip. A slip/twinning correlation example where the operating T1 twinning system in grain 42 had the lowest Schmid factor of possible twin systems but the highest *m'* (though all 6 had high Schmid factors). This pair of twins was much larger than others.

Table 4.2 Geometric deformation system analysis for grains 41 and 42 in Figure 4.5

T1 Twinning systems	m_t	ψ	κ	*m'*
$(0\bar{1}12)[01\bar{1}1]$	0.500	65.1°	82.2°	0.058
$(\bar{1}012)[10\bar{1}1]$	0.497	82.5°	82.3°	0.017
$(\bar{1}102)[1\bar{1}01]$	0.495	74.4°	80.6°	0.044
$(1\bar{1}02)[\bar{1}101]$	0.486	31.6°	45.3°	0.599
$(01\bar{1}2)[0\bar{1}11]$	0.483	45.6°	43.1°	0.510
$(10\bar{1}2)[\bar{1}011]$ *	0.475	7.8°	1.9°	**0.990**

* operating twinning system

73
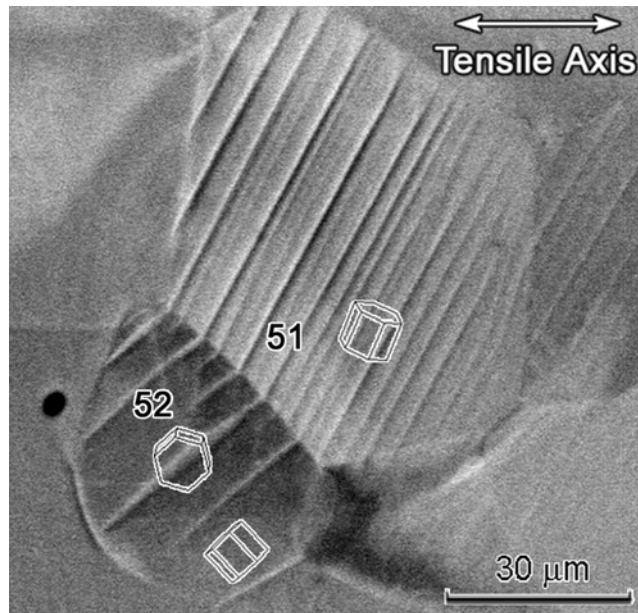
Figure 4.6 Deformation twins developed in a grain unfavorable for twinning, having its c-axis about 45° with respect to the tensile axis, resulting in a small maximum twinning Schmid factor of 0.233 (Sample B-45).

Table 4.3 Geometric deformation system analysis for grains 51 and 52 in Figure 4.6

T1 Twinning systems	m_t	ψ	κ	m'
$(1\bar{1}02)[\bar{1}101]$ *	0.233	17.7°	20.3°	**0.893**
$(\bar{1}102)[1\bar{1}01]$	0.218	81.1°	75.9°	0.038
$(01\bar{1}2)[0\bar{1}11]$	0.107	79.3°	75.3°	0.047
$(10\bar{1}2)[\bar{1}011]$	0.049	54.2°	32.4°	0.494
$(0\bar{1}12)[01\bar{1}1]$	0.025	22.9°	63.9°	0.406
$(\bar{1}012)[10\bar{1}1]$	-0.048	58.5°	81.3°	0.079

* operating twinning system

74

4.4 The Role of S+T in Total Twin Activity

Quantitative metallography reveals that slip-stimulated twins account for about a third of the total twin area in the two samples (33% in B-0 and 36% in B-45). The rest of the twins nucleated from grain boundaries, where the neighboring grain either forms another twin from the same place (T+T) or shows no obvious slip/twin activity (0+T). Examples of T+T and 0+T are shown in Figure 4.7. Table 4.4 shows the number fraction of these three categories. It is likely that part of the 0+T twins were nucleated by slip transfer from neighboring grains *beneath* the sample surface. If grains are assumed to be in a close-packed arrangement in 3-D space, then the slip-stimulated twins observed on the surface may account for about two-thirds of the total S+T events. Hence, the observed fraction of S+T events is a lower bound, and the actual fraction of slip-stimulated twins may be larger. T+T will be the focus of Chapter 5.
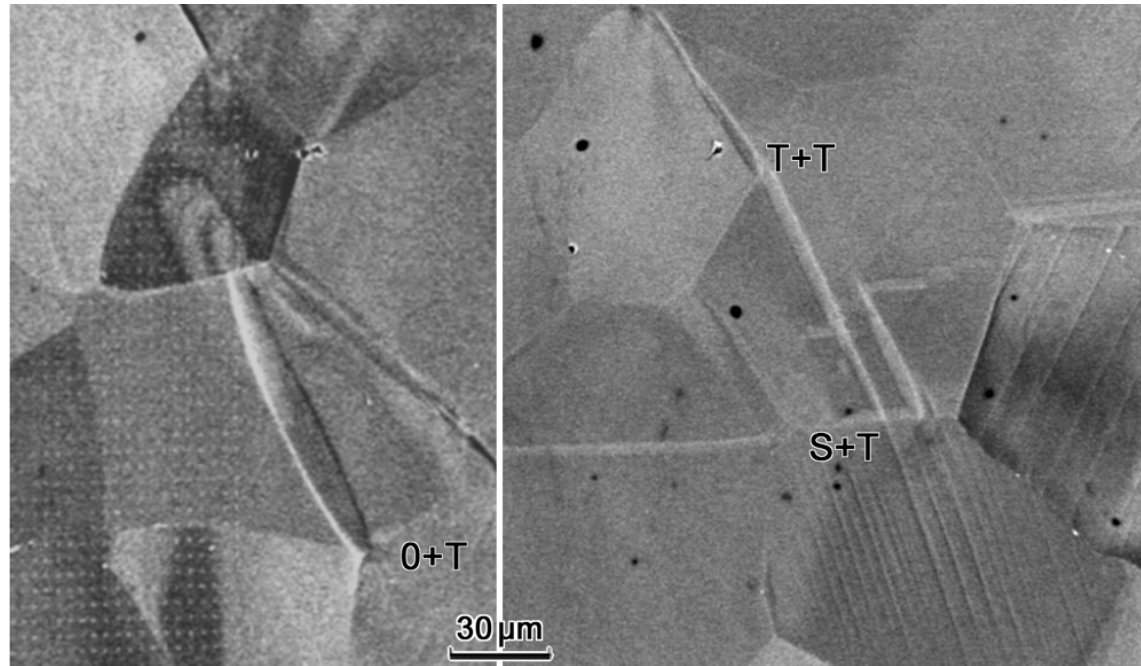
Figure 4.7 Examples of 0+T and T+T twin nucleation events

Table 4.4 Number and percentage of grain boundaries with twin interactions of different types

	S+T	0+T	T+T
B-0 ($\varepsilon \sim 8\%$)	2 (13%)	14 (87%)	0 (0%)
B-45 ($\varepsilon \sim 2\%$)	15 (29%)	25 (48%)	12 (23%)

4.5 Influence of initial texture on slip-stimulated twin nucleation

There were only two slip-stimulated twin examples (S+T pairs) observed in sample B-0, which was strained to 8%; while there were nine S+T grain pairs observed in B-45, which was strained to only 2%. The reason that the sample with lower strain exhibits many more instances of twin nucleation is the difference in their texture. S+T grain pairs are a subset of soft/hard grain pairs. Sample B-0 has many hard but few soft grains, while sample B-45 has a more balanced ratio of soft and hard grains. As a result, B-0 shows fewer slip-stimulated twins than B-45.

Examination of all 11 S+T pairs in the two samples reveals that most of the twins have their c-axes within a ~30° cone around the sample normal. Figure 4.8 shows the {0001} pole distribution of parent grains, twins, and neighboring soft grains of the 11 S+T pairs in the two samples. The c-axis poles of the parent grains are spread within ~30° of the tensile axis, indicating they are hard grains. The soft grains have their c-axes aligned within ~35° of the transverse axis. Owing to the initial texture of the two samples, all soft grains of the 11 S+T pairs have their c-axis poles close to the transverse direction, rather than the sample normal. Hence, the plane normal and Burgers vector of the active prismatic slip system in these soft grains are both roughly normal to the transverse direction (see Figure 4.9 top left). The operating twinning plane and Burgers vector in the (hard) parent grain in turn are necessarily well aligned with the active prismatic slip system in the soft grain (Figure 4.9 top right) in order to achieve a high *m'* value. Consequently, twinning causes the c-axis to be reoriented by the required 85° so that it is oriented close to the sample normal (Figure 4.9 bottom right). In other words, the existing preferred orientations of soft grains dictate the orientations of the activated twinning systems, which in turn results in a narrow distribution of the c-axis of the twins around the

77

sample normal. In summary, the initial texture and misorientation distribution determines not only the number of instances of slip-stimulated twin nucleation, but also the orientation distribution of the resulting twins.
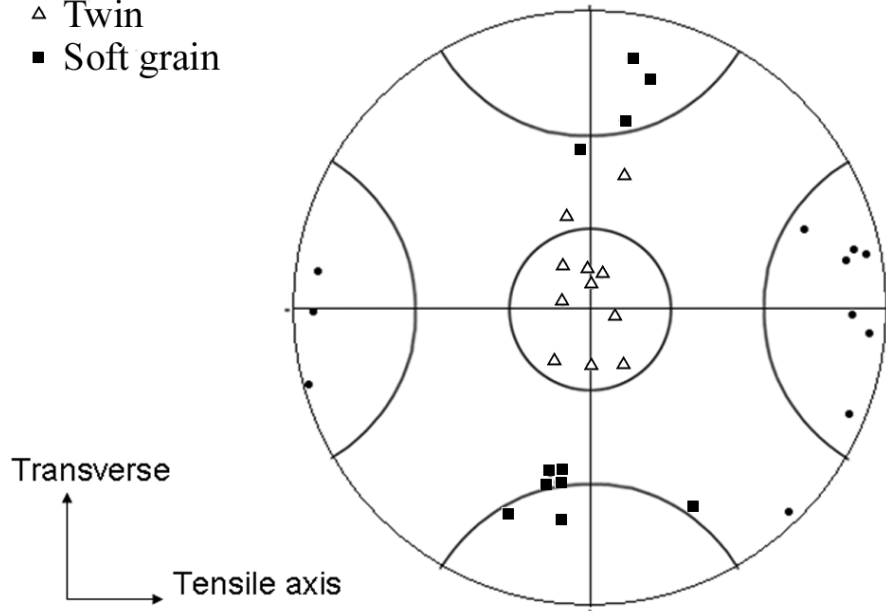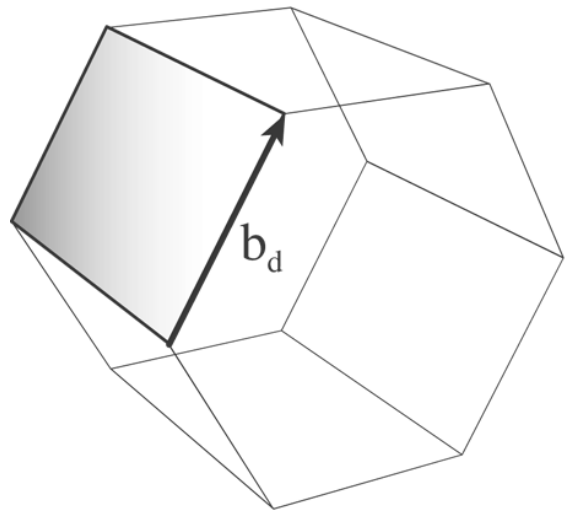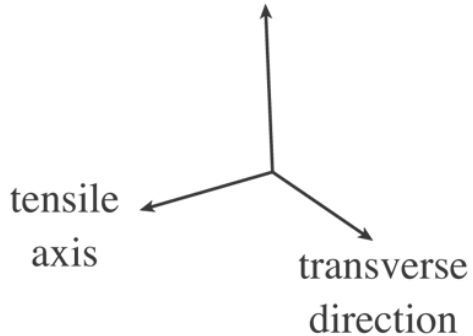
Figure 4.8 The {0001} poles of parent grains, twins, and neighboring soft grains of the 11 S+T

pairs are mostly within a ~35° cone along the tensile, sample normal, and transverse axes,

respectively (the drawn cones are 30°).

soft grain orientation

hard grain orientation

b_d

b_t

after twinning

sample normal

tensile axis

transverse direction
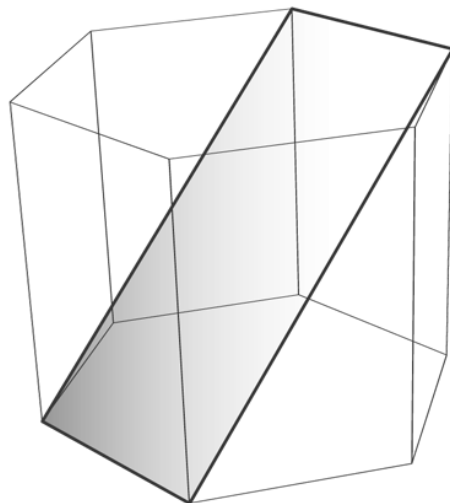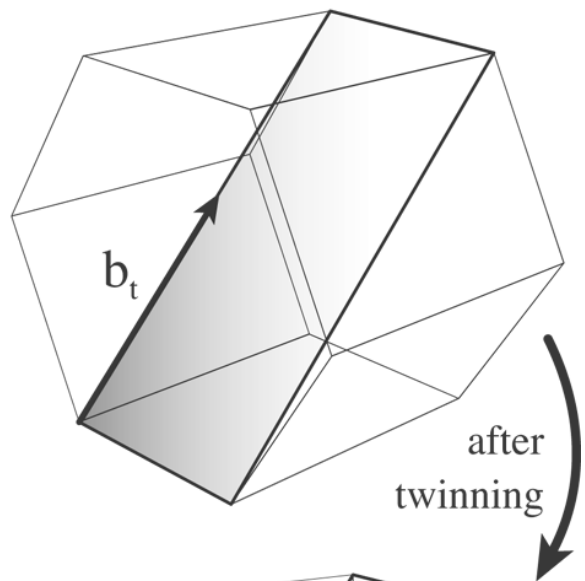
Figure 4.9 As prismatic slip stimulated twin nucleation occurs by slip transfer, the preferred c-axis orientation of soft grains along the transverse direction dictates that the c-axes of twins are close to the sample normal.

4.6 Critical Factors for Slip-stimulated Twin Nucleation

Since it has already been shown that grain pairs displaying slip-stimulated twins are associated with a high m', it is important to check if a high m' will always correlate strongly to twin nucleation in a soft/hard grain pair. As a counterpart to the S+T pairs, an S+0 grain pair is defined as a soft/hard grain pair where distinct prismatic slip bands appear in the soft grain while no deformation twins nucleated at the boundary in the hard grain. 15 S+0 grain pairs (4 in B-0 and 11 in B-45) were identified in the two samples. The same geometric parameters (m_t, ψ, κ, m') were calculated for these S+0 pairs. One S+0 example is the 43-44 grain pair shown in Figure 4.5, where no twin activity was observed in grain 44. The highest m' in this S+0 grain pair is 0.825 (see Table 4.5), lower than the highest m' in any of the three S+T examples shown previously. Since the operating twinning system in each S+T pair always had the highest m', the twinning system with the highest m' in each S+0 pair is accordingly defined as the potential twinning system for this grain pair. Figure 4.10 shows the m' and m_t of the operating twinning systems in the 11 S+T pairs, as well as the m' and m_t of the potential twinning systems in the 15 S+0 pairs. In general, S+T pairs have larger m' than the S+0 pairs. In fact, only two S+0 pairs with m' values larger than 0.9 have been indentified, one of which is shown in Figure 4.2(a): grain 16 (soft grain) and 18 (hard grain). In these two cases, it is not clear if further strain would result in slip stimulated twin nucleation. Most of the S+T pairs concentrate near the upper right corner, suggesting that twin nucleation requires not only a high slip transfer parameter m', but also a relatively high twinning Schmid factor (m_t). Table 4.6 gives the mean value and the standard deviations of the four geometric parameters of the operating twinning systems in the 11 S+T pairs and the potential twinning systems in the 15 S+0 pairs. From this table, the m' of the

operating twinning systems in S+T pairs are consistently larger than the m' of the potential twinning systems in S+0 pairs. There is only a 0.005 probability (α value) that an error will be made when rejecting this statement according to a non-parametrical statistical analysis (Mann-Whitney-Wilcoxon) by Darren E. Mason [Wang et al. (2010)]. From Table 4.6, the operating twinning systems in S+T pairs also have a larger mean value of m_t than the potential twinning systems in S+0 pairs. However, the same Mann-Whitney-Wilcoxon test gives a 0.082 probability that an error will be made when rejecting the hypothesis that the mean values of the m_t of the operating twinning systems of the S+T pairs and the mean values of the m_t of the potential twinning systems of the S+0 pairs are identical. Therefore, whether or not the prismatic slip in a soft grain would stimulate twins in the neighboring hard grain mostly depends on whether or not there is a twinning system in the hard grain that has a *sufficiently high m'* with the active slip system in the soft grain.

While all of the slip systems stimulating twin nucleation discussed to this point exhibited prismatic slip, dislocation slip on other systems can also stimulate twin nucleation. Such non-prismatic slip stimulated twin nucleation was only observed in one case in B-45, as indicated in Figure 4.10 as "pyr+T" (slip on a pyramidal <c+a> system activated twinning in the neighboring grain). The pyramidal <c+a> slip and the activated twinning system had a very high m', and both of them had a high Schmid factor. More T1 twins stimulated by slip have been observed in other samples later, making it a legitimate twin nucleation mechanism in Ti and other hexagonal metals.
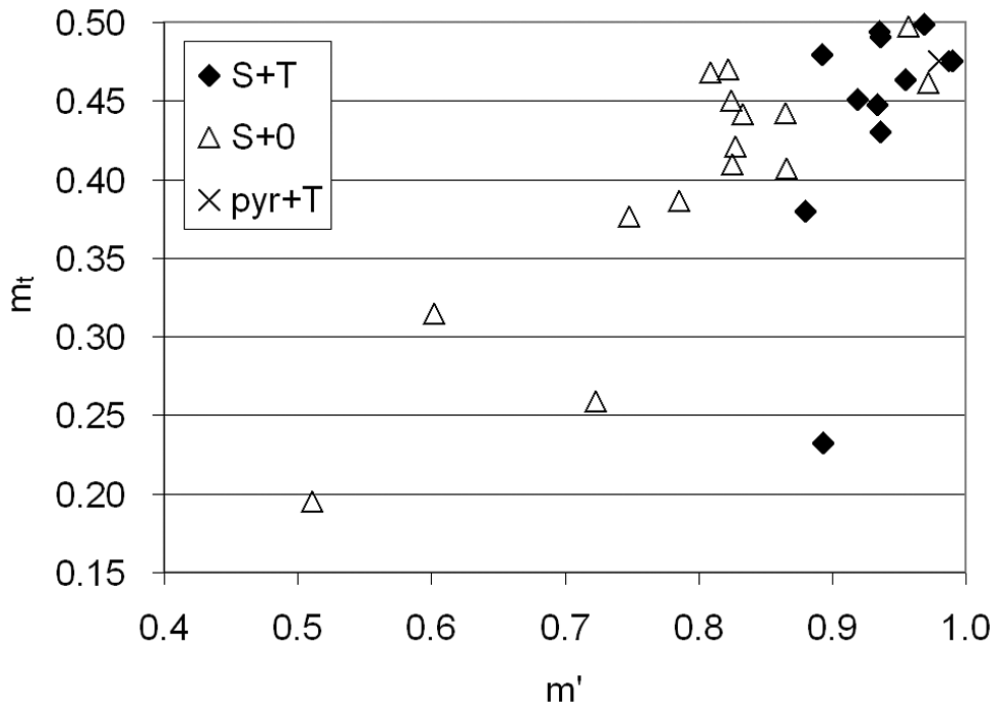
Figure 4.10 Distributions of *m'* and m_t corresponding to the two populations of 11 operating

twinning systems and 15 potential twinning systems. *m'* appears to be a more effective

parameter than m_t to distinguish between S+0 and S+T populations. Pyramidal slip is also able

to stimulate twin nucleation.

Table 4.5 Geometric deformation system analysis for grains 43 and 44 in Figure 4.5

T1 Twinning systems	m_t	ψ	κ	*m'*
$(\bar{1}012)[10\bar{1}1]$	0.457	68.9°	64.9°	0.153
$(10\bar{1}2)[\bar{1}011]$	0.451	34.7°	77.2°	0.182
$(1\bar{1}02)[\bar{1}101]$	0.451	6.0°	34.0°	**0.825**
$(0\bar{1}12)[01\bar{1}1]$	0.446	40.2°	21.4°	0.711
$(\bar{1}102)[1\bar{1}01]$	0.404	79.2°	79.5°	0.034
$(01\bar{1}2)[0\bar{1}11]$	0.392	65.3°	73.5°	0.119
None of the six twinning systems was activated				

Table 4.6 Geometric parameters of the operating twinning systems in the 11 S+T pairs and the

potential twinning systems in the 15 S+0 pairs

	m_t	ψ	κ	*m'*
Mean (S+T)	0.440	12.7°	14.5°	0.931
S. D. (S+T)	0.077	6.2°	8.0°	0.034
Mean (S+0)	0.400	22.8°	25.4°	0.798
S. D. (S+0)	0.077	12.0°	13.3°	0.122

4.7 Summary

Prismatic slip is the most active slip mode in commercial purity Ti. When prismatic slip bands impact a grain boundary, they can stimulate T1 twins in the neighboring hard grain and form S+T pairs. In all S+T examples, the operating twinning system always had the highest m' (slip transfer parameter) with the stimulating prismatic slip system. In this slip-stimulated twin nucleation process, m', as a local factor, is more important than the twinning Schmid factor (a global factor).

The results in this chapter show that twinning has a strong dependence on the local microstructure. To incorporate this slip-stimulated twin nucleation mechanism into crystal plasticity models, CPFEM seems to be the only choice, since neither Taylor model nor the self-consistent method has the ability to capture highly localized shear.

Chapter 5

Nucleation of Paired Twins at Grain Boundaries

This chapter studies another twin nucleation mechanism in polycrystalline Ti. Twin nucleation stimulated by another twin from adjacent grains has been observed at many grain boundaries, with one example shown in Figure 4.7. At some other grain boundaries, a twin in grain A and a twin in grain B appear to have nucleated simultaneously from the same place on the grain boundary. Such twin-twin correlations are referred to as T+T, as a counterpart to S+T. Based on the 26 T+T pairs identified in one sample (CP 2-2), factors including twin system alignment, twinning Schmid factor, disorientation of the parent grains, and parent grain size were assessed. An indicative combination of geometric conditions was identified that can account for the formation of most of the observed T+T pairs. The content in this chapter was published in a journal paper [Wang L., Eisenlohr P., Yang Y., Bieler T.R., Crimp M.A., 2010. Nucleation of paired twins at grain boundaries in titanium. Scripta Materialia 63, 827-830]. A reprint permit has been obtained from that journal.

5.1 Experiment and Observation of Twins

A commercial purity titanium specimen with dimensions 25×3×2.5 mm^3 was used for this study. The specimen has a moderate {0001} texture that is about 6 times intensity of a random texture along its longitudinal direction. (This value is smaller than the value in B-0 and B-45, though all three specimens were from the same plate). The specimen was deformed by four-point bending to about 2% tensile strain in the center of the 25×3 mm^2 surface. Prior to deformation, EBSD mapping was performed on a region of approximately 5×3 mm^2 in the center of that specimen surface using a JEOL JSM6500F microscope equipped with a TSL OIM system. Figure 5.1 shows the inverse pole figure map of this region, which contains 1980 grains according to the automatic grain counting software. Figure 5.1 shows this region contains many hard grains having their c-axes nearly parallel to the tensile axis. Such a texture geometrically favors tensile twinning and pyramidal <c+a> slip, while prismatic <a> slip is suppressed. The mapped region exhibited only 175 grains (~ 9 %) with a Schmid factor greater than 0.4 for prismatic slip, but 773 grains (~ 40 %) in which at least one T1 twinning system had a twinning Schmid factor greater than 0.4. After bending, T1 twins were found in 116 grains. Because there are not many soft grains in this specimen, one would expect less slip stimulated twins (S+T). In only 14 grains, twins were observed to have a correlation with slip bands in a neighboring grain. Figure 5.2 shows one S+T example in this sample. On the other hand, a total of 26 T+T grain pairs were identified, which account for twins in 45 grains, 39% of the number of grains containing T1 twins (The remaining twins found in 57 grains belonged to the 0+T category). Figure 5.3 shows two T+T examples. These T+T pairs might form as a result of a twin impacting a grain boundary to stimulate the nucleation of an accommodating twin in the neighboring grain, as is

the case in Figure 5.3(a). Alternatively, these T+T pairs might mutually nucleate at the same location on the grain boundary and grow into their respective parent grains, as suggested by the tapering of twins towards the center of the parent grains exemplified in Figure 5.3(b). T+T events have also been observed in Mg and reported recently [Wang J, et al. (2010)], implying that T+T twin nucleation could be a general source of twinning in hexagonal metals. Understanding of conditions that lead to T+T events is hence desirable.
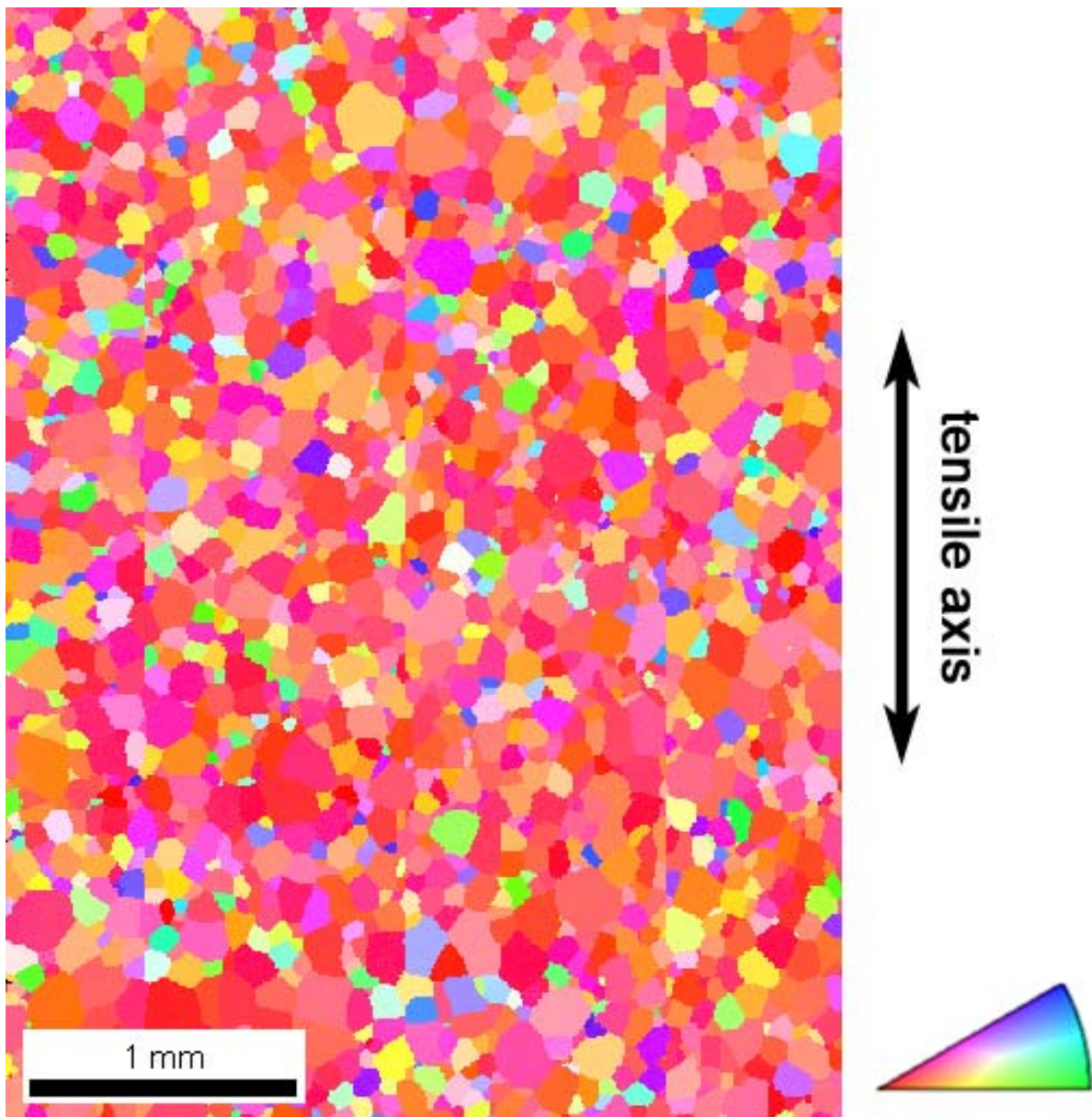
Figure 5.1 From the inverse pole figure map, most grains in the mapped region are hard grains, whose c-axes are close to the tensile axis. This map was from the combination of multiple EBSD scans; due to the tilt and beam distortion, discontinuity between neighboring scans can be seen.
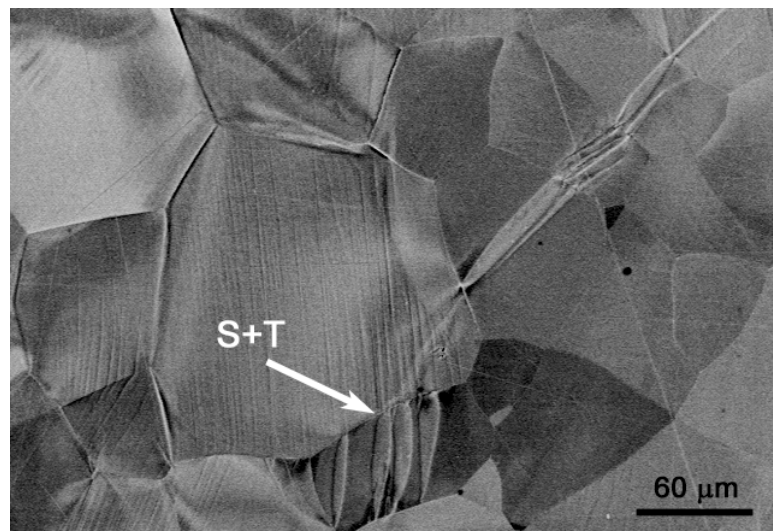
Figure 5.2 An S+T example identified in this sample
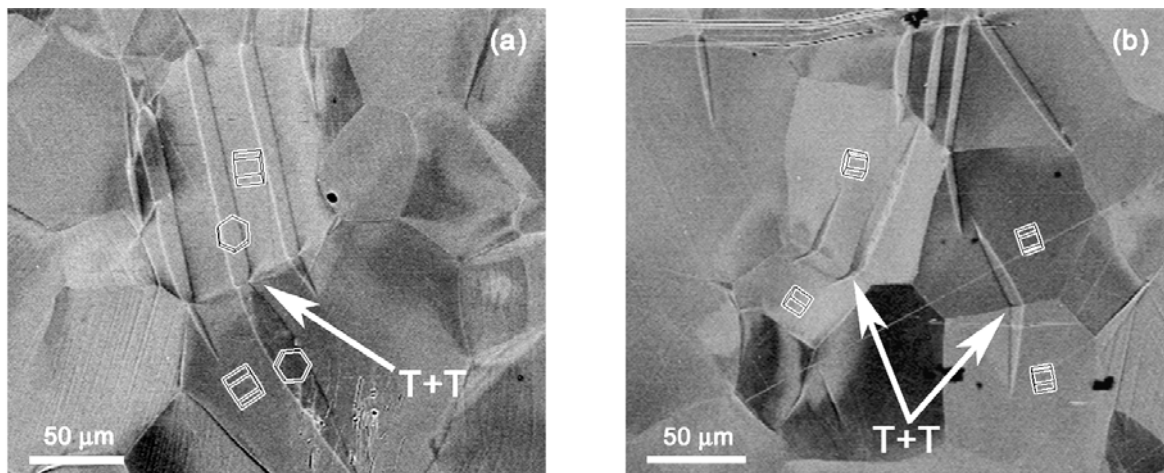
Figure 5.3 Backscattered electron images showing matching pairs of twins (T+T) at grain boundaries. (a) Twins in the upper grain seemed to have stimulated the nucleation of twins in the lower grain at the grain boundary. (b) Two T+T pairs where it appears that both twins nucleated from the same location on the grain boundary and grew into the parent grains in opposite directions.

5.2 Crystallographic Analysis of T+T Grain Pairs

5.2.1 Grain size effect

Many studies have shown a positive grain size dependence of twinning, and the Hall–Petch slope

for twinning is found to be much higher than that for slip [Song et al. (1995), El-Danaf et al.

(1999), Meyers et al. (2001), Lu et al. (2004, 2009), Yu et al. (2010)]. Consistent with these

results, twins are more frequently observed in large grains. The distribution of the grain average

cross section is close to log-normal for the three investigated populations of (a) all 1980 grains,

(b) the total 116 grains exhibiting twins, and (c) the subset of those grains comprising the 26

T+T pairs. The distribution in case (a) is shifted relative to (b) and (c) by about a factor of two,

such that the median cross section of all grains in the mapped region is $4.5{\times}10^3$ μm^2, while that

of the T+T subset is $7{\times}10^3$ μm^2 and that of all grains exhibiting twins is $9{\times}10^3$ μm^2, i.e. about

twice as large as the median grain size. These results suggest that grains where T+T pairs

developed do not have a significant difference in size compared with other grains showing

twinning.

5.2.2 Schmid factor of operating twinning systems in T+T pairs

In each of the 26 T+T grain pairs, the operating twinning systems on both sides, termed A and B,

were identified by the method described in section 3.1. The Schmid factor of the operating

twinning systems was calculated for each T+T pair, assuming a uniaxial tensile stress along the

bending direction. Figure 5.4 shows that all T+T pairs have at least one operating twinning

system whose Schmid factor was larger than 0.4. In some T+T events, the twinning Schmid

factor in one grain (A or B) is as much as 50% larger than the other (B or A). Such a large

spread suggests that either a significant deviation from the global tensile stress is present at the

local level, or twin nucleation at the grain boundaries involves factors other than merely the

resolved shear stress on the twinning system, e.g. the stress concentration induced by grain

boundary constraints, dislocation pile-ups at grain boundaries, or emission of grain boundary

defects (GBDs) [Beyerlein et al. (2008, 2010a), Wang J et al. (2010)].

5.2.3 Alignment of operating twinning systems in T+T pairs

Similar to slip-stimulated twinning (S+T) discussed in Chapter 4, T+T events are essentially a

process of strain transfer across grain boundaries. Hence, the geometrical alignment between the

two operating twinning systems in two neighboring parent grains should be a critical factor for a

T+T event to occur. Such an alignment can be described by a geometrical parameter $m' = \cos$

$\kappa \cdot \cos \psi$, where κ and ψ are the angles between twinning Burgers vectors and twinning plane

normals of the two operating twinning systems, respectively. In most T+T pairs, good

crystallographic alignment, as defined by a high m', was found between the two operating

twinning systems, as shown in Figure 5.5. Twenty T+T pairs had $m' > 0.8$, with fifteen of these

having $m' > 0.9$. (High m' T+T pairs concentrate at the upper-right corner of Figure 5.5, which

was enlarged and shown again in the otherwise empty lower left corner.) Among the six T+T

pairs with $m' < 0.8$, four had a large twinning plane misalignment ($\cos \psi$ is low), but a relatively

small twinning Burgers vector misalignment ($\cos \kappa > 0.9$, $\kappa < 25°$). This suggests that a small κ

may be more important than a small ψ in inciting a T+T event. Notably, there is one outlier in

Figure 5.5 with m' of 0.10 ($\kappa = 73°$, $\psi = 68°$). In this grain pair, each identified twinning system

actually had a potential companion twinning system with an $m' > 0.95$ in the other grain. It is

not clear why the twin pair with large compatibility did not nucleate, while the observed pair

with a much lower m' did.
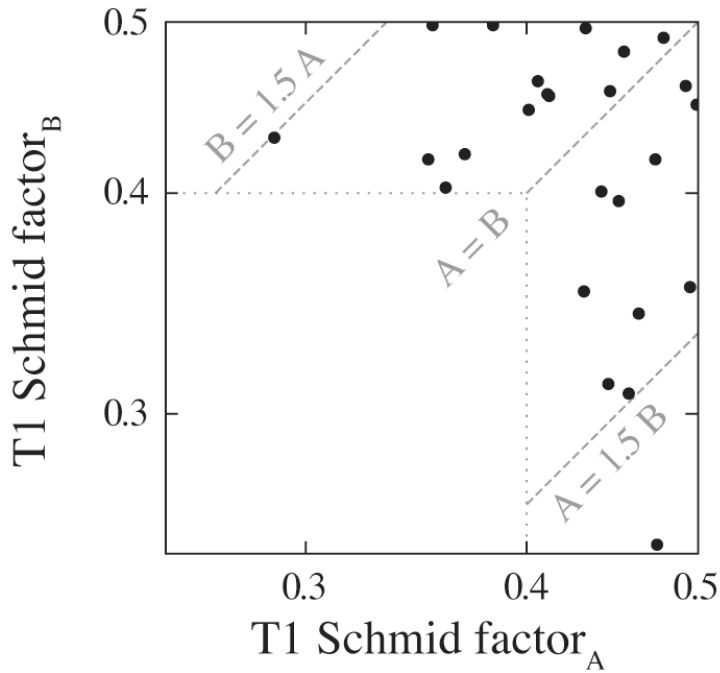
Figure 5.4 Correlation of Schmid factors for the activated T1 twinning system in grains A and B for each of the 26 T+T grain pairs. In all pairs at least one Schmid factor is larger than 0.4 (dotted demarcation). For some pairs the two operating twinning systems had significantly differing Schmid factors, exceeding the factor of 1.5 in one case.
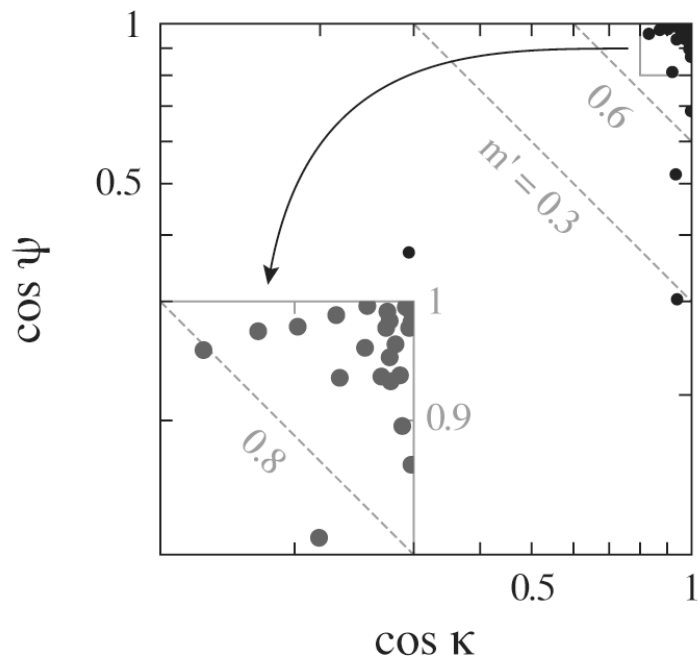
Figure 5.5 Correlation between twinning Burgers vector misalignment (κ) and twinning plane misalignment (ψ) in all 26 T+T pairs. In most T+T pairs, a high $m' = \cos \kappa \cdot \cos \psi > 0.8$ was identified between operating twinning systems (see enlarged inset).

5.3 Preferred Grain Boundaries for T+T to Form

In a recent paper, Wang J et al. (2010) observed that T+T events in Mg occurred most frequently at low-disorientation grain boundaries (disorientation is the smallest angle value of all possible misorientations due to crystal symmetry). This is also observed in the present work. Figure 5.6 (top) compares the distributions of grain boundary disorientation (gray - rotation angle θ around a particular axis) and c-axis misalignment (black - ϕ,) among (a) the 26 grain boundaries displaying T+T (T+T pairs), (b) all 5675 mapped grain boundaries, and (c) pairs of randomly oriented grains. All three distributions of c-axis misalignment fall systematically to the left of the corresponding distributions of boundary disorientation since the magnitude of c-axis misalignment cannot exceed the boundary disorientation, and is typically less. Distributions for cases (b) and (c) both extend up to the maximum of 94° possible for hexagonal crystal symmetry [Heinz et al. (1991)]. The distinct shift towards smaller angles for (b) in comparison to (c) results from the preferred orientation distribution (texture) in the sample. Both distributions of the T+T pairs in case (a) extend only up to about 45° and are much narrower than those in cases (b) and (c). Half of all observed T+T pairs fall below 15° in c-axis misalignment and 23° in boundary disorientation (see median values indicated by the dashed lines in Figure 5.6 top).

The high concentration of boundary disorientation and c-axis misalignment observed at small angles for T+T events (Figure 5.6 top) can be interpreted as the necessity to have a geometrically well-aligned pair of twin systems. As an illustration, the distributions of *m'* as function of boundary disorientation and c-axis misalignment, were calculated based on a population of 10^5 theoretical grain pairs. Each grain in these pairs was randomly oriented according to a unit

quaternion $q = \left(\sqrt{r_3}\cos 2\pi r_1, \sqrt{1-r_3}\sin 2\pi r_2, \sqrt{1-r_3}\cos 2\pi r_2, \sqrt{r_3}\sin 2\pi r_1,\right)$, with random

numbers r_1, r_2, r_3 uniformly distributed from 0 to 1. From the misorientation between grains α

and β, $q^{mis} = q_\alpha^{-1} q_\beta$, their disorientation was found by applying the $i = 1, \ldots, 12$ hexagonal

lattice symmetry rotations, q_i^{sym}, and from the resulting quaternions, $q_i^{sym} q_i^{mis}$, selecting the

one with the minimum rotation angle. Then, for each of the 10^5 grain pairs, the 36 values of m'

resulting from 6×6 twin system combinations per pair were collected in 3° increments of

boundary disorientation and c-axis misalignment.

Figure 5.6 shows the average number of twinning system pairs for which m' exceeds the

indicated value at either given boundary disorientation (center) or c-axis misalignment (bottom).

For example, with a c-axis misalignment $\phi \approx 10°$ ($\cos\phi \approx 0.98$), there are on average about 5

twinning system combinations or, equivalently, an overall fraction of 0.14 ($\approx$5/36) with m'

exceeding 0.9. At very low boundary disorientations ($\cos\theta \rightarrow 1$) the isolines of m' merge

because the 6 pairings of identical twinning systems (e.g. $(10\bar{1}2)[\bar{1}011]$ with $(10\bar{1}2)[\bar{1}011]$,

$(01\bar{1}2)[0\bar{1}11]$ with $(01\bar{1}2)[0\bar{1}11]$, etc) match very well, while any of the 30 other combinations

falls below the lower limit of 0.7 (Figure 5.6 center). There is a wider spread of m' observed in

the limit of $\cos\phi \rightarrow 1$ in Figure 4.6 bottom because the c-axis misalignment can be low even up

to moderate (i.e. 30°, $\cos\theta > 0.86$) boundary disorientation shown in the center plot. A rather

tight limit is set by $\cos\theta$ and $\cos\phi$ on the maximum observable m' such that the isolines of m'

drop for both measures quite steeply with increasing angle on the abscissa (Figure 5.6 center and

bottom). Thus, the fraction of potential twin pairs featuring high m' values rapidly drops with

the increasing c-axis misalignment *or* boundary disorientation. Since the slope is lower in the case of c-axis misalignment, its fraction of high *m'* candidates is always slightly lower than that of boundary disorientation for the same rotation angle. As a summary of Figure 5.6, T+T events most likely occurs at grain boundaries of low disorientation because these grain orientation combinations provide more twinning system pairs with large *m'*.

Nucleation of T+T pairs probably needs the participation of grain boundary defects. Among many factors, the nominal resolved shear stress on a grain boundary will affect the generation and movement of grain boundary defects, which in turn influence the activation of T+T pairs. The exact angle between the grain boundary plane and the tensile axis is unknown without knowing the grain boundary subsurface inclination. However, grain boundaries with their surface trace close to the tensile axis are more likely to have a higher resolved shear stress. Grain boundary trace orientation has been incorporated in the "fracture initiation parameter" to predict crack nucleation in TiAl [Simkin et al. (2003, 2007), Kumar et al. (2008), Bieler et al. (2009)]. Figure 5.7 shows the distribution of the angle between T+T grain boundaries' traces and the tensile axis. 18 out of 26 T+T grain boundaries have a surface trace that is less than 30° from the tensile axis. This result implies that a large resolved shear stress on a grain boundary may increase the chance of twin nucleation on it.
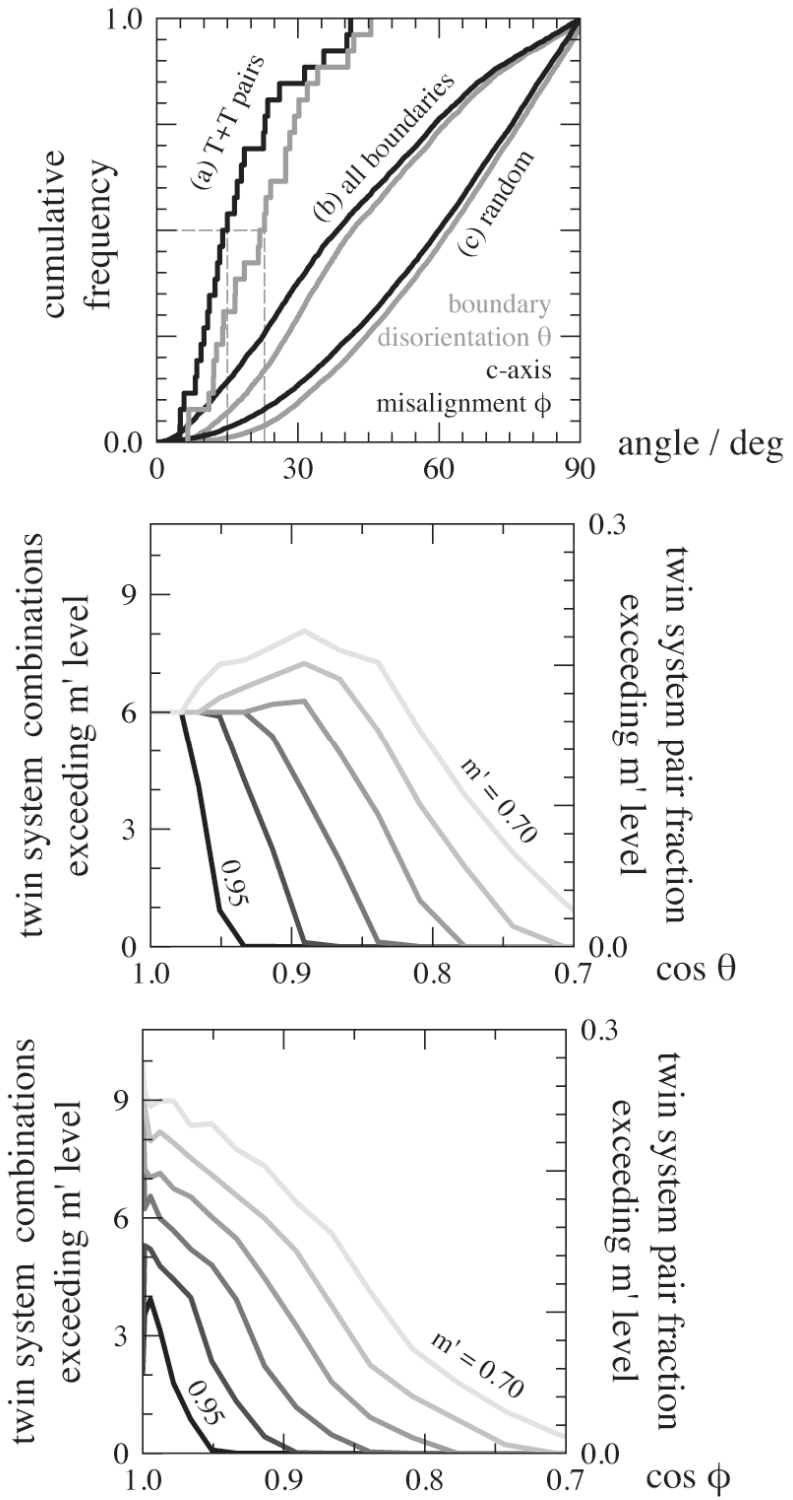
Figure 5.6 Distributions of c-axis misalignment (φ) and boundary disorientation (θ) for the 26

T+T pairs (top, a), all 5675 mapped grain boundaries (top, b), and pairs of randomly oriented

grains (top, c). Average number (left ordinate) and corresponding fraction (right ordinate) of twinning system pairs whose *m'* exceeds the indicated level at given boundary disorientation (center) or c-axis misalignment (bottom) based on 10^5 randomly oriented grain pairs.
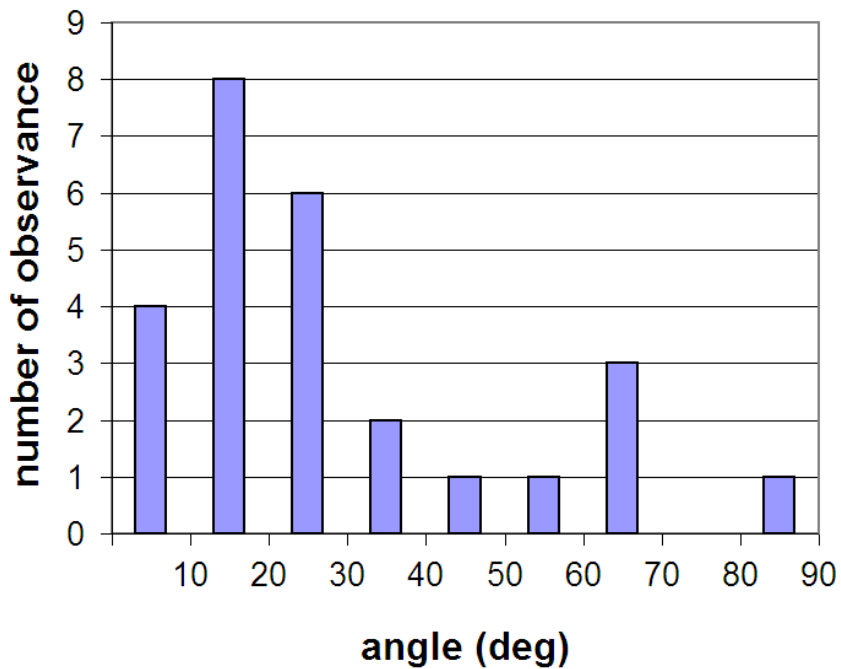
Figure 5.7 Distribution of the angle between T+T grain boundaries' traces and the tensile axis.

For example, eight T+T grain boundaries have their traces in the range of 10°~20° from the

tensile axis.

5.4 Summary

In general, grain boundaries where T+T pairs formed usually (but not strictly) satisfy the following conditions: (1) grain A and grain B have a pair of well-aligned T1 twinning systems ($m' > 0.8$) and at least one of them has a Schmid factor larger than 0.4; (which implies that (2) the c-axis misalignment between grains A and B is probably less than 25°); (3) the grain boundary trace is at a small angle with the tensile axis; and (4) the sizes of grain A and grain B are larger than the average grain size. Compared with other more localized factors that are difficult to characterize (e.g. dislocation pile-up, stress concentration, etc), the above four criteria for nucleation of T+T pairs can be conveniently implemented into a non-local CPFEM model.

Chapter 6

Characterizing Subsurface Microstructure and GNDs by DAXM

This chapter investigates two examples where Differential Aperture X-ray Microscopy (DAXM) was used to characterize subsurface microstructure and geometrically necessary dislocations (GNDs) in polycrystals. In the first example, line scans crossing three surface grains in specimen B-0 were conducted before and after deformation at the same place. Subsurface grain geometry was revealed from the scan before deformation. After deformation, streaked peaks are often observed, which according to Chapter 3, indicates lattice rotation and the presence of geometrically necessary dislocations (GNDs). The slip system of the dominant GND type was estimated using streaked peak analysis, and the result is consistent with the surface slip trace. In the second example, the two ends of a twin in Figure 4.3 (from specimen B-45) were characterized by two DAXM area scans. 3D morphology and dislocation content of these two regions were analyzed. It was found that GNDs developed at grain boundaries where slip transfer was difficult. The experimental and analysis results discussed in this chapter have been accomplished in collaboration with Wenjun Liu at Argonne National Laboratory (ANL) and Rozaliya Barabash at Oak Ridge National Laboratory (ORNL). The first example in this chapter was published in a journal paper [Wang L., Barabash R.I., Yang Y., Bieler T.R., Crimp M.A., Eisenlohr P., Liu W., Ice G.E., 2011. Experimental characterization and crystal plasticity modeling of heterogeneous deformation in polycrystalline α-Ti. Metall. Mater. Trans. A, 42, 626-635.] A reprint permit has been obtained from the journal.

6.1 Example 1 — Line Scans Near a Triple Junction

Figure 6.1 shows the result of a depth resolved line scan near the triple junction of three grains in an undeformed sample. The length of the line scan was 48μm (step size = 2μm). Prior to deformation, surface grain orientation and grain geometry in this region had been measured by EBSD (Figure 6.2). Figures 6.1 and 6.2 use the same grey scale scheme: grains with their c-axis close to the horizontal direction (tensile axis) are towards black, while grains with their c-axis perpendicular to the horizontal direction are towards white. Three surface grains (grains 3, 4, and 5) and three subsurface grains (grains U1, U2, and U3) are shown in Figure 6.1(a). Figure 6.1(b) shows an example depth-resolved Laue pattern, collected near the boundary between grains 3 and 5. This pattern belongs to the voxel marked by the small white box in the crystal orientation map in Figure 6.1(a). Diffraction peaks from both grains 3 and 5 were observed and indexed in Figure 6.1(b).
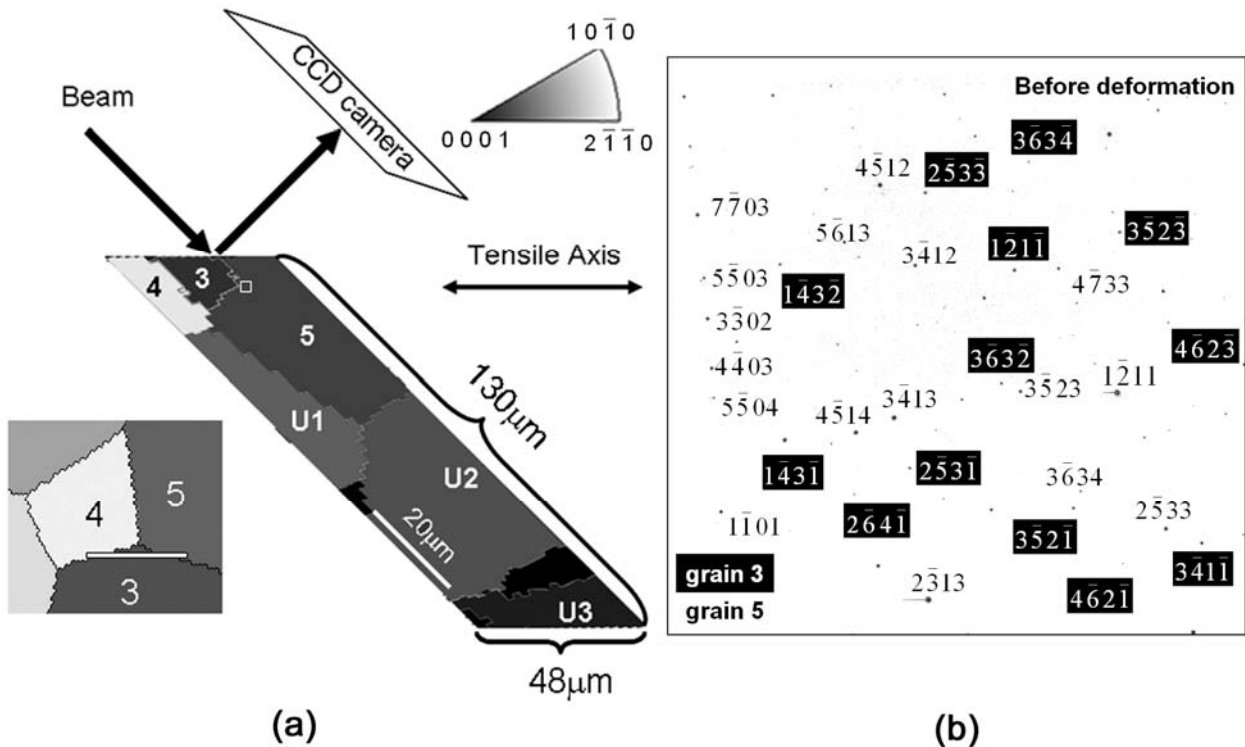
Figure 6.1 (a) The result of a DAXM line scan near the triple junction of grains 3-5 in an undeformed sample. The length of the scan was 48μm, and its position on the surface is shown in the map in the lower left corner (white line). Subsurface grain structure at a depth of about 130μm was revealed by this line scan. (b) A depth-resolved Laue pattern from white box next to the 3-5 grain boundary. Peaks from both grains are indexed with indices from grain 5 appearing in black text and indices from grain 3 as white text in black boxes.
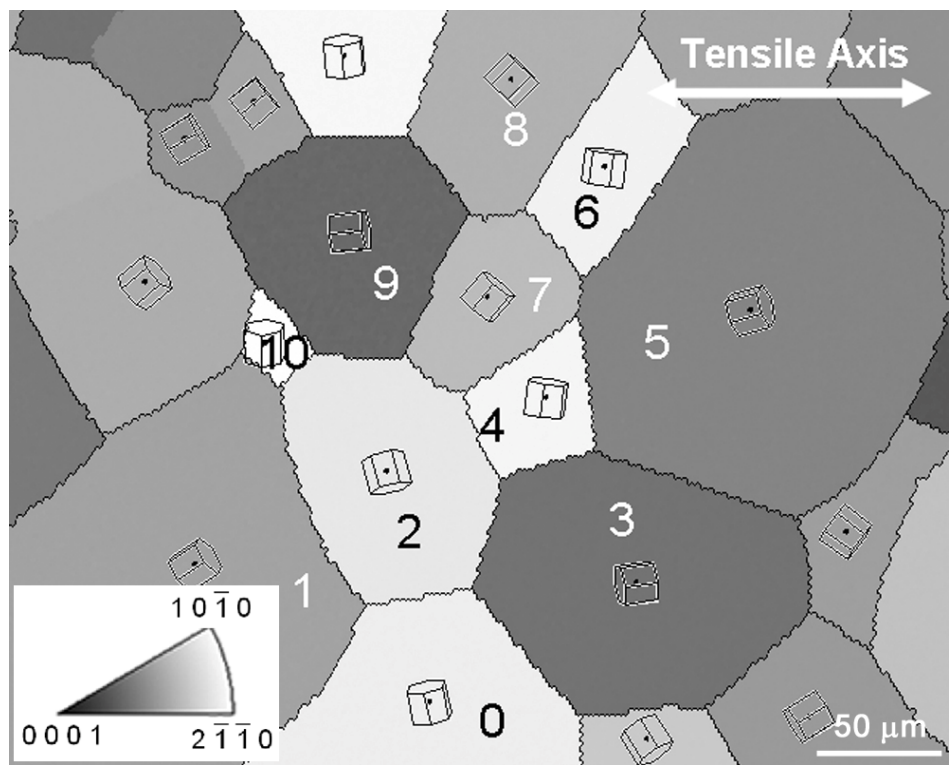
Figure 6.2 Surface grain orientation and grain geometry around the DAXM line scan in Figure

6.1 measured by EBSD.

After the initial EBSD and DAXM characterization, the sample was deformed by four-point bending about its transverse direction to achieve a surface tensile strain of ~ 8%. Figure 6.3 shows a backscattered electron SEM image of the same region after deformation. In some grains, slip bands were observed. Table 6.1 lists the identified slip systems for surface slip bands in grains 0–10 using slip trace analysis. Prismatic <a> slip was the dominant slip mode. However, basal slip and pyramidal <c+a> slip were also observed. To characterize how deformation affects subsurface microstructure, another DAXM line scan was performed at the same place near the triple junction of grains 3-5. Figure 6.4 shows a Laue pattern from grain 5 collected after deformation, about 15μm below the surface and near the 3-5 grain boundary. In contrast to the reflections in the Laue pattern in Figure 6.1(b), the peaks in Figure 6.4 are extensively streaked due to deformation. The streaked peaks were indexed manually by comparing their relative positions with the indexed peaks of grain 5 in Figure 6.1(b).

Using Equations (3.3–3.7) and the crystal orientation of grain 5, the theoretical streak directions at different diffraction peaks were estimated based upon the Nye's tensor for edge dislocations on each of the 24 slip systems of α-Ti (basal slip listed as 1–3; prismatic slip 4–6; pyramidal <a> slip 7–12; pyramidal <c+a> slip 13–24). The three "star patterns" along the top of Figure 6.4 show the theoretical streak direction of all 24 slip systems at diffraction peaks $(4\bar{5}14)$, $(3\bar{5}21)$ and $(2\bar{5}33)$ respectively. The red arrows beside these three peaks indicated the calculation results for slip system 1, $(0001)[\bar{2}110]$. From Figure 6.4, the actual streak direction at these three peaks (as well as other peaks) are very close to the theoretical peak streak direction based on edge GNDs from slip system 1. (Slip system 17 is also close, but does not match as well as

slip system 1, especially for peak $(2\bar{5}33)$.) From Table 6.1, surface slip bands in grain 5 near

the boundary with grain 3 also resulted from the activation of slip system $(0001)[\bar{2}110]$. Given

that the Laue pattern in Figure 6.4 belongs to a voxel that's close to the 3-5 grain boundary and

not far from the surface, GNDs in that voxel should be belong to slip system $(0001)[\bar{2}110]$.

To check the above result, Laue pattern simulation was performed with by R.I Barabash at Oak

Ridge National Lab. That approach directly uses Equation 3.1, and it is more accurate and

versatile than the simplified method using Equations (3.3–3.7). Assuming specific GNDs and

that a certain amount of background GNDs are present within the volume illuminated by the

beam, Barabash numerically simulated diffraction intensity distribution around Laue reflections.

At each peak, the integral spread along the streak direction depends on the GND population and

the specific contrast factor of that peak. The integral spread along the narrow direction depends

on the square root of the total dislocation density [Barabash et al. (2001, 2003), Ice et al. (2007),

Ohashi et al. (2009)]. In fact, Laue pattern simulation can accurately predict the curvature in the

Laue reflections that is usually observed, and can be used to estimate (by fitting) the orientation

gradient and the density of GNDs in the selected region. In Figure 6.4, the simulated Laue

pattern for edge GNDs on slip system 1, $(0001)[\bar{2}110]$ matches the experimental Laue pattern

quite well. Simulations based upon <c+a> GNDs on slip systems 17 and 24 also gave a

reasonably good match, but not as close as the simulation for slip system 1. Laue pattern

simulation confirms that the subsurface GNDs in grain 5 were edge dislocations of the same

$(0001)[\bar{2}110]$ basal slip system as that responsible for the surface slip traces.
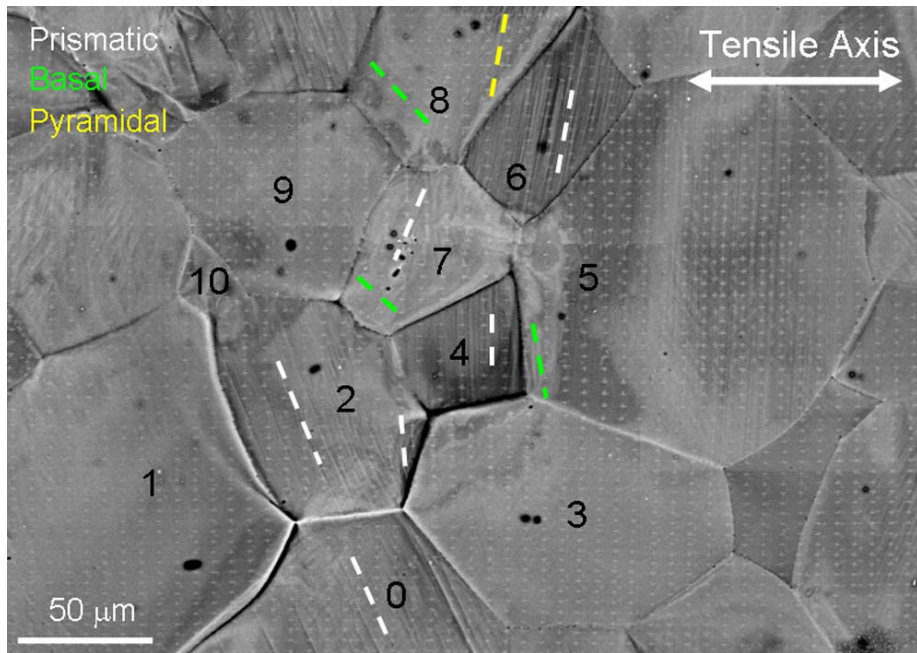
Figure 6.3 Backscattered electron image near grains 3-5 after 8% tensile strain by bending the specimen. Slip bands on the surface were identified by trace analysis. The detailed information of grain orientation, active slip system, and Schmid factor are shown in Table 6.1.

Table 6.1 Active slip systems for surface slip bands using slip trace analysis for grains 0–10.

Grain No	Bunge Euler angles before deformation $(\varphi_1, \Phi, \varphi_2)$ (deg)	observed slip traces	identified active slip system(s)	Schmid Factors
0	(281, 74, 262)	prismatic	$(1\bar{1}00)[\bar{1}\bar{1}20]$	0.454
1	(214, 70, 338)	N/A		
2	(105, 78, 61)	prismatic	$(1\bar{1}00)[\bar{1}\bar{1}20]$	0.435
2		prismatic	$(01\bar{1}0)[\bar{2}110]$	0.367
3	(188, 105, 156)	N/A		
4	(264, 81, 260)	prismatic	$(1\bar{1}00)[\bar{1}\bar{1}20]$	0.490
5	(16, 109, 315)	basal	$(0001)[\bar{2}110]$	0.378
6	(261, 85, 291)	prismatic	$(10\bar{1}0)[\bar{1}2\bar{1}0]$	0.480
7	(231, 81, 319)	prismatic	$(01\bar{1}0)[\bar{2}110]$	0.305
7		basal	$(0001)[\bar{1}\bar{1}20]$	0.477
8	(226, 88, 301)	basal	$(0001)[\bar{1}\bar{1}20]$	0.499
8		pyramidal	$(\bar{1}011)[\bar{2}11\bar{3}]$	0.347
9	(185, 78, 30)	N/A		
10	(271, 68, 261)	N/A		

Euler angles are defined with respect to x — transverse, y — tensile axis, z — sample normal.

$$4\bar{5}14 \qquad\qquad 3\bar{5}21 \qquad\qquad 2\bar{5}33$$
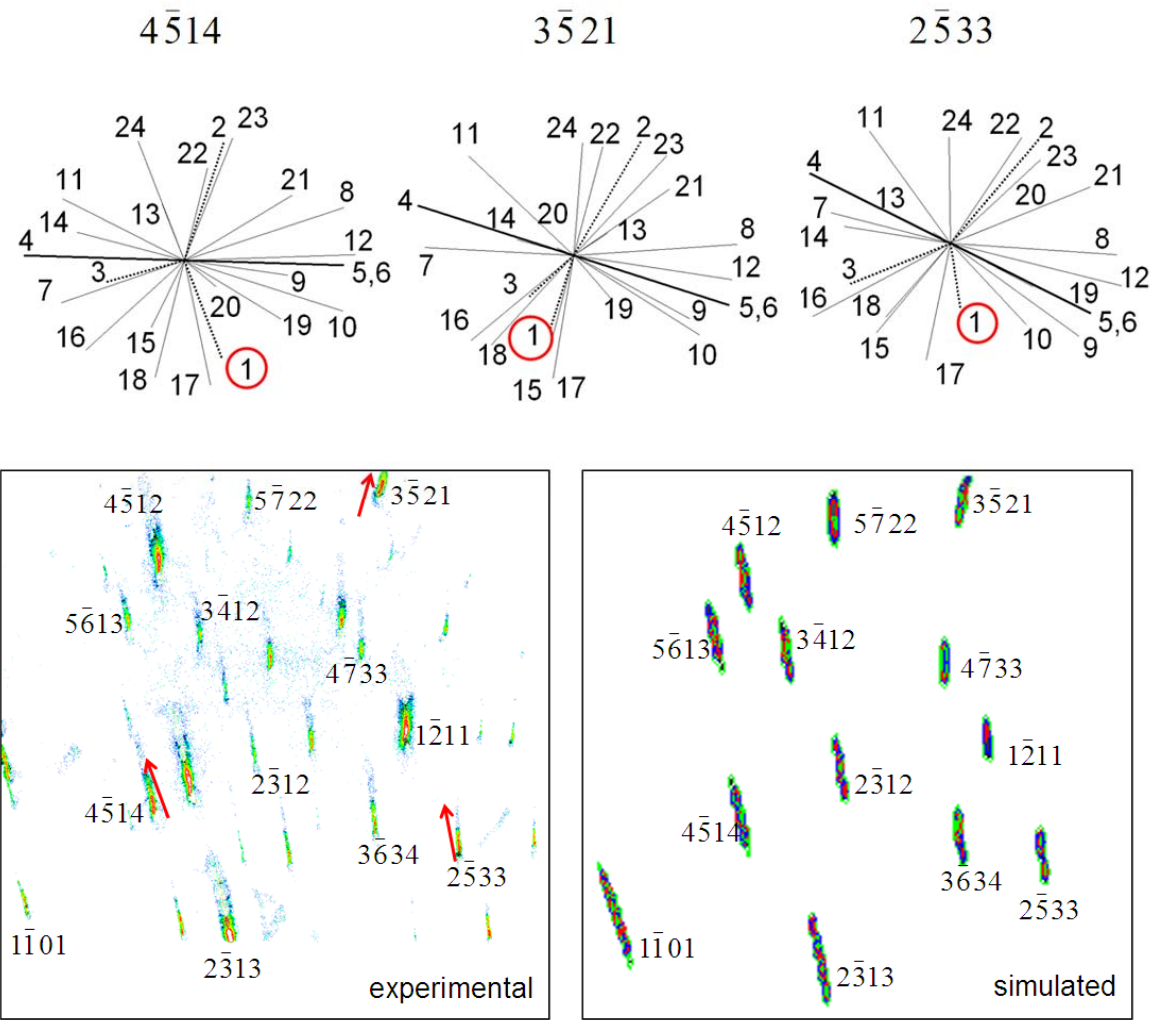
Figure 6.4 An experimental Laue pattern from grain 5 below the surface, reveals extensively

streaked Laue reflections. Theoretical streak directions at diffraction peaks $(3\bar{5}21)$, $(4\bar{5}14)$,

and $(2\bar{5}33)$ for all 24 slip systems are illustrated in star patterns above the diffraction patterns.

The relative length of each line in the star pattern reflects the projected length of the unit vector

ξ on the CCD screen. The theoretical streak direction (red arrows) for slip system 1,

$(0001)[\bar{2}110]$, are close to the experimental streak directions for most reflections. Laue pattern

simulation based on edge GNDs on slip system 1 matches the experimental Laue pattern.

6.2 Example 2 — Area Scans Near the Ends of a Twin

A DAXM line scan only characterizes the microstructure in a 2D space, with one dimension along the beam direction and the other along the beam scanning direction. For a full representation of microstructure, however, a 3D picture is necessary. 3D microstructure can be characterized nondestructively by performing an area scan by DAXM. But because an area scan is usually much more time consuming than a line scan, under the current beam speed only limited areas can be investigated.

One of the more interesting places for investigation is grain boundaries where deformation twins nucleated or terminated. The microstructure in Figure 4.3 has been intensively characterized, but the subsurface structure and dislocation content of the twins in grain 2, especially where they interact with grain boundaries, remains unknown. To address that, two DAXM area scans were performed: one at the 1-2 grain boundary where a twin nucleated, the other at the 2-3 grain boundary where that twin terminated. Both scans covered a rectangular surface region of 20×10 μm^2, with a step size of 2μm. The scanned regions are shown in Figure 6.5. Because the beam entered the sample surface from a 45 degree angle, an area scan actually probes a parallelepiped volume, as shown in Figure 6.5. One way to represent a 3D volume is by showing 2D sections of the parallelepiped at different depths. Each section has the same area as the surface scanned region (20×10 μm^2).

In Figure 6.5, the probed parallelepiped volume of the area scan at the 1-2 grain boundary almost entirely fell in grain 1. Only a few voxels near the upper-right corner of the scanned area show

characteristic diffraction peaks of the twin. None of the Laue patterns from this scan show

characteristic diffraction peaks of grain 2. Figure 6.6 shows a 2D section of the scanned volume.

The section was from 2 μm beneath the surface. Based on the characteristic diffraction peaks in

the 50 Laue patterns on each level, each pixel on this section is assigned a cyan color if its Laue

pattern has characteristic diffraction peaks from grain 1, or a turquoise color if its Laue pattern

has characteristic diffraction peaks from the twin. The 3 pixels that display moderately streaked

peaks are highlighted with a thick box, while the other 47 pixels show sharp peaks. The Laue

patterns of 4 pixels are shown in Figure 6.6: patterns 1 through pattern 3 are from grain 1, and

pattern 4 from the twin. The twin diffraction spots contain no evidence for GNDs. In contrast

with the strong topographic surface slip bands in grain 1, most Laue patterns from grain 1 have

sharp, rather than streaked peaks, which indicates that the subsurface region of grain 1 was also

almost free of GNDs. It is likely that most prismatic <a> dislocations generated in grain 1

moved out of grain 1 by forming slip bands on the surface. Another possibility is that they

"transferred" across the 1-2 grain boundary and participated in twin nucleation and propagation,

as has been discussed in Chapter 4. The most strongly streaked peak in grain 1 appears in

pattern 3. Peak streak analysis indicates that the GNDs that lead to the observed peak streak are

most likely screw type basal <a> dislocations $(0001)[1\bar{2}10]$, though edge type prismatic <a>

dislocations $(10\bar{1}0)[1\bar{2}10]$ are also possible. The red solid arrows and black dotted arrows near

three indexed peaks in pattern 3 represent the theoretical peak streak direction for screw

dislocations on $(0001)[1\bar{2}10]$ and edge dislocations on $(10\bar{1}0)[1\bar{2}10]$. The screw streak

direction is closer to the actual peak streak direction than the edge dislocations. By trace

analysis, the slip bands in grain 1 came from $(10\bar{1}0)[1\bar{2}10]$, and it has a Schmid factor of 0.478 that is much larger than the $(0001)[1\bar{2}10]$ screw dislocation system (SF=0.159). Given that these two slip systems have the same Burgers vector, screw dislocations on $(0001)[1\bar{2}10]$ could be the result of cross slip from the dominant $(10\bar{1}0)[1\bar{2}10]$ slip system. Constraint of the 1-2 grain boundary that did not facilitate slip transfer as a twin (the voxels with the streaked peak are some distance away from the location where the twin formed) could be the driving force for this process.
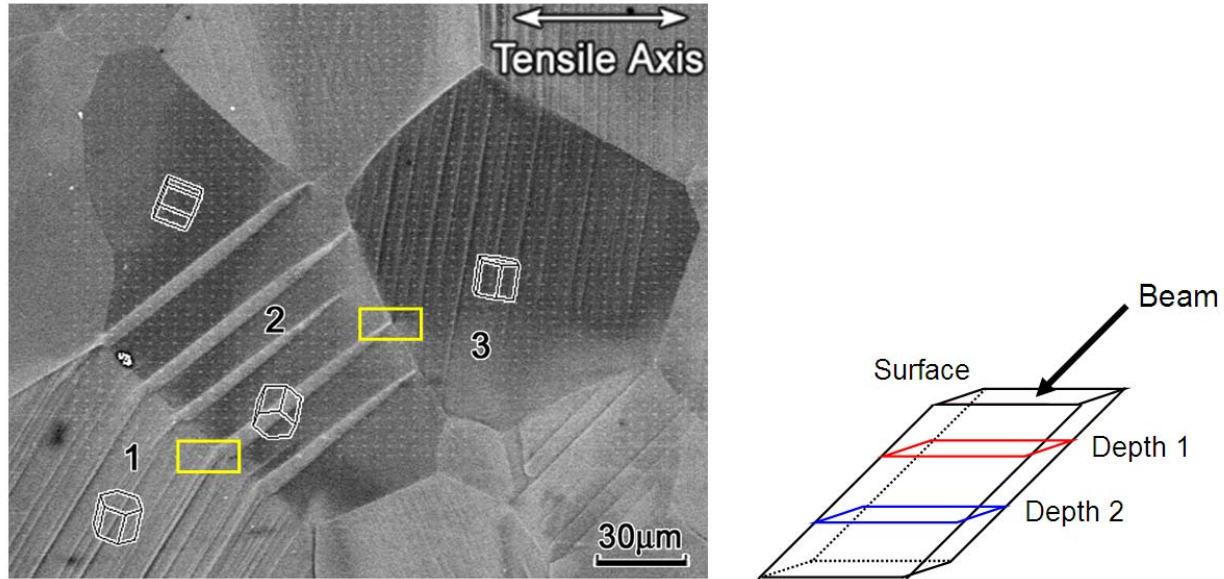
Figure 6.5 Two DAXM area scans (20×10 μm^2, step size=2μm) were performed at the 1-2 grain

and the 2-3 grain boundary. The scanned regions on the surface are indicated by the two yellow

boxes. A DAXM area scan probes a parallelepiped volume beneath the surface. Microstructure

in the 3D space can be visualized by showing 2D sections of the parallelepiped at different

depths.
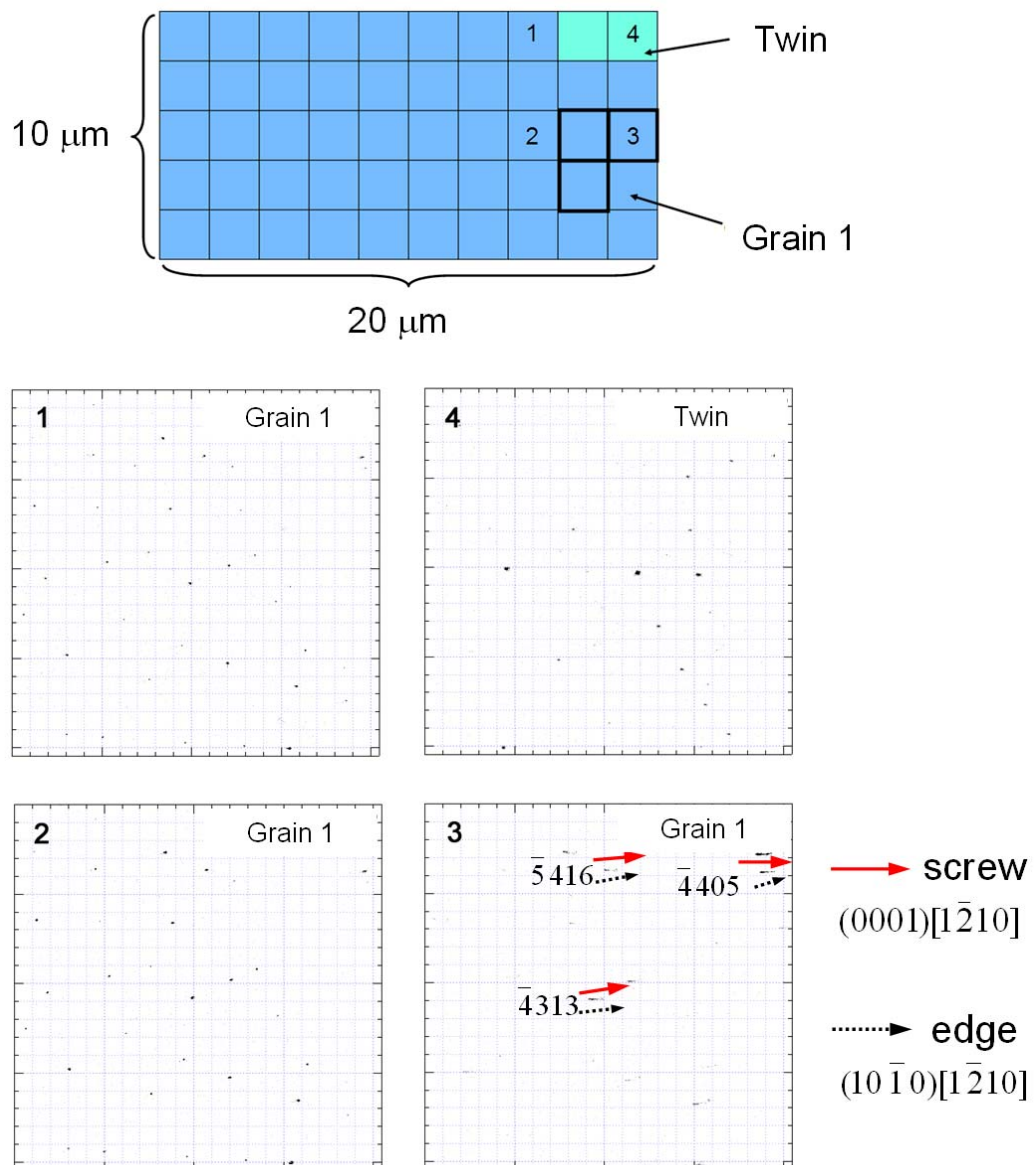
Figure 6.6 A section of the DAXM area scan near the 1-2 grain boundary 2 μm beneath the surface. Grain 1 and the twin are represented by cyan and turquoise color, respectively. The 3 pixels surrounded by thick boxes show moderately streaked peaks, while the other 47 pixels all show sharp peaks. Laue patterns of 4 pixels were shown. In pattern 3, the red solid arrows and the black dotted arrows near three indexed peaks represent the theoretical peak streak direction for $(0001)[1\bar{2}10]$ screw dislocations and $(10\bar{1}0)[1\bar{2}10]$ edge dislocations.

The area scan at the 2-3 grain boundary included grain 2, the twin, and grain 3. Figure 6.7 shows a section from that area scan. The section is also about 2 μm beneath the surface. Characteristic diffraction peaks of grain 2 (red color), grain 3 (blue color), and the twin (turquoise color) were observed at different locations. The three white voxels ahead of the tip of the twin have Laue patterns with hazy peaks. According to a few still recognizable peaks, all of the three voxels belong to grain 2 (e.g. pattern 5, and pattern 6 also has a couple of peaks from grain 3 in Figure 6.7). The hazy appearance of Laue patterns ahead of the twin tip indicated that local lattice was so heavily distorted that crystal planes are poorly defined there. This is probably due to the plastic accommodation and the associated emissary dislocations in the very vicinity of a twin that terminate in the matrix, as first studied by Sleeswyk (1962) in Fe and later observed in other materials [Mahajan et al. (1974), Vaidya et al. (1980)]. Laue patterns of selected voxels are shown in Figure 6.7. Pattern 1 shows a characteristic diffraction pattern for the twin. As with the other end of the twin (at the 1-2 grain boundary), no streaked peaks are observed in this pattern or any other Laue pattern from the twin. In other words, the twin has a very small number of GNDs near its two ends (because the peaks are slightly elliptical). Patterns 2 through 6 came from different places in grain 2, with patterns 5 and 6 ahead of the twin tip. The intensity threshold for these two patterns is set to be lower than the other patterns in order to make the weak peaks more visible. Even so, peaks in these two patterns are not very distinct. In addition, there is a large shift in peak positions from voxel 5 to voxel 6, which implies the existence of a large orientation rotation in front of the twin tip. Streaked peaks are present in the three patterns from grain 3, and the directions of streaked peaks in patterns 7 and 8 are different from that in pattern 9. Hence, grain 3 has a significant amount of GNDs, and there are at least two types of GNDs present. Peak streak analysis was performed to identify the slip systems of the GNDs in

118

grain 3. With the Euler angles ((φ_1, Φ, φ_2)= (261°, 87°, 97°)), theoretical streak directions for

peaks $(4\bar{3}\bar{1}2)$, $(5\bar{3}\bar{2}\bar{1})$, and $(4\bar{3}\bar{1}\bar{1})$ were calculated for edge GNDs for the 24 slip systems of

α-Ti shown in Figure 6.8 (basal slip is listed as 1–3, prismatic slip 4–6, pyramidal <a> slip 7–12,

and pyramidal <c+a> slip 13–24). For pattern 9, the three prismatic slip systems (4–6) match

the actual peak streak direction (see the red arrows near the three peaks). Among slip systems

4–6, slip system 5, $(10\bar{1}0)[1\bar{2}10]$, is favored by its high Schmid factor (= 0.467). The surface

trace of slip system 5 is also parallel to the surface slip bands in grain 3. For pattern 8 (as well as

pattern 7), the peak streak direction suggests the activation of slip system 8, $(10\bar{1}1)[1\bar{2}10]$ (see

the red arrows near the three reflections). This pyramidal <a> slip system has a high Schmid

factor (= 0.469) and its Burgers vector is same as that of slip system 5. Similar calculation was

also performed for screw GNDs on the 24 slip systems, but none of them would account for the

peak streak in pattern 9 or pattern 8. To conclude, edge GNDs on slip system $(10\bar{1}0)[1\bar{2}10]$

exist in the interior of grain 3, while edge GNDs on slip system $(10\bar{1}1)[1\bar{2}10]$ exist near the

grain boundary with grain 2.

Grain 1 and grain 3 both displayed prismatic slip bands that impacted boundaries with grain 2.

However, the density of GNDs in grain 3 was much higher than in grain 1 by comparing the

extent of the streak in these two grains. This difference can be accounted for by the slip transfer

effect. Near the 1-2 grain boundary, prismatic dislocations generated in grain 1, by slip transfer,

were quickly absorbed and transformed into the propagation of twinning dislocations in grain 2

(*m'* is 0.936 for this process). As a result, not many dislocations were left in grain 1. The prismatic dislocations generated in grain 3, however, could not transfer into grain 2, as the *m'* between the twin and the prismatic slip in grain 3 was 0.730, much lower than the average *m'* value in S+T pairs (Table 4.6). These prismatic dislocations piled up at the 3-2 grain boundary and caused lattice curvature and streaked peaks. Also, the small *m'* might be the reason that the twin terminated in grain 2 instead of further expanding along the 2-3 grain boundary.

A simple way to represent 3D microstructures is to place a few sections from various depths next to each other. The grain boundary inclination beneath the surface can be estimated using this information. Figure 6.9 shows three sections of the area scan at the 2-3 grain boundary. The section on the top is the one shown in Figure 6.7. The distance between neighboring sections in Figure 6.9 is 3.5μm. From the positions of the 2-3 grain boundary line at these three different depths, it is found that that grain boundary plane is almost perpendicular to the sample surface (the angle between the grain boundary plane normal and the surface normal is about 86°).

There are two issues yet to be solved before this technique can be used to characterize a much bigger area (at least covering a couple of grains). First, the scanning speed must be increased. Second, specialized software that can automatically analyze Laue patterns and plot a 3D microstructure should be developed accordingly, something similar to the OIM software for analyzing EBSD patterns. However, the two area scans discussed above demonstrate the potential of DAXM for characterizing 3D microstructures.
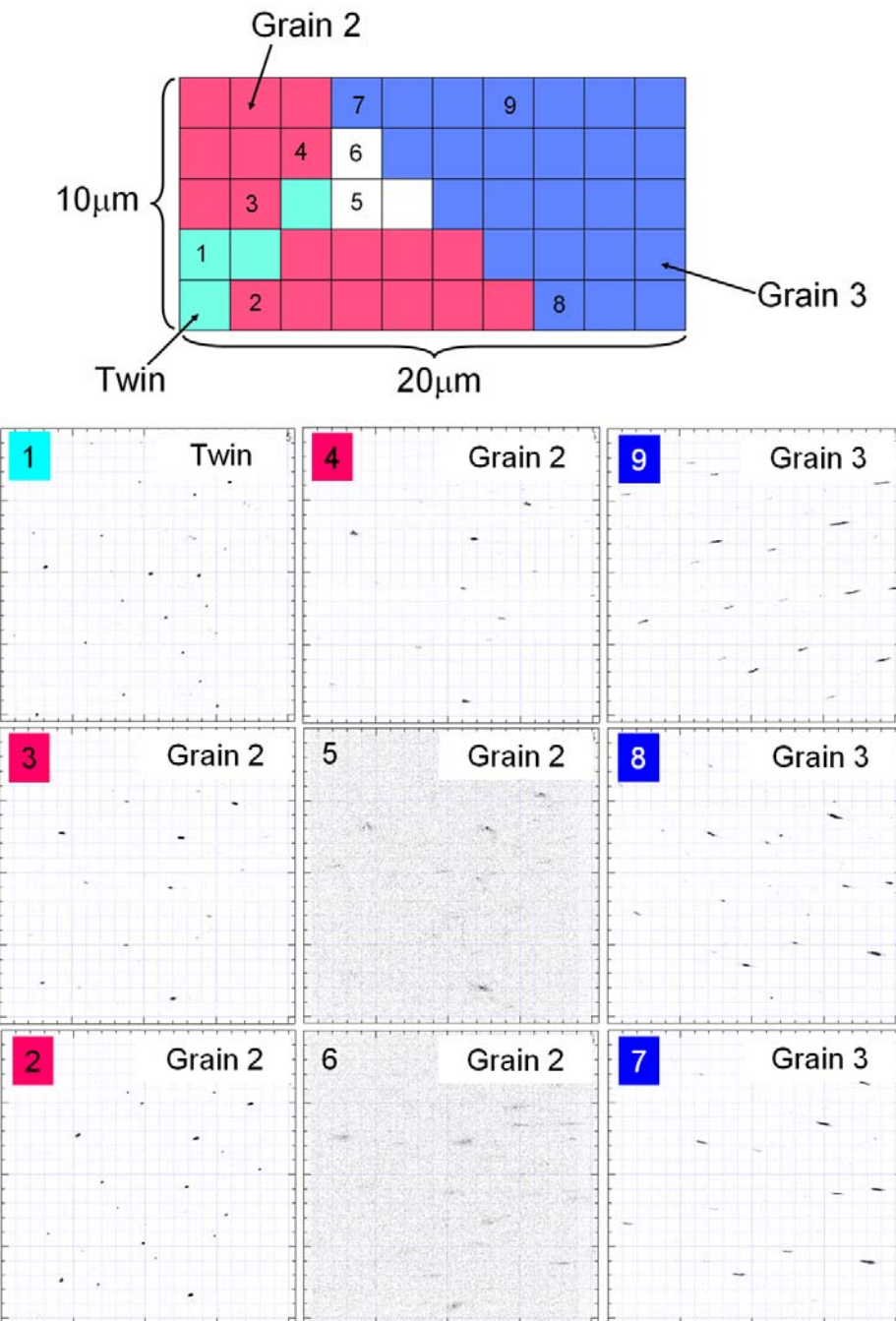
Figure 6.7 A section of the DAXM area scan near the 2-3 grain boundary. The section was about 2 μm beneath the surface. Laue patterns from selected voxels are shown. Patterns 5 and 6 use an intensity threshold that is lower than the rest of the patterns to make the peaks more visible. Laue patterns from grain 3 display significantly streaked peaks, such as patterns 7-9.
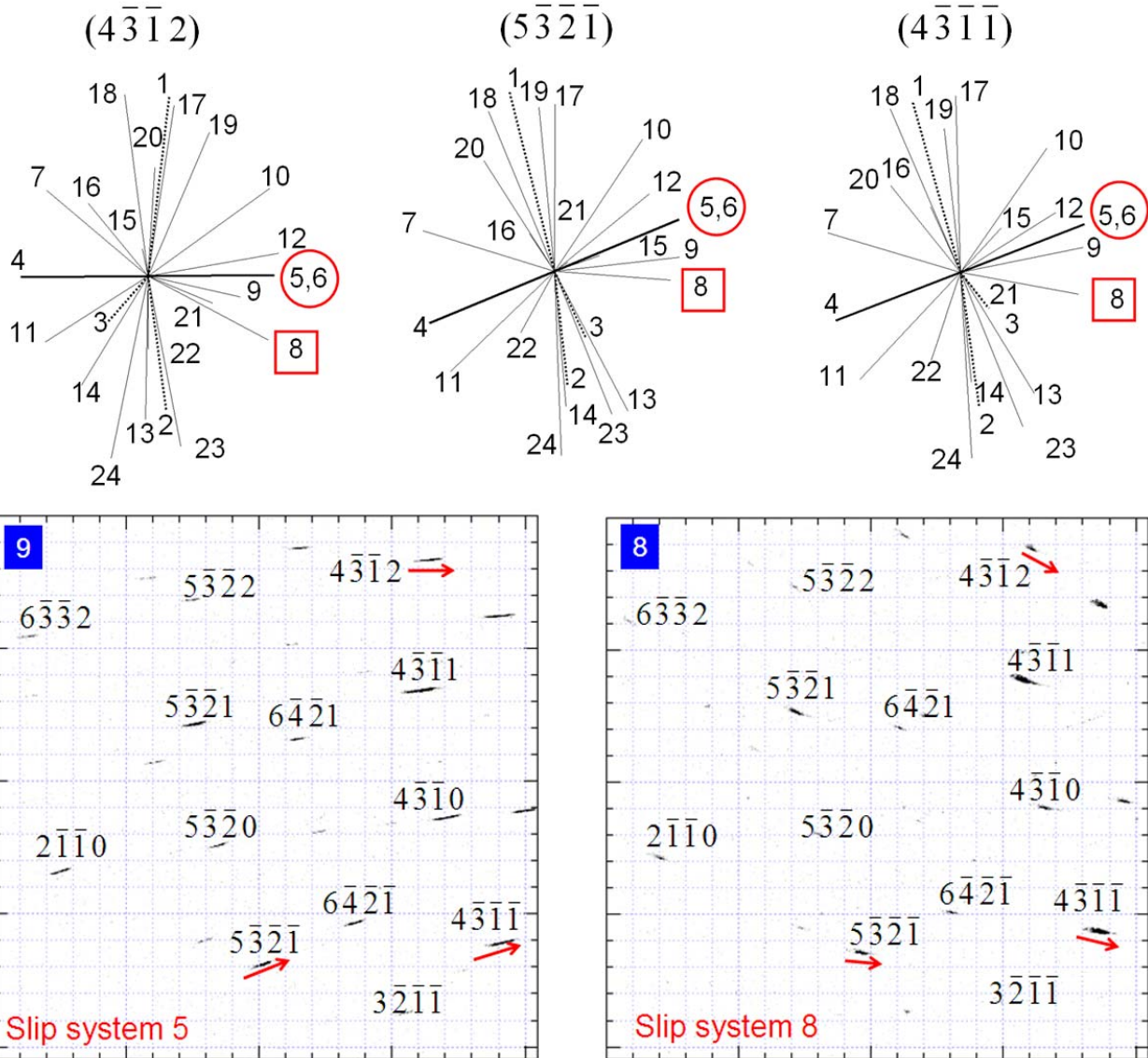
Figure 6.8 Peak streak analysis for identifying GNDs in grain 3. For edge dislocation on each of the 24 slip systems, theoretical peak streak directions for peaks $(4\bar{3}\bar{1}2)$, $(5\bar{3}\bar{2}\bar{1})$, and $(4\bar{3}\bar{1}\bar{1})$ are shown in the three star patterns. Arrows in pattern 9 are the calculated streak direction based on slip system 5, and arrows in pattern 8 are the calculated streak direction based on slip system 8.
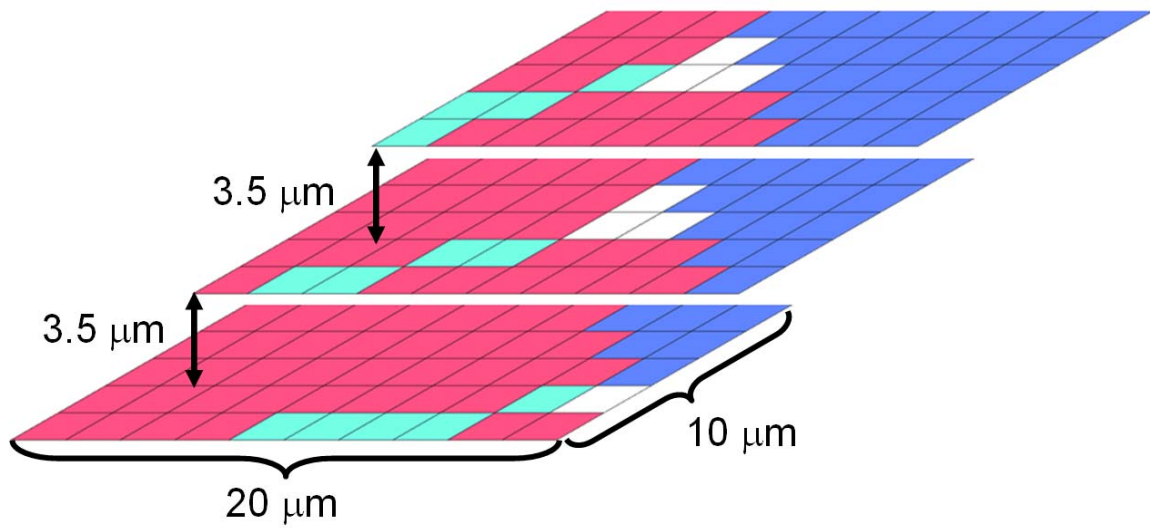
Figure 6.9 Three sections of the area scan are put together to visualize 3-D microstructure. The vertical distance between neighboring sections is 3.5 μm. 2-3 grain boundary (red & blue) is almost perpendicular to the sample surface.

6.3 Summary

DAXM is a non-destructive technique to characterize subsurface microstructure. The primary data of DAXM experiments are depth-resolved Laue patterns of individual voxels from the probed volume. The underlying crystal orientation can be determined from peak positions in a Laue pattern. Streaked peaks are often observed in deformed samples, which indicates the presence of GNDs. The direction of streaked peaks depends on the slip system of the GNDs. Using Nye's dislocation tensor, the theoretical peak streak direction can be calculated for any GNDs. Comparing the computational results for all possible GND slip systems with the actual direction of streaked peaks, the GND slip system can be identified. 3D microstructure can be built from a DAXM area scan, which can show grain boundary inclination beneath the surface.

The DAXM technique can be coupled with CPFE modeling. 3D microstructure measured by DAXM provides an opportunity for more accurate finite element meshing. Lattice rotation (peak shift and streaked peaks) measured by DAXM can be compared with the calculated rotations from CPFEM simulations. This is particularly useful for developing criteria that describe the properties at grain boundaries, an important challenge in CPFE modeling.

Chapter 7

Study of T2 Twinning in α-Ti by EBSD and DAXM

Activity of the $\{11\bar{2}1\} < \bar{1}\bar{1}26 >$ extension twinning (T2) mode was analyzed in a commercial

purity Ti sample after 2% tensile strain from four-point bending. Compared with the many

concurrently formed $\{10\bar{1}2\} < \bar{1}011 >$ extension (T1) twins formed in 6% of the grains, T2 twins

were identified in 0.25% of the grains by scanning electron microscopy (SEM) and electron

backscattered diffraction (EBSD) maps. All of the identified T2 twins nucleated from grain

boundaries, apparently in correlation with extension twins (T1 or T2) formed in the neighboring

grain. Because T2 twins are thin, they have limited capability to accommodate the strain

imposed by deformation of neighboring grains. As a result, other slip or twinning systems are

often activated in the same grain. T2 twin boundaries are often irregular due to the interaction

with adjacent slip bands or T1 twins. In particular, pyramidal <c+a> matrix dislocations

$\{0\bar{1}11\} < \bar{1}2\bar{1}3 >$ with their Burgers vector parallel to the T2 twinning plane $\{\bar{1}\bar{1}21\}$ can transmit

into the twin lattice, then either glide on the two available pyramidal planes in the twin lattice, or

become immobile geometrically necessary dislocations (GNDs) on other planes. Laue

microdiffraction and the associated peak streak analysis were used to analyze the slip system of

GNDs and their distribution inside the twin. The dramatic morphological distinction between T2

and T1 twins was attributed to the different crystallographic nature of their twinning dislocations.

7.1 Identification of T2 twins and Surface Characterization

In the region shown in Figure 5.1 that contains 1980 grains, 116 grains display T1 twins. In this same region, T2 twins were observed in 5 grains in two microstructrual areas. Figure 7.1 shows a low magnification inverse pole figure map, in which grains 1–3 display T2 twins. (The tensile axis inverse pole figure color key is used in all inverse pole figure maps in this chapter.) These T2 twins are shown in greater detail in Figures 7.2 and 7.3 where they are marked by yellow arrows. In grain 1 (Euler angles= (14°, 103°, 61°)), two different T2 twin variants were

identified (Figure 7.2(a)). One variant, $(\bar{1}2\bar{1}1)[1\bar{2}16]$, was successfully resolved in high resolution EBSD scans (step size = 0.15 μm) with a pink color in Figure 7.2(b, c). The

misorientation between the twin and the parent grain was about 35° around the $[10\bar{1}0]$ axis, consistent with the theoretical misorientation relation for T2 twinning in Ti [Christian et al. (1995)]. Along its twin boundaries, small regions of dark pink color (an orientation that is different than the twin and the matrix) were occasionally observed. From an enlarged EBSD

map and the corresponding (0001) and $\{10\bar{1}0\}$ pole figures in Figure 7.2(c), the orientation in the dark pink region (Euler angles= (213°, 77°, 233°)) is almost centered between the twin orientation (Euler angles= (229°, 79°, 231°)) and the matrix orientation (Euler angles= (14°, 103°, 61°)). The misorientation between the dark pink region and the twin was about 16° around

the $[10\bar{1}0]$ axis. Because the matrix, the twin, and the dark pink region had the same $[10\bar{1}0]$

crystal direction, their $(10\bar{1}0)$ poles (the middle one) coincide in the $\{10\bar{1}0\}$ pole figure, while

their $(1\bar{1}00)$ and $(01\bar{1}0)$ poles are distinct. Reed-Hill et al. (1968) observed regions with

similar strong lattice rotation at the tip of some T2 twins in Zr. They suggested, based on the lattice rotation direction, that they are kinks from basal slip $(0001)[1\bar{2}10]$. The poorly indexed band near the bottom of grain 1, according to trace analysis, is parallel to the prismatic plane $(10\bar{1}0)$. If Reed-Hill's ideas are applicable, then one possibility is that $[1\bar{2}10]$ dislocations in the kink band (dark pink region) cross-slipped from plane (0001) to plane $(10\bar{1}0)$. $(10\bar{1}0)$ is the plane of shear for the $(\bar{1}2\bar{1}1)[1\bar{2}16]$ T2 twin, which might be the reason for the cross slip to occur. Further analysis is needed before the cause of this highly defective band can be understood. The other identified T2 variant in grain 1 was $(11\bar{2}1)[\bar{1}\bar{1}26]$. It appears black (pixels of low confidence index) in Figure 7.2(b, c), but it can still be identified by trace analysis.

Many accommodating T1 twins nucleated from its TB. This $(11\bar{2}1)[\bar{1}\bar{1}26]$ twin probably nucleated from its upper end, as it tapers towards its lower end. At its upper end, a T1 twin formed in the opposite grain and a microcrack was observed by a high resolution secondary electron image (inset red box). The T2 twins in grain 2 (also unindexed and identified by trace analysis) connected with the $(\bar{1}2\bar{1}1)[1\bar{2}16]$ twins in grain 1, which is also in connection with T1 twins at its upper end (see Figure 7.2(b)). A generalized T+T mechanism (i.e. T1+T2 or T2+T2) seems to be responsible for the nucleation of the T2 twins in grains 1 and 2. In fact, this generalized T+T mechanism applies for all observed T2 twins in this sample, as will be seen later.
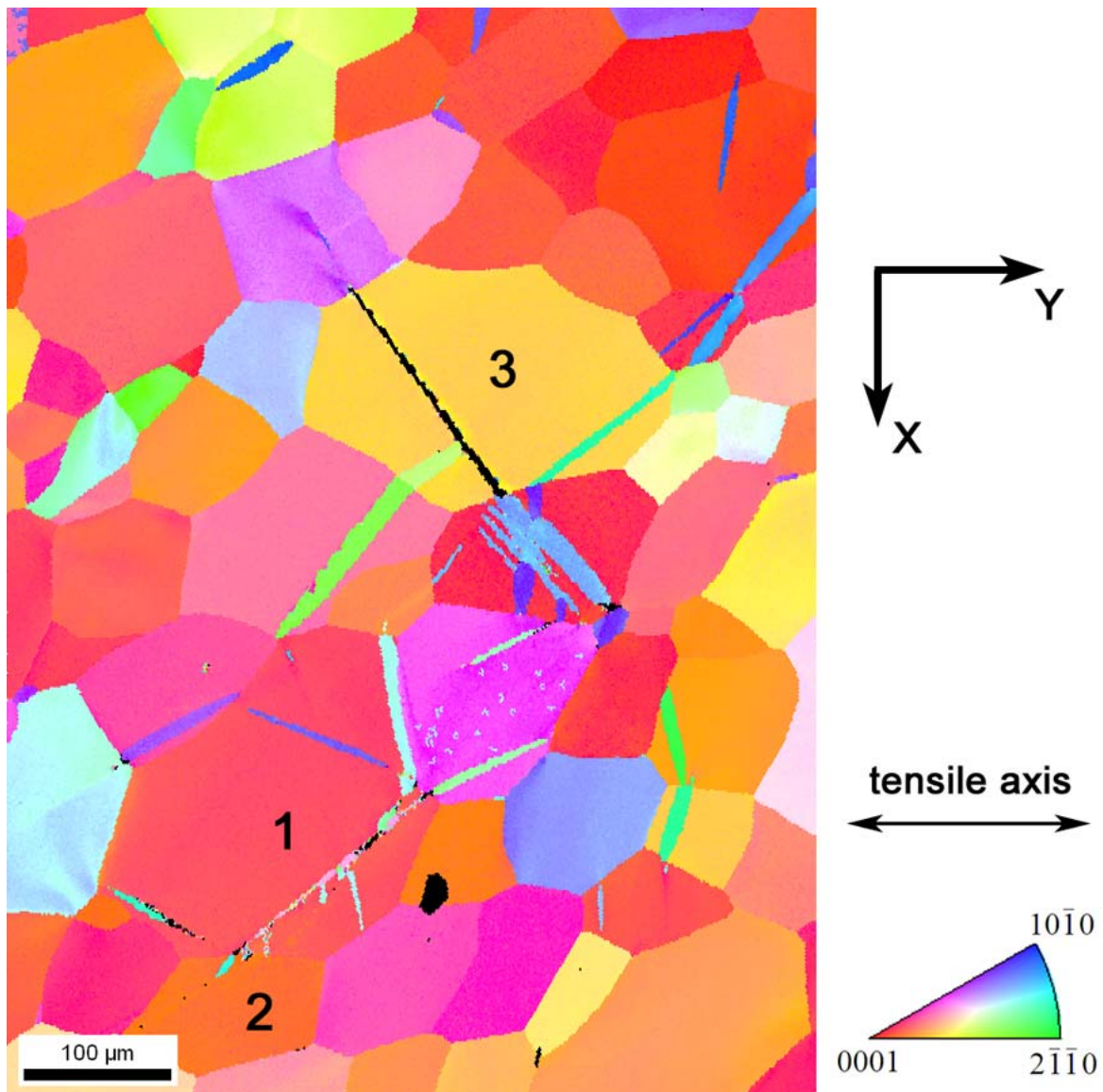
Figure 7.1 Inverse pole figure map of an area containing both T1 and T2 twins. In grains 1, 2, and 3, T2 twins were identified, which are thinner than the more commonly observed T1 twins. The coordinate system right to the map is the basis for Bunge Euler angles.
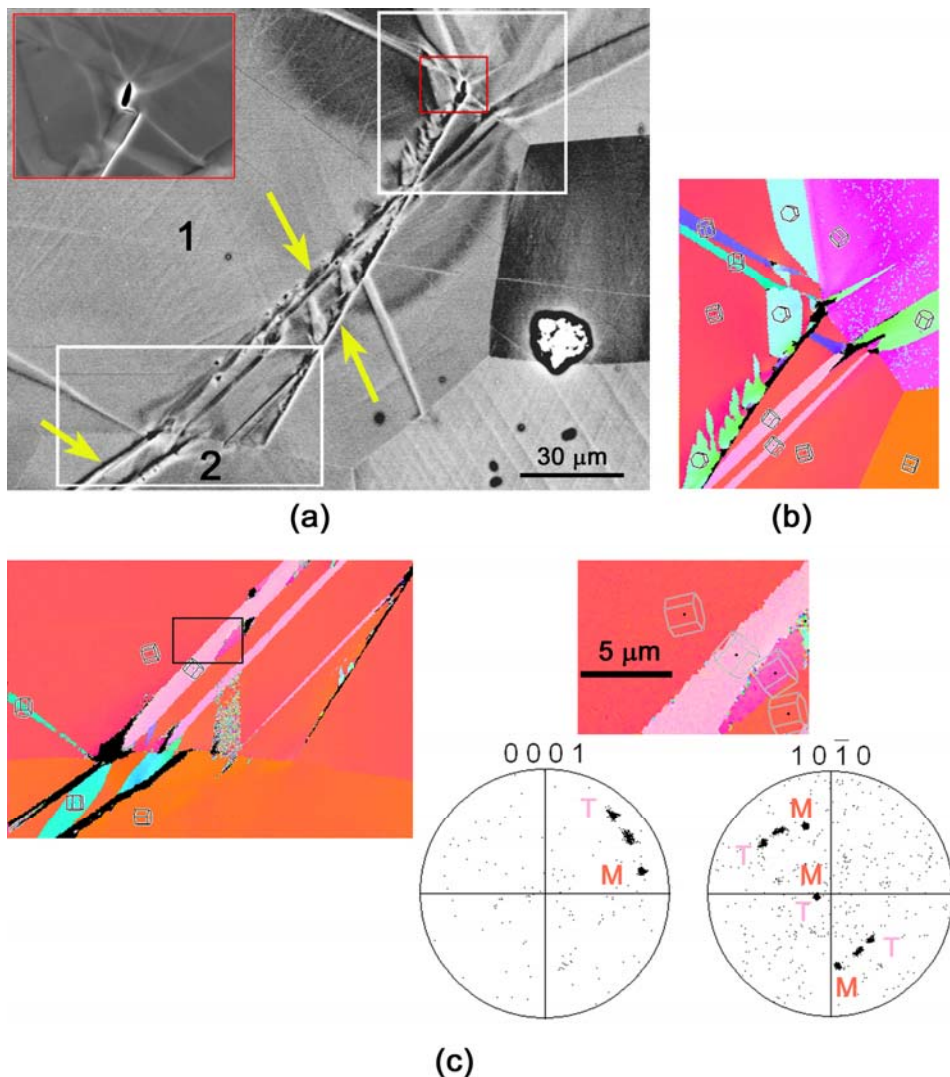
Figure 7.2 (a) Yellow arrows point to T2 twins in grains 1 and 2. At the upper end of one T2 twin variant in grain 1, a microcrack formed. An enlarged image for this microcrack (the area within the red box) is shown in the upper left corner. (b) An EBSD map corresponding to the upper-right white box. (c) EBSD maps corresponding to the lower-left white box. Small regions with intermediate orientation (dark pink color) were found on the twin boundary of a T2 twin, as shown in the enlarged EBSD map. (0001) and $\{10\bar{1}0\}$ pole figures show that the orientation of the dark pink region is almost halfway between the twin orientation ("T") and the matrix orientation ("M").

129

Figure 7.3(a) shows the T2 twin in grain 3 (Euler angles = (157°, 78°, 28°)).   This twin

(twinning system $(1\bar{2}11)[\bar{1}2\bar{1}6]$) has a rough surface morphology, and it blocked the growth of

a T1 twin variant from the left. Given its tapered upper end, this T2 twin is more likely to have

nucleated from its lower end, where many T1 twins nucleated and developed in the adjoining

grain (more evident in Figure 7.1). This is a typical example of "T1+T2". Also, T1 twins

formed in two locations in grain 3 by the "T1+T1" mechanism. In addition to twins, distinct slip

bands were also observed in grain 3. By trace and Schmid factor analysis, these slip bands were

from the activation of $(0\bar{1}11)[11\bar{2}3]$, a pyramidal <c+a> slip system. The slip plane trace of this

slip system matches the slip band trace and its Schmid factor is high, 0.494 (the other <c+a> slip

and the <a> slip on this pyramidal plane has lower Schmid factor of 0.394 and 0.189,

respectively.). Its Burgers vector, $\frac{1}{3}[11\bar{2}3]$, is parallel to the operating T2 twinning plane

$(1\bar{2}11)$, as shown in Figure 7.3(b).
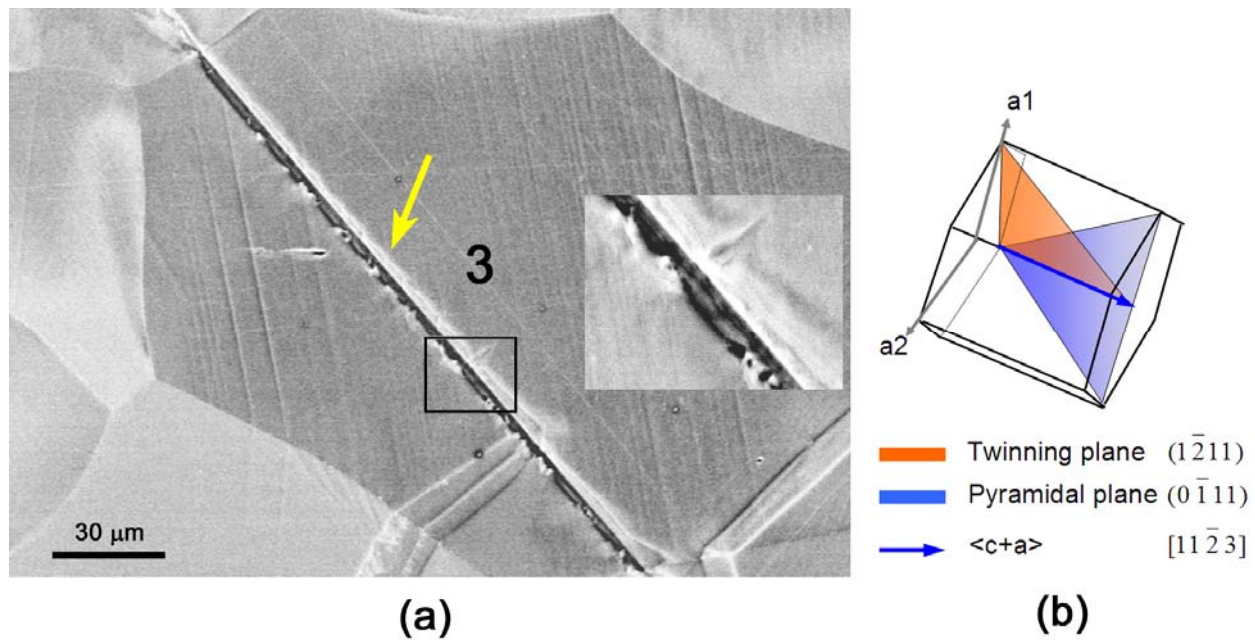
Figure 7.3 (a) Both a T2 twin (yellow arrow) and T1 twins are identified in grain 3. They formed by "T2+T1" and "T1+T1" mechanisms. Part of the T2 twin (the black box) is shown at higher magnification. Grain 3 also display slip lines. (b) The unit cell of grain 3 (Euler angles=(157°, 78°, 28°)). The activated pyramidal <c+a> slip system, $(0\bar{1}11)[11\bar{2}3]$, has its Burgers vector parallel to the operating T2 twinning plane, $(1\bar{2}11)$.

Two other grains display T2 twins (yellow arrows) as shown in Figure 7.4(a). The activated

twinning system in grain 4 (Euler angles $(\varphi_1, \Phi, \varphi_2) = (175°, 66°, 2°))$ was $(\bar{1}\bar{1}21)[11\bar{2}6]$, and

the T2 twin has Euler angles $(\varphi_1, \Phi, \varphi_2) = (22°, 143°, 75°)$. This twin appears to have

stimulated two smaller T2 twins in grain 5 and massive T1 twins in the grain above (see the inset

EBSD map in Figure 7.4(a)). The left TB of this twin is irregular, while the right TB is straight,

but a surface ledge developed there, which gave rise to the very bright local contrast in Figure

7.4(a). This twin separated grain 4 into two parts, with the left part having much stronger slip

lines (indicated by a blue line) than the right part. According to trace and Schmid factor analysis,

two coplanar pyramidal <c+a> slip systems could be activated: $(0\bar{1}11)[\bar{1}2\bar{1}3]$ (Schmid factor =

0.447) or $(0\bar{1}11)[11\bar{2}3]$ (Schmid factors = 0.477). DAXM peak streak analysis later indicated

that $(0\bar{1}11)[\bar{1}2\bar{1}3]$ was the primary active slip system in grain 4. The topographic features in

this area are better shown in Figure 7.4(b), an image taken from a tilted perspective. The region

within the white box in Figure 7.4(b) was imaged at higher magnification under both secondary

electron (SE) mode and backscattered electron (BSE) mode (Figure 7.4(c)). The height of the

ledge is about 1μm. Slip traces of $(0\bar{1}11)[\bar{1}2\bar{1}3]$ were found on the ledge as well as on the

surface. From the BSE image, paired slip lines that nucleated from the ledge can be recognized.

By trace analysis, they correspond to slip on two pyramidal planes, $(0\bar{1}11)_T$ and $(\bar{1}10\bar{1})_T$

(subscript "T" means that the crystal plane/direction is defined in the twin lattice). According to

Christian and Mahajan (1995), a matrix dislocation can transmit into the twin lattice without

leaving a step on the interface if its Burgers vector is parallel to the twinning plane. Recent

molecular dynamics simulations also support this process [Jin et al. (2008)]. Since the activated matrix slip system $(0\bar{1}11)[\bar{1}2\bar{1}3]$ has its Burgers vector parallel to the twinning plane $(1\bar{2}11)$ as well as pyramidal planes $(0\bar{1}11)_T$ and $(\bar{1}10\bar{1})_T$, a very likely possibility is that the observed slip lines in the twin were the result of slip transmission. Figure 7.4(d) shows the geometrical relationship of slip systems $(0\bar{1}11)[\bar{1}2\bar{1}3]$, $(0\bar{1}11)_T[1\bar{2}1\bar{3}]_T$ and $(\bar{1}10\bar{1})_T[1\bar{2}1\bar{3}]_T$ with respect to the twin boundary (TB). From the sense of shear, the co-operation of $(0\bar{1}11)_T[1\bar{2}1\bar{3}]_T$ and $(\bar{1}10\bar{1})_T[1\bar{2}1\bar{3}]_T$ would sink the material between each pair of slip lines and elevate the adjacent material. This topographic feature has been confirmed in another tilted SEM image, and it may explain why the wedge-like regions bounded by paired slip lines have darker BSE contrast in Figure 7.4(c). On the other hand, slip transmission across the twin boundary might not be very easy due to unfavorable geometric factors. First, $(0\bar{1}11)$ is at a large angle with both $(0\bar{1}11)_T$ ($\sim 60°$) and $(\bar{1}10\bar{1})_T$ ($\sim 75°$). In addition, $(0\bar{1}11)_T[1\bar{2}1\bar{3}]_T$ and $(\bar{1}10\bar{1})_T[1\bar{2}1\bar{3}]_T$ had relatively small Schmid factors, 0.123 and 0.278. For the $(0\bar{1}11)[\bar{1}2\bar{1}3]$ dislocations that failed to transmit through the TB, they most likely escaped from the TB to the free surface and formed the ledge concurrently. Note that their Burgers vector had a large out-of-plane component of the unit vector (~0.76).
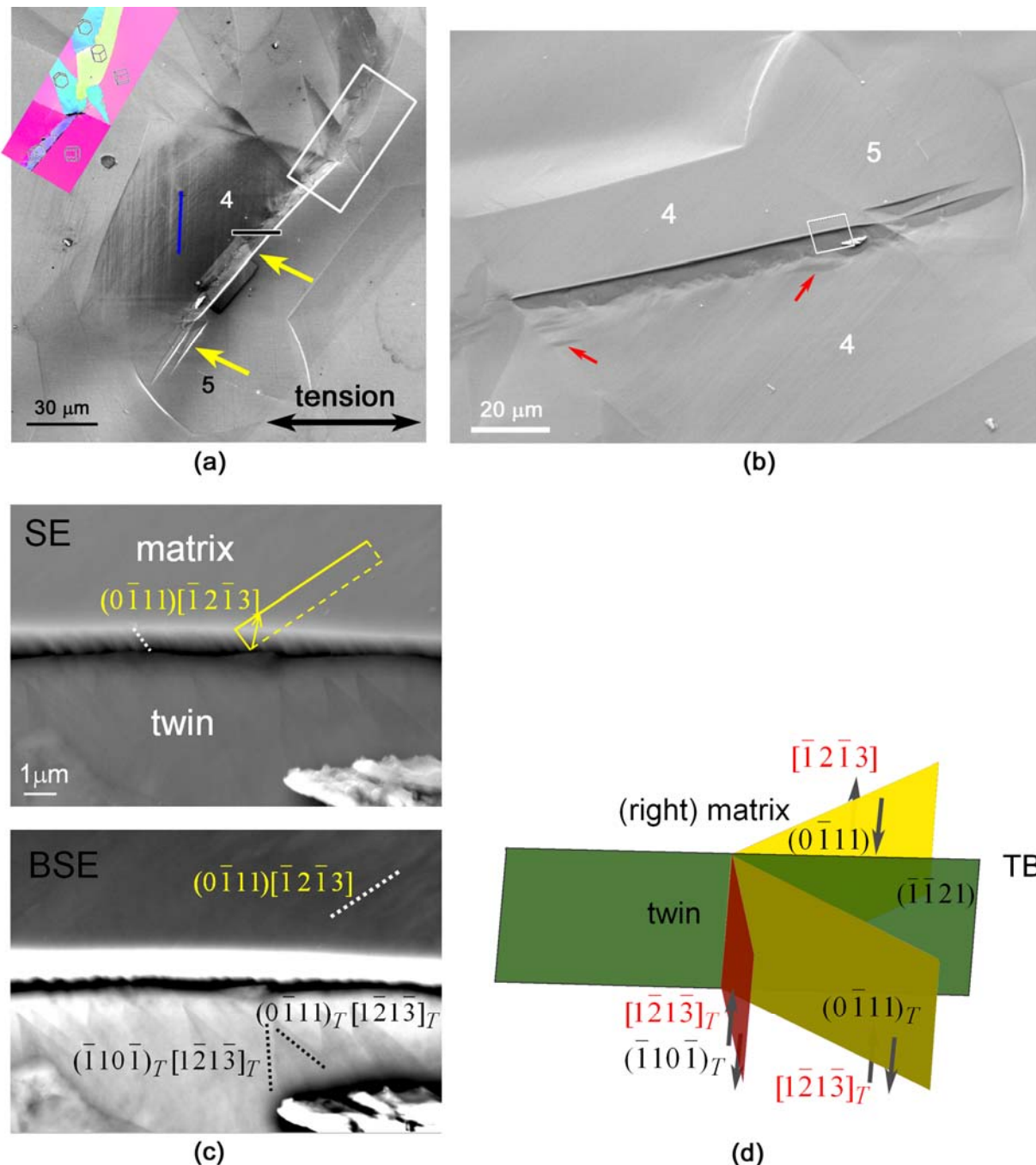
Figure 7.4 (a) T2 twins observed in grains 4 and 5 are indicated by yellow arrows. The EBSD map on the upper-left corner corresponds to the white box. In grain 4, slip lines can be observed left to the T2 twin. The horizontal black line crossing the middle of the twin indicates the location of the DAXM line scan shown in Figure 7.6. (b) An image taken from a rotated and

tilted perspective. Some small T1 twins in grain 4 are marked by red arrows. (c) Secondary

electron (SE) image and backscattered electron (BSE) image for the region within the white box

in (b). $(0\bar{1}11)[\bar{1}2\bar{1}3]$ slip traces can be observed both on the ledge and on the surface. Slip

traces in the twin are identified to be $(0\bar{1}11)_T[1\bar{2}1\bar{3}]_T$ and $(\bar{1}10\bar{1})_T[1\bar{2}1\bar{3}]_T$. (d) Geometrical

relationship of the activated slip systems: $(0\bar{1}11)[\bar{1}2\bar{1}3]$, $(0\bar{1}11)_T[1\bar{2}1\bar{3}]_T$ and $(\bar{1}10\bar{1})_T[1\bar{2}1\bar{3}]_T$.

They have a common Burgers vector that is parallel to the twinning plane.

To further characterize the T2 twin in grain 4, an EBSD scan with step size of 0.02μm (Figure 7.5) was performed with the trace of the twin boundary aligned with the beam scanning direction. Such a setup improved the fraction of high confidence pixel indexing. This scan covered twin and matrix, and it left some visible beam damage on the surface (see Figure 7.4(a)) that reflected the tilted surface topography in the twin; note that the scanned area consists of two narrow rectangular areas, with a shaded parallelogram between them. From the inverse pole figure map in Figure 7.5(a), large orientation gradients are evident in the twin. The orientation spread within the twin is nearly 15° and appears quite heterogeneous (Figure 7.5(b)). Figure 7.5(c) shows the stereographic projection of $\{10\bar{1}0\}$ poles of points A−E. Points A−C were from different places in the twin. Their $(10\bar{1}0)$ and $(01\bar{1}0)$ poles are separated from each other, while their $(1\bar{1}00)$ poles almost converge to a single point, which suggests that the lattice rotation in this twin was roughly around the $[1\bar{1}00]$ axis. Point E was from the matrix. The misorientation between E and A was about 35° around the same $[1\bar{1}00]$ axis (note their $(1\bar{1}00)$ poles almost overlap with each other), very close to the theoretical matrix/twin relationship for this twinning system $(\bar{1}\bar{1}21)[11\bar{2}6]$. Point D is in an orange colored region whose orientation is distinct from the matrix and the twin. Similar to the observation in grain 1 (Figure 7.2(c), this orange region may also be a kink band. However, it cannot be described by a single set of basal dislocations because the $(1\bar{1}00)$ pole of D does not exactly coincide with the matrix nor the twin. Some more complicated dislocation-twin interaction must have occurred in this vicinity.
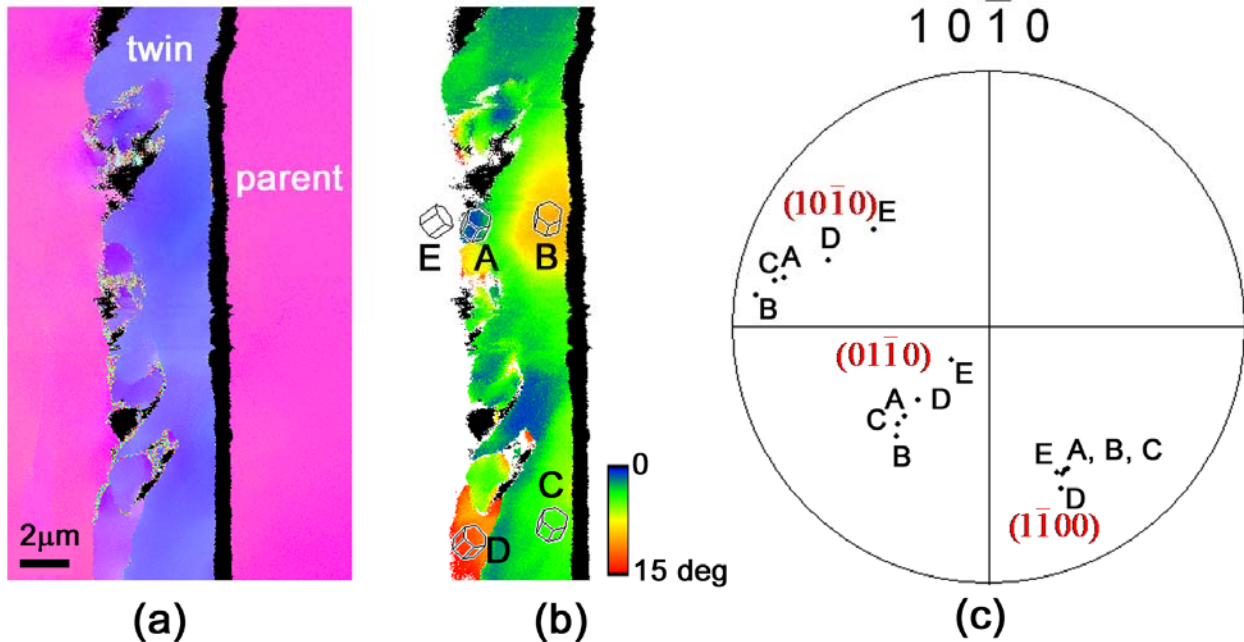
Figure 7.5 (a) High resolution EBSD scan shows large orientation gradients within the twin, while the matrix maintained a more nearly uniform orientation. (b) A map of orientation spread in the twin. Orientations at five points (A−E) are represented by hexagonal unit cells. (c) Stereographic projection of {10$\bar{1}$0} poles of points A−E. A−C from the twin have similarly oriented (1$\bar{1}$00) poles but quite divergent (10$\bar{1}$0) and (01$\bar{1}$0) poles. The misorientation between E and A was about 35° around the same [1$\bar{1}$00] axis. The orientation at point D is different than both the matrix and the twin, making it a distinct "transition region" sitting on the left TB.

137

7.2 DAXM Characterization

A DAXM line scan (length = 20μm, step size=1μm) was performed crossing the middle of the T2 twin in grain 4. The position of this line scan is indicated in Figure 7.4(a). After the experiment, the subsurface structure of this twin was obtained in Figure 7.6. In this figure, pixels with different colors have different crystal orientations. Three orientations were identified from this scan — grain 4 (pink), the embedded T2 twin (light purple), and a subsurface grain (light green). Some pixels were unindexed (white) because diffraction peaks in their Laue patterns are very indistinct — an example Laue pattern from an unindexed pixel was shown in the figure (though it could not be indexed automatically, this indistinct pattern is clearly from the twin, by comparing it with diffraction patterns in Figure 7.7). From Figure 7.6, the inclination angle between the T2 twin and the sample surface was about 40°, close to the calculated value (~38°). Near the surface, the thickness of the twin along the tensile direction (horizontal) was about 7~8 μm; Further from the surface, the twin was not quite as thick. The surface topography revealed by DAXM is consistent with the SEM observation in that the surface to the right of the twin was slightly higher than the surface left to the twin.
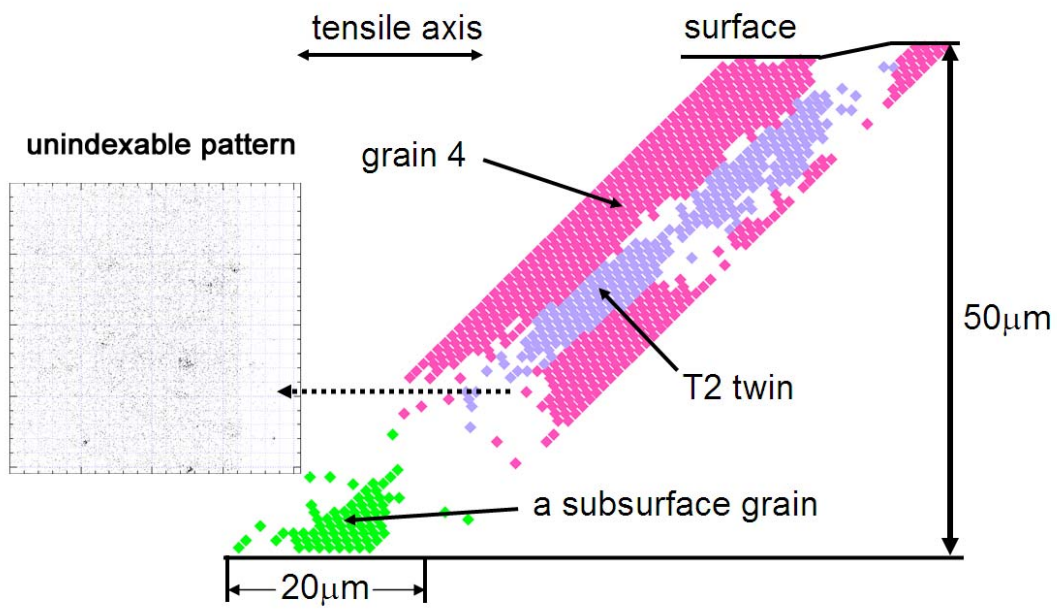
Figure 7.6 A DAXM line scan reveals the subsurface structure of the T2 twin in grain 4. A grain underneath was also identified. Laue patterns in the white regions cannot be indexed automatically.

Every Laue pattern from this scan was examined by eye. In Figure 7.7, pixels are colored based on the appearance of their Laue patterns. In the matrix, the yellow region and the red region display streaked peaks but along different directions. Two typical Laue patterns (*a* and *b*) from these two regions are shown in Figure 7.7. It can be inferred that the yellow region and the red region in the matrix contain different types of GNDs. In the twin, streaked peaks were also observed in the dark green region and the light green region along different directions (patterns *d* and *f*). The light grey regions show no apparent peak broadening (e.g. pattern *c* and pattern *g*), thus containing minimal GND content. The dark grey regions display complex shaped Laue peaks with strong curvature instead of straight streaks (e.g. pattern *e*).

Peak streak analysis was performed to identify the GNDs in the yellow, red, dark green, and light green regions where straight streaked peaks were present. Initially, only the 24 regular slip systems for Ti were tested (edge and screw types). The analysis shows that the yellow region in the matrix contained $(0\bar{1}11)[\bar{1}2\bar{1}3]$ edge GNDs (same slip system as the surface slip bands, Schmid factor=0.447), and the red region contained $(1\bar{1}01)[\bar{1}2\bar{1}3]$ edge GNDs (Schmid factor=0.377). None of the 24 regular slip systems could account for the peak streak in the twin, so more slip systems were tested. It was found that the dark green region contained $(\bar{1}\bar{1}21)_T[1\bar{2}1\bar{3}]_T$ edge GNDs (Schmid factor = 0.330), and the light green region contained $(\bar{1}010)_T[1\bar{2}1\bar{3}]_T$ edge GNDs (Schmid factor = 0.457). Simulated patterns by Barabash based on these GNDs match the patterns *a*, *b*, *d*, and *f* very closely, as shown in Figure 7.8. The 4 activated slip systems are visualized in the matrix unit cell (Euler angles = (175°, 66°, 2°)) and

the twin unit cell (Euler angles = (22°, 143°, 75°)). $(\bar{1}\bar{1}21)_T[1\bar{2}1\bar{3}]_T$ dislocations have been

previously observed by Vaidya and Mahajan using TEM in the vicinity of T2 twins in Co

[Vaidya et al. (1980)].
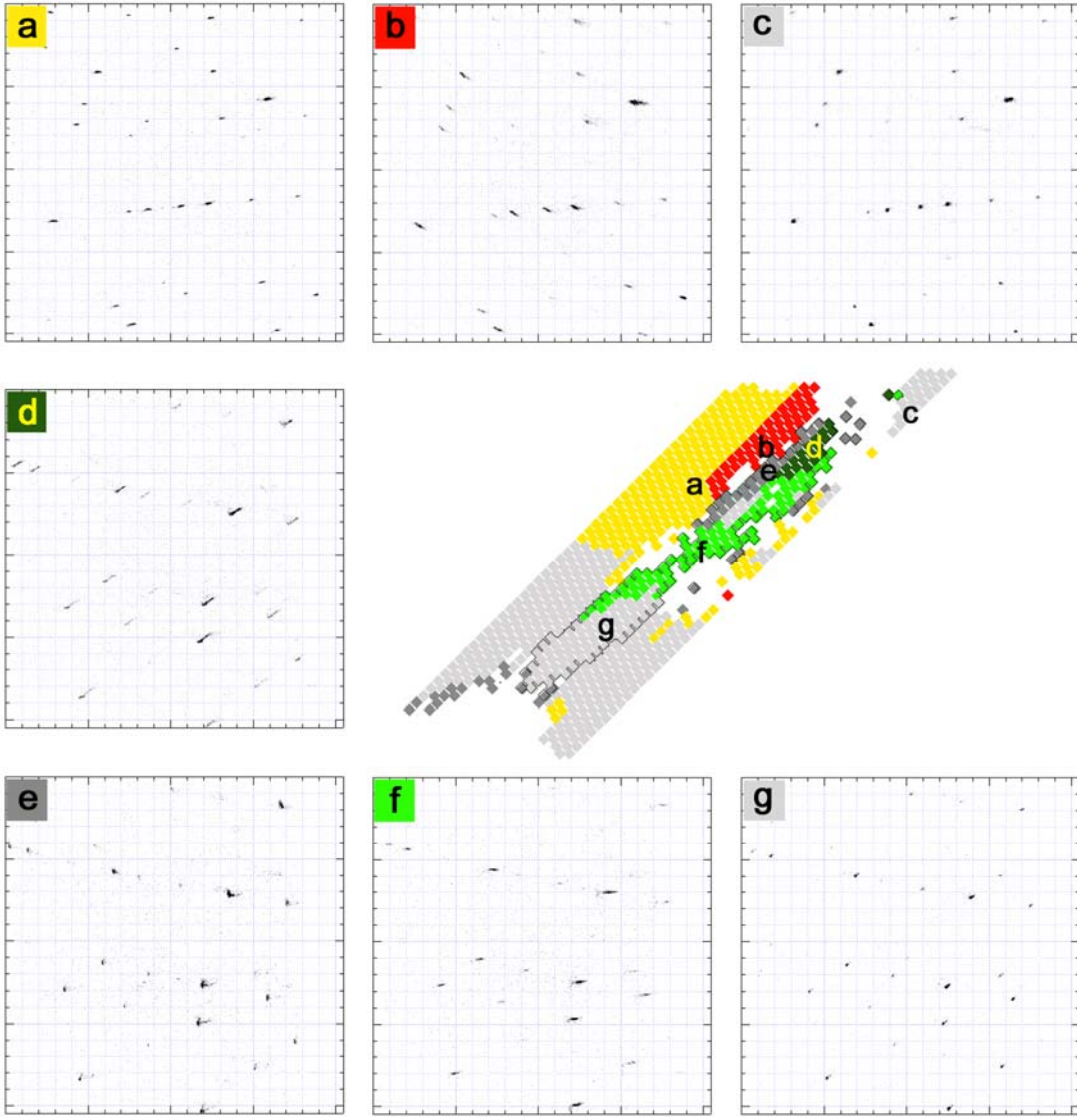
Figure 7.7 Sub-division of grain 4 (matrix) and the T2 twin based on the appearance of Laue patterns. The twin is between the black boundaries. Laue patterns at selected pixels (*a–g*) are shown. In the matrix, the yellow region and the red region display streaked peaks (e.g. pattern *a* and pattern *b*). In the twin, the dark green region and the light green region also displayed streaked peaks (e.g. pattern *d* and pattern *f*). GNDs in these colored regions will be analyzed in Figure 7.8. The light grey regions show no apparent peak broadening (e.g. pattern *c* from the matrix and pattern *g* from the twin). The dark grey regions have complex shaped diffraction peaks (e.g. pattern *e*).
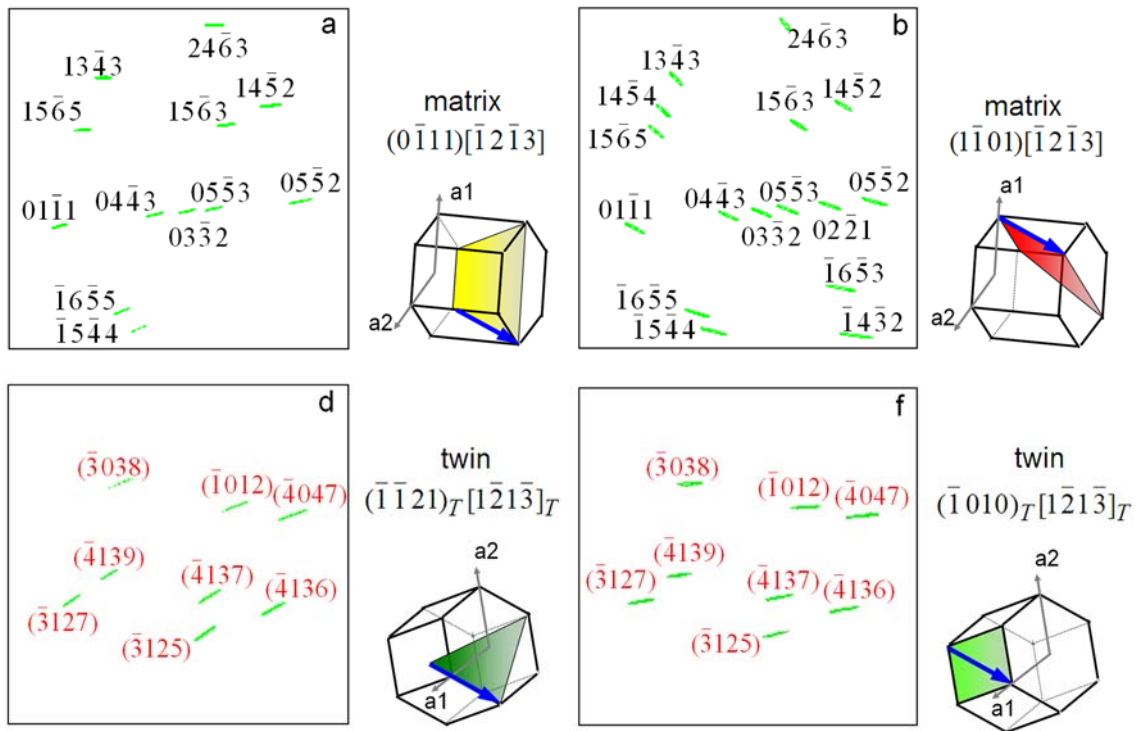
Figure 7.8 Slip systems of GNDs in the yellow, red, dark green and light green regions in Figure 7.7 are identified: they are $(0\bar{1}11)[\bar{1}2\bar{1}3]$, $(1\bar{1}01)[\bar{1}2\bar{1}3]$, $(\bar{1}\bar{1}21)_T[1\bar{2}13]_T$ and $(\bar{1}010)_T[1\bar{2}13]_T$, respectively.   The simulated Laue patterns based on edge GNDs on these 4 slip systems match the experimental patterns (*a, b, d* and *f*) in Figure 7.7. Peak indices are black for the matrix lattice and red for the twin lattice. The Burgers vector and the slip plane of these identified slip systems are visualized in the unit cells for the matrix and the twin.

Combining the results from surface slip trace and peak streak analysis, all of the identified

dislocations in grain 4 and the T2 twin had the same <c+a> Burgers vector — $\frac{1}{3}[\bar{1}2\bar{1}3]$. These

dislocations glided on six different planes. Figure 7.9(a) summarizes the identified dislocation

activity around the twin.

Near the left TB, <c+a> edge GNDs were identified on four slip planes $(0\bar{1}11)$, $(1\bar{1}01)$, $(\bar{1}\bar{1}21)$

(equivalent to $(\bar{1}\bar{1}21)_T$ because it is the twinning plane), and $(\bar{1}010)_T$. The misalignment

between $(0\bar{1}11)$ and $(\bar{1}010)_T$ is only about 5.3°, so the uncommon prismatic <c+a>

dislocations of $(\bar{1}010)_T[1\bar{2}13]_T$ in the light green region, which were present across the entire

twin, are likely to be the result of transmutation of the primary matrix dislocations $(0\bar{1}11)[\bar{1}2\bar{1}3]$

in the twin lattice during twin growth. Based on crystallographic analysis, a recent paper

[Niewczas (2010)] also suggested the possibility of this dislocation transmutation for T2

twinning in Zr, a hexagonal metal with its c/a ratio very close to Ti. The identified

$(1\bar{1}01)[\bar{1}2\bar{1}3]$ and $(\bar{1}\bar{1}21)_T[1\bar{2}13]_T$ edge GNDs can be understood as the outcome of cross-slip,

as illustrated in Figure 7.9(b): when a $(0\bar{1}11)[\bar{1}2\bar{1}3]$ dislocation loop encountered the twin

boundary, its screw segment could cross slip from $(0\bar{1}11)$ onto the neighboring pyramidal plane

$(1\bar{1}01)$ or onto the twinning plane $(\bar{1}\bar{1}21)$. The screw segment could continue to glide on these

two planes, while the edge segments were less mobile, since their movement would be pinned by

the jog out of the $(0\bar{1}11)$ plane. Due to this pinning effect, accumulated edge segments can

account for the observed GNDs. Near the right TB, slip lines of $(0\bar{1}11)[\bar{1}2\bar{1}3]$, $(0\bar{1}11)_T[1\bar{2}1\bar{3}]_T$

and $(\bar{1}10\bar{1})_T[1\bar{2}1\bar{3}]_T$ were identified on the surface (Figure 7.4(c)). As analyzed before,

activation of $(0\bar{1}11)_T[1\bar{2}1\bar{3}]_T$ and $(\bar{1}10\bar{1})_T[1\bar{2}1\bar{3}]_T$ could arise from slip transmission.
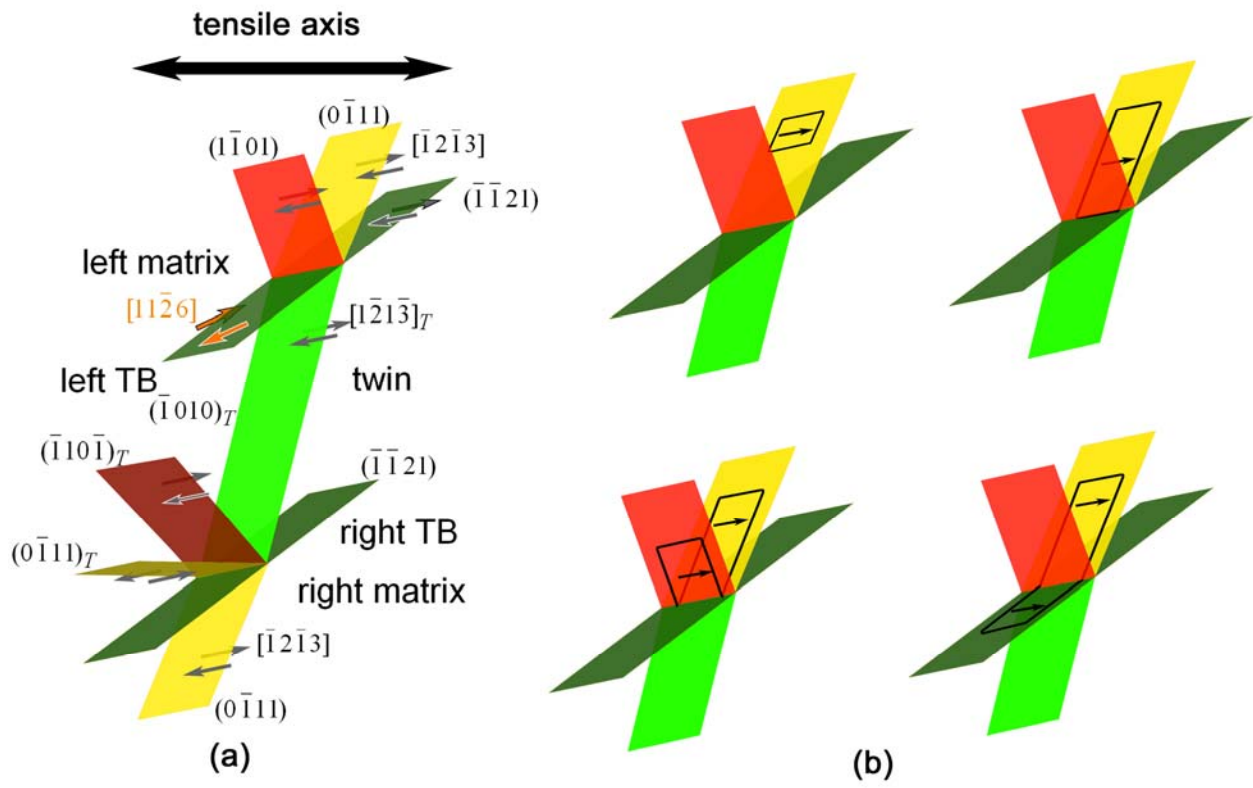
Figure 7.9   (a) Summary of dislocation activities around the twin. All of the identified

dislocations had the same <c+a> Burgers vector: $\frac{1}{3}[\bar{1}\,2\,\bar{1}\,3]$ or $\frac{1}{3}[1\bar{2}1\bar{3}]_T$. This <c+a> Burgers

vector was about 27.5° from the twinning direction $[11\bar{2}6]$. (b) $(1\bar{1}01)[\bar{1}\,2\,\bar{1}\,3]$ and

$(\bar{1}\,\bar{1}\,21)_T[1\bar{2}1\bar{3}]_T$ GNDs were likely the result of cross slip from $(0\bar{1}11)[\bar{1}\,2\,\bar{1}3]$ dislocations.

7.3 Discussion

7.3.1 Dislocation-twin interaction and the resultant morphology

As shown in Figure 7.4, the T2 twin in grain 4 had unique morphology: its left boundary was rough; its right boundary was straight but a surface ledge developed on it; large orientation gradient was found inside the twin. A sequence of events is proposed here that can account for these observations, as summarized in Figure 7.10. Upon initial loading, $(0\bar{1}11)[\bar{1}2\bar{1}3]$ <c+a> slip was activated in the entire grain 4 (Figure 7.10(a)). Sometime later, the T2 twin nucleated and quickly grew through the grain, while preexisting $(0\bar{1}11)[\bar{1}2\bar{1}3]$ dislocations became sessile $(\bar{1}010)_T[1\bar{2}1\bar{3}]_T$ GNDs in the twin, making it hard for any other slip system to operate (Figure 7.10(b)). The sense of shear of the twinning system, indicated by a pair of orange arrows in Figure 7.9(a), is similar to the <c+a> slip system. Operation of this twinning system moved mass to the right of the twinning plane in a positive z direction, leading to the topographic ramp shape as shown in Figure 7.4. With further loading, more $(0\bar{1}11)[\bar{1}2\bar{1}3]$ <c+a> dislocations were generated in grain 4, primarily in the left part while also in the right part (Figure 7.10(c)). (The formation of the twin may have altered the local stress state and reduced the driving force for further <c+a> slip on its right side, or the twin was effective in blocking <c+a> dislocations arriving from sources in the upper left part of the grain.) For these newly generated <c+a> dislocations, various slip transmission events — through cross slip facilitated by the Burgers vector being parallel to the twinning plane — occurred at both twin boundaries. Dislocations built up inside the twin, causing significant orientation rotations. With more dislocations being pushed into the twin, slip transmission became more and more difficult due to the back stresses

from the existing sessile and mobile dislocations in the twin. Eventually the twin became a true

barrier for the matrix <c+a> dislocations (Figure 7.10(d)). On the right TB, subsequent <c+a>

dislocations escaped from the TB to the free surface, forming a ledge there. It could happen

because the sense of shear of slip system $(0\bar{1}11)[\bar{1}2\bar{1}3]$ was to move mass on the right upward,

which would not be constrained by the presence of the twin. Measurements of the ledge

geometry shows that the ledge is not parallel to the twin plane, so the ledge represents a mode II

crack on a plane in the matrix orientation, which has no obvious low index plane. On the left TB,

subsequent <c+a> dislocations could not escape from the TB to the free surface because the left

TB would not allow the mass to its right (twin) to be elevated. As a result, many <c+a>

dislocations were trapped outside the left TB, causing the irregular topography there.
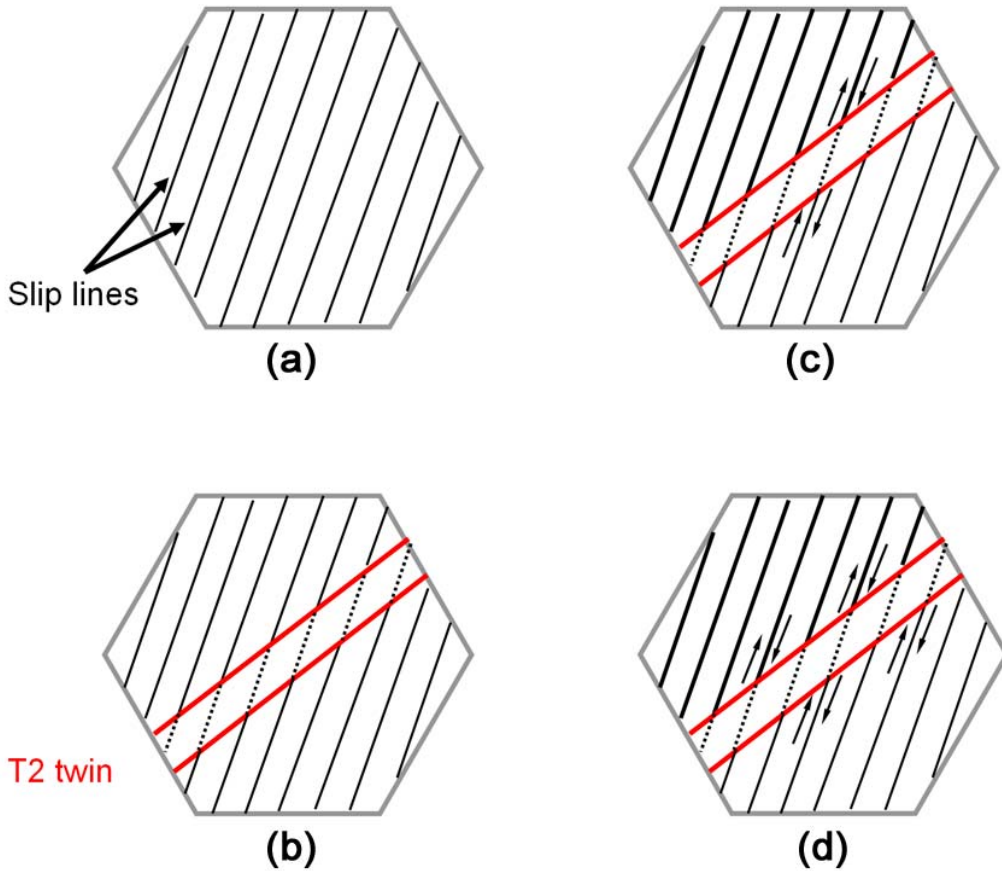
Figure 7.10 Schematic drawing of the possible sequence of events in grain 4. (a) $(0\bar{1}11)[\bar{1}2\bar{1}3]$ was activated in the entire grain. (b) Formation of the T2 twin divided grain 4. Preexisting

<c+a> dislocations transited from plane $(0\bar{1}11)$ (solid line) to the closely oriented plane

$(\bar{1}010)_T$ (dotted line). (c) Subsequent operation of $(0\bar{1}11)[\bar{1}2\bar{1}3]$ led to slip transmission near

the TB. (d) Accumulation of $(0\bar{1}11)[\bar{1}2\bar{1}3]$ dislocations gave rise to the disparate topography of

the left TB and the right TB.

7.3.2 Difference between T1 and T2 twins

T1 and T2 twins are greatly different from each other, in their nucleation, growth, and morphology. These differences can be interpreted by comparing their twinning dislocations.

For hexagonal metals, the Burgers vector of a T1 twinning dislocation is $\mathbf{b_{T1}} = \frac{3 - \gamma^2}{3 + \gamma^2} < \bar{1}011 >$ [Christian et al. (1995)]. Given $\gamma \approx 1.59$ for Ti, its magnitude is $b_{T1} = \frac{3 - \gamma^2}{\sqrt{3 + \gamma^2}} a \approx 0.20a$. A recent atomistic simulation suggested that a stable T1 twin nucleus needs the coordinated participation of six T1 twinning dislocations [Wang J et al. (2009)], i.e. a zonal dislocation. The total shear associated with a stable T1 twin nucleus is thus 1.2**a**, close to the magnitude of an <a> dislocation. As a result, a matrix <a> dislocation could potentially trigger the nucleation of a T1 twin, mostly at grain boundaries. In fact, S+T events described in Chapter 4 are consistent with this mechanism. Similarly, the Burgers vector of a T2 twinning dislocation is

$\mathbf{b_{T2}} = \frac{1}{3(4\gamma^2 + 1)} < 11\bar{2}6 >$. Its magnitude is $b_{T2} = \frac{1}{\sqrt{1 + 4\gamma^2}} a \approx 0.30a$. There has been no atomistic study of T2 twin nucleation so far. Nonetheless, by crystallographic analysis, Vaidya and Mahajan suggested that a stable twin nucleus needs twelve twinning dislocations [Vaidya et al. (1980)], which have the total magnitude of 3.6**a**. This value is two times larger than that for T1 twinning. From a probabilistic point of view, it is much easier to form a T1 twin nucleus than a T2 twin nucleus, which can explain why T2 twins are much rarer than T1 twins. On the other hand, to accommodate the large twinning shear of a T2 twin that nucleates from a grain boundary, coordinated formation of other tensile twins in the neighboring grain can assist in

maintaining coherency of the grain boundary plane. In fact, T2 twins identified in grains 1, 3

and 4 are all correlated with T1 twins at one of their ends, suggesting a mutual nucleation event

(i.e. T1+T2). T2 twins in grains 2 and 5 were likely the result of T2 +T2 strain transfer from

grain 1 and grain 4, respectively. In the case of T1+T2 co-nucleation, after nucleation, the

subsequent growth of a T2 twin may require coordinated growth of the T1 twin in the

neighboring grain. However, this could be difficult. T1 and T2 twins are likely to grow at

different speeds, so that their twin boundaries would soon disconnect on the grain boundary with

an increasing separation distance after the initial twin nucleation. This separation distance makes

strain transfer more difficult because T1 twinning dislocations would need to migrate along the

grain boundary for the separation distance before they join the TB of the T2 twin and reorganize

themselves to become the requisite T2 zonal twinning dislocations for the T2 twin to grow (and

vice versa), as illustrated schematically in Figure 7.11. Such a complex process means that T2

twins that nucleated by a T1+T2 mechanism cannot grow very wide. Consequently, this also

limits the width of T2 twins that were stimulated by other T2 twins.

Due to the limited width of T2 twins, other slip or twinning activity is usually needed for the

parent grain to continue deformation. (T1 twins are found in grains 1–4; slip bands are observed

in grain 3 and grain 4.) T2 twin boundaries are usually irregular because of their interaction with

other slip bands or T1 twins. In contrast, T1 twin can grow to a wide distance and bear most of

the strains for the parent grain. At the low strain level, grains that show T1 twins seldom

develop other slip or twinning systems. Without interaction with dislocations or other twins,

most T1 twin boundaries are smooth. Summarizing, the morphological distinction between T1

and T2 twins can be boiled down to the different length of their twinning dislocations and the number of twinning dislocations that are necessary for a stable twin nucleus.
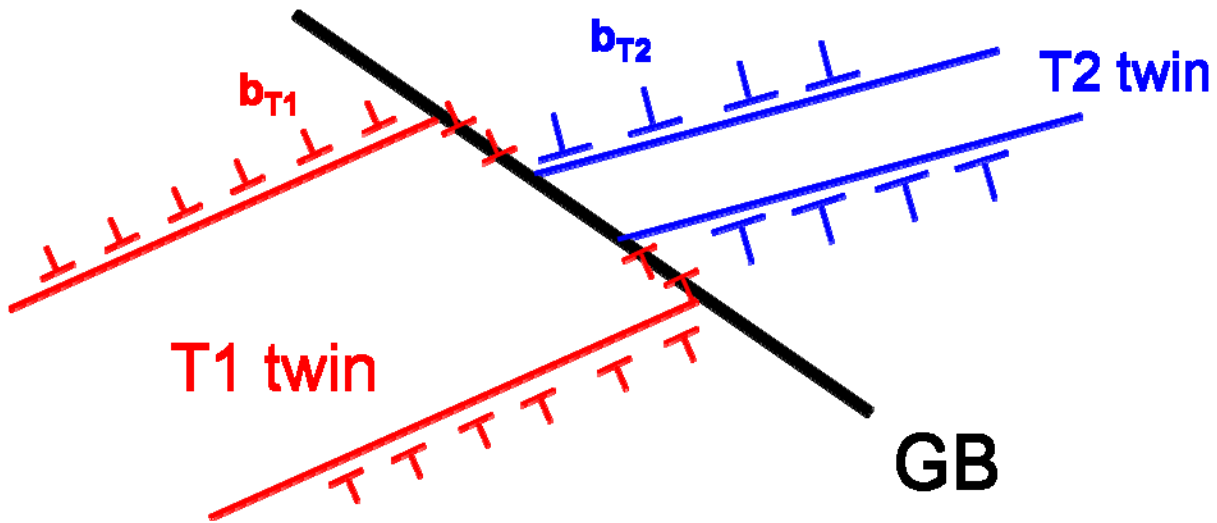
Figure 7.11 In the case of T1+T2, twin boundaries of the T1 twin and the T2 twin soon

separated with each other. Further growth requires twinning dislocations to migrate on the grain

boundary (GB) to complete the strain transfer.

7.4 Summary

Both T2 and T1 twins formed in a Ti sample after a small tensile strain, though the number of T2 twins was much smaller. The width of T2 twins is usually small, making the activation of other slip or twinning systems in the same parent grain necessary. Pyramidal <c+a> dislocations with their Burgers vector parallel to the T2 twinning plane could transmit through twin boundaries via cross slip, then either continue gliding on the two pyramidal planes in the twin lattice or become immobile GNDs, which gave rise to kink bands and large orientation gradients inside some T2 twins. Interaction between slip bands and T2 twin boundaries makes the growing side of the twin boundary irregular. Because a stable T2 twin nucleus needs more twinning dislocations of greater magnitude than T1 twinning, most T2 twins nucleated at a grain boundary by the formation of other T1 or T2 twins in the neighboring grain (T1+T2 & T2+T2). In T1+T2, unsynchronized growth of T1 and T2 twins likely limited the final width of the T2 twin.

Chapter 8

Discussion

Nucleation and propagation of twins in hexagonal metals as a mechanism to accommodate strain along the <c> axis has been observed for many decades. However, many questions about twin nucleation and twin propagation remain unanswered: Why is the Schmid law often not applicable for twin nucleation? What are the driving forces for twin nucleation? Can twin nucleation be predicted in a well-characterized polycrystal?

This work sheds some important light on these questions. From this work, and some recent similar work in Zr [Beyerlein, et al. (2010)], most twins nucleate from grain boundaries. This work has shown that most of the twins nucleate in order to accommodate the strain mismatch on the grain boundary due to strong slip or twinning activities in the adjacent grain. By this strain transfer mechanism, the global stress state and the associated Schmid factor for twinning is no longer the decisive factor for the activation of a twinning system. Instead, the alignment between the twinning system to be activated and the active slip or twinning system in the adjacent grain is more important. This alignment is quantified by a geometric parameter, m', which can be easily calculated if the crystal orientations of the grain pair is known. From statistical analysis, the likelihood for twin nucleation has been correlated with the magnitude of m'. Therefore, prediction of twin nucleation can be substantially improved by calculating the m' at grain boundaries for slip and twinning systems that have reasonably high Schmid factors. This

method would be most effective in a slightly strained ($\varepsilon \approx 1\%$) sample, where some incipient slip lines and twins can be identified under the SEM.

To date, most CPFE models solely use the CRSS-based law to simulate twin nucleation and twin propagation. This framework is easy to implement, but it has at least two obvious flaws. First, as noted above, the Schmid Law can be inaccurate for describing twin nucleation. Second, twin deformation is simulated as a single direction slip system in these models, so the twinning shear usually spreads homogeneously over the entire grain and there are no well-defined twin boundaries inside the matrix grain, which contradicts the fact that twin shear alters the shape and orientation of the volume of the twin, and the twin boundaries create barriers to slip on other systems. As a result, constitutive models that use CRSS-based slip laws to simulate twinning will inevitably be inaccurate in the calculation of the flow stress and the hardening rate. The strain transfer twin nucleation mechanism identified in this work provides a new perspective on how to properly simulate twinning with CPFEM.   Since twins tend to nucleate from grain boundaries, an improved model should keep track of the shear of the elements that are adjacent to grain boundaries. If a significant shear mismatch is observed between two elements on the two sides of a grain boundary, plus if there is a suitable twinning system (high m' and relatively high twinning Schmid factor) in the less strained element, then that twinning system should be activated if the shear mismatch, m', and the twinning Schmid factor together surpass a certain threshold. Subsequent twin propagation can be described with the same framework, as the same twinning system is going to be activated in the elements that are next to the initial twin nucleation element (m' would be 1). With the twinning system being activated in elements one by one, the shear mismatch between "twinned" elements will decrease, reducing the driving

156

force for continuing twinning shear in these elements. This scheme will account for the fact that shear associated with twinning only occurs in the very vicinity of twin boundaries while the twinned area can no longer be strained by the same twinning system. In addition, it is necessary to assign the twin orientation to the elements in which the accumulated shear on a twinning system reaches the theoretical twin shear, so that they can accommodate the subsequent deformation by activating other slip or twinning systems with the new orientation. The above described CPFEM framework belongs to the so-called non-local model, since it explicitly considers the interaction between element neighbors. On the basis of these ideas, such a model is under development as part of a collaborative effort with Philip Eisenlohr at Max-Planck-Institut für Eisenforschung.

Most experimental work on microstructrual deformation focuses on the surface area of the sample. The results from such analysis are always susceptible to effects due to the presence of the free surface, though the real impact of the free surface to the deformation microstructure is yet unclear. The results of DAXM analysis show gradients in deformation behavior with depth from the surface in many cases, but there are also instances where the activated deformation systems are consistent between the surface and subsurface region. Thus, it is not easy to make a generalized assessment about the influence of the surface on activated slip systems. A more robust investigation should use the 3D grain structure and probe the deformation and damage nucleation processes inside the material in a statistically significant number of locations with different grain boundary geometry, and grain misorientations. DAXM provides such a possibility, as demonstrated in Chapter 6. This technique allows 3D grain structure to be measured in a non-destructive manner. After deformation, lattice rotation and the related GNDs

is characterized by peak streak analysis. With increased scanning speed and the use of some in-situ deformation apparatus, perhaps one day the entire deformation process in a bulk microstructure can be characterized, and the results can be readily compared with the computational results from a CPFE model that uses the real grain structure and some advanced constitutive laws. That would be an important milestone achievement in physical metallurgy.

Hexagonal metals have more than one available twinning mode. Although T1 twinning is the most common and most studied mode, the general picture of twinning will be incomplete without bringing in other modes. This work examined a previously less understood twinning mode, T2. A combination of SEM, EBSD and DAXM analysis illustrate the unique characteristics of T2 twinning, which is by no means similar with T1 twinning. Unlike prior work done using TEM, the broader area covered allowed a sequence of events to be proposed that leads to the nucleation and propagation of T2 twins, which was not understood before. The synergistic combination of different characterization techniques with an analysis approach from microscopic observation to atomic-scale processes can be used in future studies of other twinning modes.

There are two issues, if solved, could significantly extend the findings of this work.

First of all, strain transfer induced twin nucleation (S+T & T+T) only represents a fraction of the observed twins. More than half of the twins belong to 0+T, in which twins nucleated from grain boundaries where there is no apparent slip or twin activities on the opposite side. The defect source for these twin embryos to form is not known yet. Possible defect sources include pile-up

dislocations from the same grain, grain boundary dislocations, and dislocations from grains underneath. The difficulty for the analysis is that these defects are not as obvious as slip bands or twins in the SEM. TEM experiments or DAXM are necessary to analyze 0+T nucleation sites. To be able to include a 0+T grain boundary in the small TEM sample, the recently developed focused ion beam (FIB) technique might be used, which allows a targeted region of interest under the SEM image field to be cut directly from the bulk specimen to a thickness that is suitable for TEM characterization. Ten or even twenty 0+T instances need to be analyzed this way in order to draw a statistically meaningful conclusion.

The other issue to examine further is with the DAXM peak streak analysis. The current analysis strategy cannot reveal the dislocation content in the voxel if the peaks display strong curvature or streak in two distinct directions, which are the evidence of co-existing two (or more) sets of GNDs. The Nye's tensor method should still be useful, however, the major difficulty is that there are many possible combinations of two slip systems (for Ti, this number is 24×24=576), not to say that dislocations on each slip system may take edge, screw, or mixed orientation. A practical way to overcome this problem might be first analyzing nearby voxels that display straight peak streak (single set of GNDs). Once there are some clues about the slip plane and the Burgers vector of dislocations nearby, the number of possible slip systems to consider can be substantially reduced to examine how dislocations interact with each other and result in the complex-shaped diffraction peak in the voxel in question.

Chapter 9

Conclusions and Future Work

9.1 Conclusions

This dissertation examined the mesoscale conditions that will favor twin nucleation. It has been found that many twin nucleation events are essentially a form of strain transfer at grain boundaries. A strain transfer parameter, *m'*, is used to measure the likelihood for strain transfer to occur between two deformation systems on the two sides of a grain boundary. For a soft-hard grain pair, T1 twins are likely to form in the hard grain if it has a T1 twinning system that has a high *m'* with the active prismatic slip system in the soft grain — S+T. For a hard-hard grain pair with a small misorientation, paired twins can nucleate cooperatively from the same place on the grain boundary and propagate in opposite directions — T+T. In a specimen whose texture favors twinning, S+T and T+T can account for about half of the total observed twins. The magnitude of *m'* between the slip system and the twinning system in the case of S+T, and between the two twinning systems in the case of T+T, dictates whether such strain transfer induced twin nucleation events will occur.

DAXM is a new and effective technique to characterize subsurface microstructure and dislocations in bulk materials. Depending on the dimension of the beam scanning path (line scan or area scan), a 2D or 3D orientation map can be built underneath the surface. In deformed samples, local lattice rotations resulting from geometrically necessary dislocations leads to streaked diffraction peaks in many Laue patterns. This thesis proposed a simplified method to estimate the slip system of GNDs based on the direction of peak streak. The calculation results

using this simplified method agree with the more sophisticated Laue pattern simulation methodology established by R.I. Barabash and G.E. Ice at Oak Ridge National Laboratory. Using DAXM and peak streak analysis, it has been found that GNDs often accumulate near grain boundaries when slip transfer to the adjacent grain is difficult. GNDs, in most cases, are of edge type, though screw GNDs were identified in one example. If surface slip bands form in a grain, then subsurface GNDs are most likely either from the same slip system or from another slip system with the same Burgers vector.

This thesis also provides a comprehensive study of T2 twinning, a twinning mode that has been neglected by most researchers. T2 twins are almost exclusively nucleated by a generalized T+T mechanism (i.e. T1+T2 and T2+T2). This finding was attributed to the fact that a stable T2 twin embryo needs more twinning dislocations with larger Burgers vector than T1 twinning, and only T+T could provide so many defects in a short time. T2 twins usually do not grow very wide, which makes the activation of other slip or T1 twinning systems in the same grain to be necessary in order to accommodate the global strain. Interaction between T2 twins and neighboring slip and twinning activities makes the boundary of T2 twins often irregular. Kink bands, surface ledges, and microcracks are observed near some T2 twin boundaries. The <c+a> dislocations that have their Burgers vector parallel to the T2 twinning plane can continue glide in the twin lattice because their Burgers vector is unchanged in the twinning operation. Accumulation of <c+a> dislocations in the twin lattice can lead to large orientation gradient in the T2 twin. Taking all of these difficulties together, conditions are more favorable for developing a crack than with T1 twins.

9.2 Future Work

Some broadly defined potential research opportunities have already been discussed at the end of

Chapter 8, such as building 3D grain structure based on DAXM measurement, incorporating

strain transfer based twin nucleation into CPFEM, identifying other twin nucleation mechanisms,

etc. There are also some less ambitious studies that can be directly proposed from this thesis.

Some of them are currently under investigation.

One project is to simulate S+T using molecular dynamics (MD). Motion of individual

dislocations and reaction of the grain boundary during slip transfer can be observed at the atomic

level. It will be interesting to find out the least number of prismatic <a> dislocations that are

necessary to stimulate a stable twin embryo in the adjacent grain. Another possible trial is to

simulate some S+0 grain pairs. If the hard grain does not develop twins, how will it

accommodate the slip shear from the soft grain? This project is anticipated in collaboration with

Dr. Jian Wang at Los Alamos National Laboratory.

The second project is to identify a statistical correlation between *m'* and grain boundary ledges.

Ledges have been observed at some grain boundaries in our samples. Clearly, ledges are

evidence of shear incompatibility between two neighboring grains. In fact, a low *m'* was found

in a couple of ledges. More observations are needed to confirm this trend. CPFE simulations

made on microstructures with ledges have been analyzed using combination of a tensorial

measure of in-plane grain boundary deformation with localized mode-II shear stresses, in which

a new metric was developed that effectively and statistically distinguishes between ledge-

forming and topographically homogenous grain boundaries, a work that is in ongoing collaboration with Prof. Darren Mason.

A third project will use the established DAXM peak streak analysis method to investigate GNDs in other materials, such as Ti alloys and Nb. Ti alloy specimens loaded under high temperature show wavy slip lines, indicating cross slip. In these regions, one might observe DAXM peak streak coming from screw GNDs, as cross slip only happens for screw dislocations. Mixed type dislocations are also expected near the cross-slip regions. This work is continuing in an ongoing project as a part of Hongmei Li's Ph.D. research. Peaks streak analysis is also being used to study GNDs in single crystal Nb. These results will lead to clarification on activated slip systems in multi-slip conditions and single slip experiments on single crystals to help identify conditions where slip is not controlled by the Schmid factor alone. This effort is in conjunction with the Ph.D. research of Derek Baars, Aboozar Mapar, and Di Kang.

APPENDIX

APPENDIX

The following Matlab code is for simulating the Laue pattern in Figure 3.2(b). Grain orientation
of the voxel needs to be provided. In this example, $(\varphi_1, \Phi, \varphi_2) = (35°, 88°, 147°)$. The variable
ss is a 48 by 3 cell array. Each peak in the Laue pattern corresponds to a row in ss. For the jth
peak, ss{j, 1} and ss{j, 2}, are j and the 4-digit Miller index of the peak, respectively. The Miller
index of the jth peak is converted to a Cartesian system and stored in ss{j,3}. With the grain
orientation, the plane normal of jth peak in the sample coordinate system is calculated and stored
in rot_nA(j,:). In the DAXM experiment, the CCD screen is 45° from the sample surface, thus
rot_nA(j,:) needs to be further converted into the "CCD coordinate system" as pn_inCCD(j,:).
The X and Y components of the plane normal vector in the "CCD coordinate system" give the
position of the peak in the Laue pattern.

```
% Enter grain orientation by Bunge Euler angles
Euler=zeros(3,1);
Euler(1)=35;
Euler(2)=88;
Euler(3)=147;

% Calculate the rotation matrix, g, based on the Euler angles
phi1=Euler(1)*pi/180;
PHI=Euler(2)*pi/180;
phi2=Euler(3)*pi/180;
g1=[cos(phi1),sin(phi1),0;-sin(phi1),cos(phi1),0;0,0,1];
g2=[1,0,0;0,cos(PHI),sin(PHI);0,-sin(PHI),cos(PHI)];
g3=[cos(phi2),sin(phi2),0;-sin(phi2),cos(phi2),0;0,0,1];
g=g3*g2*g1;

% Define each peaks in the pattern
ss=cell(48,3);
% Miller indices of 13 peaks
```

```matlab
ss{1,2} = [3 -7 4 0];
ss{2,2} = [1 -2 1 0];
ss{3,2} = [2 -3 1 0];
ss{4,2} = [3 -4 1 0];
ss{5,2} = [4 -5 1 0];
ss{6,2} = [4 -7 3 -1];
ss{7,2} = [3 -5 2 -1];
ss{8,2} = [4 -6 2 -1];
ss{9,2} = [3 -7 4 1];
ss{10,2} = [2 -5 3 1];
ss{11,2} = [3 -6 3 2];
ss{12,2} = [3 -5 2 1];
ss{13,2} = [4 -6 2 1];

npeaks = 13; % number of peaks

c_a = 1.59;  % c/a ratio of Ti

% convert Miller index from hexagonal system to Cartesian system
for j=1:1:npeaks;
        n=[ss{j,2}(1,1),(ss{j,2}(1,2)*2+ss{j,2}(1,1))/3^.5,ss{j,2}(1,4)/c_a];
        mag_n=(n(1,1)^2+n(1,2)^2+n(1,3)^2)^0.5;
        unit_n = n/mag_n;
        ss{j,1} = j;
        ss{j,3} = [unit_n];

end

for j=1:1:npeaks
        % calculate plane normal in the sample coordinate system
        rot_nA(j,:) = (g'*ss{j,3}(1,:)')';

        % convert plane normal vector into "CCD coordinate system"
        pn_inCCD(j,:)=rot_nA(j,:)*[1 0 0;0 1/sqrt(2) -1/sqrt(2);0 1/sqrt(2) 1/sqrt(2)];
        reflection_inCCD(j,1)=2*pn_inCCD(j,2)*pn_inCCD(j,1);
        reflection_inCCD(j,2)=2*pn_inCCD(j,2)*pn_inCCD(j,2)-1;
        reflection_inCCD(j,3)=2*pn_inCCD(j,2)*pn_inCCD(j,3);
end

% Peak position in the CCD screen
Y=-reflection_inCCD(:,1);
X=-reflection_inCCD(:,2);  % X-scan "+ +" H-scan "- -"
plot(X,Y,'*');
hold on

% Label each peak by its Miller index
```

```
for j=1:1:npeaks
        text(X(j)+0.03,Y(j),num2str(ss{j,2}(:)'));
        hold on
end
axis([-0.5 0.5 -0.5 0.5])
```

This Matlab code is for calculating the theoretical peak streak direction for 24 slip systems in Ti at a given peak. The result is a "star pattern" such as in Figure 6.4. The grain orientation of the voxel needs to be provided. In this example, $(\varphi_1, \Phi, \varphi_2) = (16°, 109°, 315°)$. The variable ss is a 48 by 3 cell array. Each slip system corresponds to a row in ss. For the jth slip system ($1 \leq j \leq 24$), ss{j, 1} is the slip system number, j. ss{j, 2} stores the Miller indices of the slip plane and slip direction. These Miller indices are converted to a Cartesian system and stored in ss{j,3}. The plane normal and the Burgers vector in the sample coordinate system are calculated as rot_nA(j,:) and rot_bA(j,:). Nye's tensor for edge and screw type dislocations on jth slip system are calculated as Edge_Lab(:, :) and Screw_Lab(:, :). ξ is calculated by Equations 3.6 and 3.7.

```
% Enter grain orientation by Bunge Euler angles
Euler=zeros(3,1);
Euler(1)=16;
Euler(2)=109;
Euler(3)=315;

% Calculate the rotation matrix, g, based on the Euler angles
phi1=Euler(1)*pi/180;
PHI=Euler(2)*pi/180;
phi2=Euler(3)*pi/180;
g1=[cos(phi1),sin(phi1),0;-sin(phi1),cos(phi1),0;0,0,1];
g2=[1,0,0;0,cos(PHI),sin(PHI);0,-sin(PHI),cos(PHI)];
g3=[cos(phi2),sin(phi2),0;-sin(phi2),cos(phi2),0;0,0,1];
g=g3*g2*g1;

ss=cell(48,3);
%  basal <a>
ss{1,2} = [0 0 0 1; -2 1 1 0]; % slip plane and slip direction
ss{2,2} = [0 0 0 1; 1 -2 1 0];
ss{3,2} = [0 0 0 1; 1 1 -2 0];
%  prism <a>
ss{4,2} = [0 1 -1 0; -2 1 1 0];
ss{5,2} = [1 0 -1 0; 1 -2 1 0];
ss{6,2} = [-1 1 0 0; 1 1 -2 0];
%  pyramidal <a>
ss{7,2} = [0 1 -1 1; -2 1 1 0];
```

```matlab
ss{8,2} = [1 0 -1 1; 1 -2 1 0];
ss{9,2} = [-1 1 0 1; 1 1 -2 0];
ss{10,2} = [0 -1 1 1; -2 1 1 0];
ss{11,2} = [-1 0 1 1; 1 -2 1 0];
ss{12,2} = [1 -1 0 1; -1 -1 2 0];
% pyramidal <c+a>
ss{13,2} = [1 0 -1 1; 2 -1 -1 -3];
ss{14,2} = [1 0 -1 1; 1 1 -2 -3];
ss{15,2} = [0 1 -1 1; 1 1 -2 -3];
ss{16,2} = [0 1 -1 1; -1 2 -1 -3];
ss{17,2} = [-1 1 0 1; -1 2 -1 -3];
ss{18,2} = [-1 1 0 1; -2 1 1 -3];
ss{19,2} = [-1 0 1 1; -2 1 1 -3];
ss{20,2} = [-1 0 1 1; -1 -1 2 -3];
ss{21,2} = [0 -1 1 1; -1 -1 2 -3];
ss{22,2} = [0 -1 1 1; 1 -2 1 -3];
ss{23,2} = [1 -1 0 1; 1 -2 1 -3];
ss{24,2} = [1 -1 0 1; 2 -1 -1 -3];


% peak to be analyzed is (4, -5, 1, 4)
ss{25,2} = [4 -5 1 4; 0 0 0 0];


nss = 24;    % number of allowed slip systems


c_a = 1.59;  % c/a ratio of Ti


% convert Miller index from hexagonal system to Cartesian system
for j=1:1: (nss+1)
        n=[ss{j,2}(1,1),(ss{j,2}(1,2)*2+ss{j,2}(1,1))/3^.5,ss{j,2}(1,4)/c_a];
        m=[ss{j,2}(2,1)*1.5,3^.5/2*(ss{j,2}(2,2)*2+ss{j,2}(2,1)),ss{j,2}(2,4)*c_a];
        mag_n=(n(1,1)^2+n(1,2)^2+n(1,3)^2)^0.5;
        mag_m=(m(1,1)^2+m(1,2)^2+m(1,3)^2)^0.5;
        unit_n = n/mag_n;     % normalized plane normal vector
        unit_m = m/mag_m;     % normalized slip direction vector
        ss{j,1} = j;
        ss{j,3} = [unit_n;unit_m];
end

rot_nA=zeros(25,3);
rot_nA(25,:)=(g'*ss{25,3}(1,:)')';    % plane normal of the peak



p=1;
% lattice rotation tensor defined in the dislocation coordinate system: x->b, y->n, z->t
Edge_rot=[0 -p 0;p 0 0;0 0 0];
Screw_rot=[0 p/2 p/2;-p/2 0 -p/2;-p/2 p/2 0];
```

```matlab
for j=1:1:nss
    rot_bA(j,:) = (g'*ss{j,3}(2,:)')';     % Burgers vector in sample coordinate system
    rot_nA(j,:) = (g'*ss{j,3}(1,:)')';     % Slip plane normal in sample coordinate system
    rot_tA(j,:)=cross(rot_bA(j,:),rot_nA(j,:));     % Dislocation line direction

    DisTOLab(:,:)=[rot_bA(j,:);rot_nA(j,:);rot_tA(j,:)]; % Transformation matrix

    % Nye's tensor for edge dislocations on jth slip system
    Edge_Lab(:,:)=DisTOLab'*Edge_rot*DisTOLab;
    % Nye's tensor for screw dislocations on jth slip system
    Screw_Lab(:,:)=DisTOLab'*Screw_rot*DisTOLab;

    % Calculate the peak streak direction, ξ, for edge or screw dislocations
    ita(j,:)=(Edge_Lab(:,:)*rot_nA(25,:)')';
    %ita(j,:)=(Screw_Lab(:,:)*rot_nA(25,:)')';
end

for j=1:1:nss
    % convert ξ into "CCD coordinate system"
    ita(j,:)=ita(j,:)*[1 0 0;0 1/sqrt(2) -1/sqrt(2);0 1/sqrt(2) 1/sqrt(2)];
    Ita(j,:)=cross(ita(j,:),rot_nA(nss,:));  % project ξ to the CCD screen
    xita(j)=Ita(j,1);          %  x component of the streak
    yita(j)=-Ita(j,2);         %  ycomponent of the streak

    if j<=3  % basal slip systems are represented by dotted thick lines
        plot([0 xita(j)],[0,yita(j)],'k:','Linewidth', 1);
        hold on;
    elseif j<=6 % Prism slip systems are represented by solid thick lines
        plot([0 xita(j)],[0,yita(j)],'k','Linewidth', 2);
        hold on;
    else % Pyramidal slip systems are represented by solid thin lines
        plot([0 xita(j)],[0,yita(j)],'k','Linewidth', 1);
        hold on;
    end

    text(xita(j),yita(j),int2str(j), 'Fontsize', 16); % label slip system number
    hold on;
    title('Reflection (4 -5 1 4)', 'Fontsize', 16);  % show peak index as the figure title
end
axis ([-1,1,-1,1])
```

REFERENCES

171

REFERENCES

Alam M.N., Blackman M., Pashley D.W., 1954. High-angle Kikuchi patterns. Proc. R. Soc. A, 221, 224-242.

Adams B.L., Wright S.I., Kunze K., 1993. Orientation Imaging - The Emergence Of A New Microscopy. Metall. Trans. A. 24, 819-831.

Ahmed J., Roberts S.G., Wilkinson A.J., 2006. Characterizing dislocation structure evolution during cyclic deformation using electron channeling contrast imaging. Philos. Mag. 86, 4965-4981.

Arsenlis A., Parks D.M., 1999. Crystallographic aspects of geometrically-necessary and statistically-stored dislocation density. Acta Mater. 47, 1597-1611.

Asaro R.J., Needleman A., 1985. Texture development and strain-hardening in rate dependent polycrystals. Acta Metall. 33, 923-953.

Barabash R., Ice G.E., Larson B.C., Pharr G.M., Chung K.S., Yang W., 2001. White microbeam diffraction from distorted crystals. Appl. Phys. Lett. 79, 749-751.

Barabash R.I., Ice G.E., Walker F.J., 2003. Quantitative microdiffraction from deformed crystals with unpaired dislocations and dislocation walls. J. Appl. Phys. 93, 1457-1464.

Barabash R., Ice G., Liu W., Barabash O., 2009. Polychromatic microdiffraction characterization of defect gradients in severely deformed materials. Micron 40, 28-36.

Becker R., Panchanadeeswaran S., 1995. Effects of grain interactions on deformation and local texture in polycrystals. Acta Metall. Mater. 43, 2701-2719.

Beyerlein I.J., Tome C.N., 2008. A dislocation-based constitutive law for pure Zr including temperature effects. Int. J. Plasticity 24, 867-895.

Beyerlein I.J., Tome C.N., 2010a. A probabilistic twin nucleation model for HCP polycrystalline metals. Proc. R. Soc. A 466, 2517-2544.

Beyerlein I.J., Capolungo L., Marshall P.E., McCabe R.J., Tome C.N., 2010b. Statistical analyses of deformation twinning in magnesium. Philos. Mag. 90, 2161-2190.

Bhattacharyya D., Cerreta E.K., McCabe R., Niewczas M., Gray G.T., Misra A., Tome C.N., 2009. Origin of dislocations within tensile and compressive twins in pure textured Zr. Acta Mater. 57, 305-315.

Bieler T.R., Eisenlohr P., Roters F., Kumar D., Mason D.E., Crimp M.A., Raabe D., 2009. The role of heterogeneous deformation on damage nucleation at grain boundaries in single phase metals. Int. J. Plasticity 25, 1655-1683.

Bieler T.R., Crimp M.A., Yang Y., Wang L., Eisenlohr P., Mason D.E., Liu W., Ice G.E., 2009. Strain Heterogeneity and Damage Nucleation at Grain Boundaries during Monotonic Deformation in Commercial Purity Titanium. JOM 61, 45-52.

Bingert J.F., Mason T.A., Kaschner G.C., Maudlin P.J., Gray G.T., 2002. Deformation twinning in polycrystalline Zr: Insights from electron backscattered diffraction characterization. Metall. Mater. Trans. A. 33, 955-963.

Booker G.R., Shaw A.M.B., Whelan M.J., Hirsch P.B., 1967. Some comments on interpretation of kikuchi-like reflection patterns observed by scanning electron microscopy. Philos. Mag. 16, 1185-1191.

Bozzolo N., Chan L.S., Rollett A.D., 2010. Misorientations induced by deformation twinning in titanium. J. Appl. Crystallogr. 43, 596-602.

Bridier F., Villechaise P., Mendez J., 2005. Analysis of the different slip systems activated by tension in a α/β titanium alloy in relation with local crystallographic orientation. Acta Mater. 53, 555-567.

Bronkhorst C.A., Kalidindi S.R., Anand L., 1992. Polycrystalline plasticity and the evolution of crystallographic texture in fcc metals. Philos. Trans. R. Soc. Lond. Ser. A 341, 443-477.

Bunge H.J., Wenk H.R., Pannetier J., 1982. Neutron-diffraction texture analysis using a 2-theta-position sensitive detector. Textures and microstructures. 5, 153-170.

Bunge, H.J., 1983. Texture Analysis in Materials Science: Mathematical Methods. Butterworth, London.

Calcagnotto M., Ponge D., Demir E., Raabe D., 2010. Orientation gradients and geometrically necessary dislocations in ultrafine grained dual-phase steels studied by 2D and 3D EBSD. Mater. Sci. Eng. A 527, 2738-2746.

Capolungo L., Beyerlein I.J., 2008. Nucleation and stability of twins in HCP metals. Phys. Rev. B 78, 024117.

Capolungo L., Beyerlein I.J., Tome C.N., 2009a. Slip-assisted twin growth in hexagonal close-packed metals. Scripta Mater. 60, 32-35.

Capolungo L., Marshall P.E., McCabe R.J., Beyerlein I.J., Tomé C.N., 2009b. Nucleation and growth of twins in Zr: A statistical study. Acta Mater. 57, 6047-6056.

Coates D.G., 1967. Kikuchi-like reflection patterns obtained with scanning electron microscope. Philos. Mag. 16, 1179-1184.

Christian J.W., Mahajan S., 1995. Deformation Twinning. Prog. Mater. Sci. 39, 1-157.

Chun Y., Yu S., Semiatin S., Hwang S., 2005. Effect of deformation twinning on microstructure and texture evolution during cold rolling of CP-Titanium. Mater. Sci. Eng. A 398, 209-219.

Crimp M.A., Simkin B.A., Ng B.C., 2001. Demonstration of the g·b×u=0 edge dislocation invisibility criterion for electron channeling contrast imaging. Philos. Mag. Lett. 81, 833-837.

Crimp M.A., 2006. Scanning electron microscopy imaging of dislocations in bulk materials, using electron channeling contrast. Micros. Res. Tech. 69, 374-381.

Davidson D.L., Tryon R.G., Oja M., Matthews R., Ravi Chandran K.S., 2007. Fatigue Crack Initiation In WASPALOY at 20 °C. Metall. Mater. Trans. A 38, 2214-2225.

Delaire F., Raphanel J.L., Rey C., 2000. Plastic heterogeneities of a copper multicrystal deformed in uniaxial tension: Experimental study and finite element simulations. Acta Mater. 48, 1075-1087.

Delannay L., Loge R.E., Chastel Y., Signorelli J.W., Van Houtte P., 2003. Measurement of in-grain orientation gradients by EBSD and comparison with finite element results. Adv. Eng. Mater. 5, 597-600.

Demir E., Raabe D., Zaafarani N., Zaefferer S., 2009. Investigation of the indentation size effect through the measurement of the geometrically necessary dislocations beneath small indents of different depths using EBSD tomography. Acta Mater. 57, 559-569.

Dingley D.J., Babakishi K., 1986. Use of electron back scatter diffraction patterns for determination of crystal symmetry elements. Scan. Electron Micros. 2, 383-391.

Dingley D.J., Randle V., 1992. Microtexture determination by electron back-scatter diffraction. J. Mater. Sci. 27, 4545-4566.

Dunne F.P.E., Walker A., Rugg D., 2007. A systematic study of hcp crystal orientation and morphology effects in polycrystal deformation and fatigue. P. Roy. Soc. Lon. A 463, 1467-1489.

El-Danaf E., Kalidindi S.R., Doherty R.D., 1999. Influence of grain size and stacking-fault energy on deformation twinning in fcc metals. Metall. Mater. Trans. A 30, 1223-1233.

Fundenberger J.J., Philippe M.J., Wagner F., Esling C., 1997. Modeling and prediction of mechanical properties for materials with hexagonal symmetry (zinc, titanium and zirconium alloys). Acta Mater. 45, 4041-4055.

Goldstein J.I., Newbury D.E., Echlin P., Joy D.C., Lyman C.E., Lifshin E., Sawyer L., Michael J.R., 2003. Scanning Electron Microscopy and X-Ray Microanalysis (3rd Edition). Springer, New York.

Gutierrez-Urrutia I., Zaefferer S., Raabe D., 2009. Electron channeling contrast imaging of twins and dislocations in twinning-induced plasticity steels under controlled diffraction conditions in a scanning electron microscope. Scripta Mater. 61, 737-740.

Heinz A., Neumann P., 1991. Representation of orientation and disorientation data for cubic, hexagonal, tetragonal and orthorhombic crystals. Acta Crystallogr. A 47, 780-789.

Hirsch P.B., Howie H., Nicholson R.B., Pashley D.W., Whelan M.J., 1965. Electron microscopy of thin crystals. Butterworths, London.

Hirth J.P., Lothe J., 1982. Theory of Dislocations. John Wiley & Sons, New York.

Hook R.E., Hirth J.P., 1967. The deformation behavior of isoaxial bicrystals of Fe-3% Si. Acta Metall. 15, 535-551.

Hook R.E., Hirth J.P., 1967. The deformation behavior of non-isoaxial bicrystals of Fe-3% Si. Acta Metall. 15, 1099-1100.

Hull D., Bacon D.J., 2001. Introduction to Dislocations (4th Edition). Elsevier, Oxford.

Ice G.E., Barabash R.I., 2007. White beam Microdiffraction and dislocations gradients. Dislocations in Solids, vol 13, Chapter 79, 500-601.

Inokuti Y., Doherty R.D., 1977. Transmission Kossel study of the structure of cold-rolled iron and its nucleation behavior. Texture of Crystalline Solids 2, 143-168.

Jin Z.H., Gumbsch P., Ma E., Albe K., Lu K., Hahn H., Gleiter H., 2006. The interaction mechanism of screw dislocations with coherent twin boundaries in different face-centred cubic metals. Scripta Mater. 54, 1163-1168.

Joy D.C., Newbury D.E., Davidson D.L., 1982. Electron channeling patterns in the scanning electron-microscope. J. Appl. Phys. 53, R81-R122.

Kaganer V.M., Kohler R., Schmidbauer M., Opitz R., Jenichen B., 1997. X-ray diffraction peaks due to misfit dislocations in heteroepitaxial structures. Phys. Rev. B 55, 1793-1810.

Kalidindi S.R., Bronkhorst C.A., Anand L., 1992. Crystallographic texture evolution in bulk deformation processing of fcc metals. J. Mech. Phys. Solids 40, 537-569.

Kalidindi S.R., Bhattacharyya A., Doherty R.D., 2004. Detailed analyses of grain-scale plastic deformation in columnar polycrystalline aluminum using orientation image mapping and crystal plasticity models. Proc. R. Soc. London Ser. A-Math. Phys. Eng. Sci. 460, 1935-1956.

Kaschner G.C., Tome C.N., Beyerlein I.J., Vogel S.C., Brown D.W., McCabe R.J., 2006. Role of twinning in the hardening response of zirconium during temperature reloads. Acta Mater. 54, 2887-2896.

Kocks U.F., 1970. Relation between Polycrystal Deformation and Single-Crystal Deformation. Metall. Trans. 1, 1121-1143.

Kocks U.F., Tome C.N., Wenk H.R., 1998. Texture and Anisotropy. Cambridge University Press, Cambridge.

Kumar D., Bieler T.R., Eisenlohr P., Mason D.E., Crimp M.A., Roters F., Raabe D., 2008. On predicting nucleation of microcracks due to slip-twin interactions at grain boundaries in duplex near γ-TiAl. J. Eng. Mater. Tech. 130, 021012.

Krivoglaz M.A., 1996. Theory of x-ray and neutron scattering in nonideal crystals. Berlin: Springer-Verlag.

Larson B.C., Yang W., Ice G.E., Budai J.D., Tischler J.Z., 2002. Three-dimensional X-ray structural microscopy with submicrometre resolution. Nature 415, 887-890.

Lebensohn R.A., Tome C.N., 1993. A self-consistent anisotropic approach for the simulation of plastic-deformation and texture development of polycrystals - application to zirconium alloys. Acta Metall. Mater. 41, 2611-2624.

Li B., Ma E., 2009. Atomic Shuffling Dominated Mechanism for Deformation Twinning in Magnesium. Phys. Rev. Lett. 103, 035503.

Liu W.J., Ice G.E., Larson B.C., Yang W.G., Tischler J.Z., Budai J.D., 2004. The three-dimensional X-ray crystal microscope: A new tool for materials characterization. Metall. Mater. Trans. A 35, 1963-1967.

Liu W., Ice G., Larson B., Yang W., Tischler J., 2005. Nondestructive three-dimensional characterization of grain boundaries by X-ray crystal microscopy. Ultramicroscopy 103, 199-204.

Lu L., Shen Y.F., Chen X.H., Qian L.H., Lu K., 2004. Ultrahigh strength and high electrical conductivity in copper. Science 304, 422-426.

Lu L., Chen X., Huang X., Lu K., 2009. Revealing the maximum strength in nanotwinned Copper. Science 323, 607-610.

Luster J., Morris M.A., 1995. Compatibility of deformation in 2-phase ti-al alloys - dependence on microstructure and orientation relationships. Metall. Mater. Trans. A 26, 1745-1756.

Ma A., Roters F., Raabe D., 2006a. A dislocation density based constitutive model for crystal plasticity FEM including geometrically necessary dislocations. Acta Mater. 54, 2169-2179.

Ma A., Roters F., Raabe D., 2006b. On the consideration of interactions between dislocations and grain boundaries in crystal plasticity finite element modeling - Theory, experiments, and simulations. Acta Mater. 54, 2181-2194.

Maass R., Van Petegem S., Van Swygenhoven H., Derlet P.M., Volkert C.A., Grolimund D., 2007. Time-resolved Laue diffraction of deforming micropillars. Phys. Rev. Lett. 99, 145505.

Mahajan S., Chin G.Y., 1974. Interaction of twins with existing substructure and twins in cobalt-iron alloys. Acta Metall. 22, 1113-1119.

Meyers M.A., Vohringer O., Lubarda V.A., 2001. The onset of twinning in metals: A constitutive description. Acta Mater. 49, 4025-4039.

Mills D.M., 2002. Third-Generation Hard X-ray Synchrotron Radiation Sources: Source Properties, Optics, and Experimental Techniques. John Wiley and Sons.

Mises R. von, 1928. Mechanik der plastischen Formänderung von Kristallen. Z. Angew. Math. Mech., 8(3), 161-185.

Mishra S.K., Pant P., Narasimhan K., Rollett A.D., Samajdar I., 2009. On the widths of orientation gradient zones adjacent to grain boundaries. Scripta Mater. 61, 273-276.

Musienko A., Tatschl A., Schmidegg K., Kolednik O., Pippan R., Cailletaud G., 2007. Three-dimensional finite element simulation of a polycrystalline copper specimen. Acta Mater. 55, 4121-4136.

Ng B.C., Simkin B.A., Crimp M.A., 1998. Application of the electron channeling contrast imaging technique to the study of dislocations associated with cracks in bulk specimens. Ultramicroscopy 75, 137-145.

Niewczas M., 2010. Lattice correspondence during twinning in hexagonal close-packed crystals. Acta Mater. 58, 5848-5857.

Nowell M.M, Sabourin M.C., Carpenter J.O., 2006. Recent Advances in High-Speed Orientation Mapping. Microscopy Today. 14 (6), 6-9.

Nye J.F., 1953. Some geometrical relations in dislocated crystals. Acta Metall. 1, 153-162.

Ohashi T., Barabash R.I., Pang J.W.L., Ice G.E., Barabash O.M., 2009. X-ray microdiffraction and strain gradient crystal plasticity studies of geometrically necessary dislocations near a Ni bicrystal grain boundary. Int. J. Plasticity 25, 920-941.

Orowan E., 1934. Zur Kristallplastizität. III. Z. Phys., 89, 634-659.

Polanyi M., 1934. Über eine Art Gitterstörung, die einen Kristall plastisch machen könnte. Z. Phys. 89, 660-664.

Pantleon W., 2008. Resolving the geometrically necessary dislocation content by conventional electron backscattering diffraction. Scripta Mater. 58, 994-997.

Raabe D., Sachtleber M., Zhao Z., Roters F., Zaefferer S., 2001. Micromechanical and macromechanical effects in grain scale polycrystal plasticity experimentation and simulation. Acta Mater. 49, 3433-3441.

Raabe D., Zhao Z., Park S.J., Roters F., 2002. Theory of orientation gradients in plastically strained crystals. Acta Mater. 50, 421-440.

Raabe D., Roters F., 2004. Using texture components in crystal plasticity finite element simulations. Int. J. Plasticity 20, 339-361.

Reed-Hill R.E., Hartt W.H., Slippy W.A., 1968. Double accommodation kinking and growth of {11-21} Twins in Zirconium. Trans. TMS-AIME 242, 2211-2215.

Reddy J.N., 2008. An Introduction to Continuum Mechanics. Cambridge University Press, New York.

Roters F., Eisenlohr P., Hantcherli L., Tjahjanto D.D., Bieler T.R., Raabe D., 2010. Overview of constitutive laws, kinematics, homogenization and multiscale methods in crystal plasticity finite-element modeling: Theory, experiments, applications. Acta Mater. 58, 1152-1211.

Roters F., Eisenlohr P., Bieler T.R., Raabe D., 2010. Crystal Plasticity Finite Element Methods: in Materials Science and Engineering, Wiley-VCH, Weinheim.

Sachs G., 1928. On the derivation of a condition of flowing. Z. Ver. Dtsch. Ing. 72, 734-736.

Salem A.A., Kalidindi S.R., Doherty R.D., 2003. Strain hardening of titanium: role of deformation twinning. Acta Mater. 51, 4225-4237.

Salem A.A, Kalidindi S.R, Semiatin S.L, 2005. Strain hardening due to deformation twinning in α-titanium: Constitutive relations and crystal-plasticity modeling. Acta Mater. 53, 3495-3502.

Schmidt N.H., Olesen N.O., 1989. Computer-aided determination of crystal-lattice orientation from electron-channeling patterns in the sem. Can. Mineral. 27, 15-22.

Serra A., Bacon D.J., 1996. A new model for {1012} twin growth in hcp metals. Philos. Mag. A 73, 333-343.

Serra A., Bacon D.J., Pond R.C., 1999. Dislocations in interfaces in the hcp metals - I. Defects formed by absorption of crystal dislocations. Acta Mater. 47, 1425-1439.

Serra A., Bacon D.J., Pond R.C., 2002. Twins as barriers to basal slip in hexagonal-close-packed metals. Metall. Mater. Trans. A 33, 809-812.

Serra A., Bacon D.J., Pond R.C., 2010. Comment on "Atomic Shuffling Dominated Mechanism For Deformation Twinning In Magnesium". Phys. Rev. Lett. 104, 029603.

Simkin B.A., Crimp M.A., 1999. An experimentally convenient configuration for electron channeling contrast imaging. Ultramicroscopy 77, 65-75.

Simkin B.A., Crimp M.A., Bieler T.R., 2003. A factor to predict microcrack nucleation at gamma-gamma grain boundaries in TiAl. Scripta Mater. 49, 149-154.

Simkin B.A., Ng B.C., Crimp M.A., Bieler T.R., 2007. Crack opening due to deformation twin shear at grain boundaries in near-gamma TiAl. Intermetallics 15, 55-60.

Schulson E.M., 1977. Electron channeling patterns in scanning electron-microscopy. J. Mater. Sci. 12, 1071-1087.

Schwarz A.J., Kumar M., Field D.P., Adams B.L., 2000. Electron Backscatter Diffraction in Materials Science. Springer, New York.

Schwarzer R.A., Hjelen J., 2010. Orientation microscopy with fast EBSD. Mater. Sci. Technol. 26, 646-649.

Shapiro L.G., Stockman G.C., 2001. Computer Vision. Prentice Hall.

Sleeswyk A.W., 1962. Emissary dislocations - theory and experiments on propagation of deformation twins in alpha-iron. Acta Metall. 10, 705-725.

Song S.G., Gray G.T., 1995a. Structural interpretation of the nucleation and growth of deformation twins in Zr and Ti. Part 1. Application of the coincidence site lattice (CSL) theory to twinning problems in hcp structures. Acta Metall. Mater. 43, 2325-2337.

Song S.G., Gray G.T., 1995b. Structural interpretation of the nucleation and growth of deformation twins in Zr and Ti. Part 2. TEM study of twin morphology and defect reactions during twinning. Acta Metall. Mater. 43, 2339-2350.

Stanford N., Carlson U., Barnett M.R., 2008a. Deformation twinning and the Hall-Petch relation in commercial purity Ti. Metall. Mater. Trans. A 39, 934-944.

Stanford N., 2008b. Observation of {1121} twinning in a Mg-based alloy. Philos. Mag. Lett. 88, 379-386.

Staroselsky A., Anand L., 2003. A constitutive model for hcp materials deforming by slip and twinning: application to magnesium alloy AZ31B. Int. J. Plasticity 19, 1843-1864.

Tan X., Gu H., Laird C., Munroe N.D.H., 1998. Cyclic deformation behavior of high-purity titanium single crystals: Part I. Orientation dependence of stress-strain response. Metall. Mater. Trans. A 29, 507-512.

Taylor G.I., 1934. The Mechanism of Plastic Deformation of Crystals. Part I. Theoretical. Proc. Roy. Soc. A. 145, 362-387.

Thompson N., Millard D.J., 1952. Twin formation in Cadmium. Philos. Mag. 43, 422-440.

Tome C.N., Maudlin P.J., Lebensohn R.A., Kaschner G.C., 2001. Mechanical response of zirconium - I. Derivation of a polycrystal constitutive law and finite element analysis. Acta Mater. 49, 3085-3096.

Vaidya S., Mahajan S., 1980. Accommodation and formation of (1121) twins in Co single-crystals. Acta Metall. 28, 1123-1131.

Venables J.A., Harland C.J., 1973. Electron backscattering patterns - new technique for obtaining crystallographic information in scanning electron-microscope. Philos. Mag. 27, 1193-1200.

Venables J.A., Binjaya R., 1977. Accurate micro-crystallography using electron backscattering patterns. Philos. Mag. 35, 1317-1332.

Wagenknecht B., Libiran D., Poon S., Sztykiel K., 2008. In-situ Four-Point Bending Apparatus for Scanning Electron Microscopes (Senior Design Project, Mechanical Engineering, Michigan State University).

Wang J., Hirth J.P., Tomé C.N., 2009a. (-1012) Twinning nucleation mechanisms in hexagonal-close-packed crystals. Acta Mater. 57, 5521-5530.

Wang J., Hoagland R.G., Hirth J.P., Capolungo L., Beyerlein I.J., Tomé C.N., 2009b. Nucleation of a (-1012) twin in hexagonal close-packed crystals. Scripta Mater. 61, 903-906.

Wang J., Beyerlein I.J., Tome C.N., 2010. An atomic and probabilistic perspective on twin nucleation in Mg. Scripta Mater. 63, 741-746.

Wang L., Yang Y., Eisenlohr P., Bieler T.R., Crimp M.A., Mason D.E., 2010a. Twin Nucleation by Slip Transfer across Grain Boundaries in Commercial Purity Titanium. Metall. Mater. Trans. A 41, 421-430.

Wang L., Eisenlohr P., Yang Y., Bieler T.R., Crimp M.A., 2010b. Nucleation of paired twins at grain boundaries in titanium. Scripta Mater. 63, 827-830.

Wang L., Barabash R.I., Yang Y., Bieler T.R., Crimp M.A., Eisenlohr P., Liu W., Ice G.E., 2011. Experimental characterization and crystal plasticity modeling of heterogeneous deformation in polycrystalline α-Ti. Metall. Mater. Trans. A 42, 626-635.

Williams D.B., Carter C.B., 1996. Transmission Electron Microscopy. Plenum Press, New York.

Williams J.C., Baggerly R.G., Paton N.E., 2002. Deformation behavior of HCP Ti-Al alloy single crystals. Metall. Mater. Trans. A, 33, 837-850.

Wright S., Nowell M., 2008. High-speed EBSD. Adv. Mater. Process. 166, 29-31.

Wu X., Kalidindi S., Necker C., Salem A., 2007. Prediction of crystallographic texture evolution and anisotropic stress–strain curves during large plastic strains in high purity α-titanium using a Taylor-type crystal plasticity model. Acta Mater. 55, 423-432.

Yang Y., Wang L., Bieler T.R., Eisenlohr P., Crimp M.A., 2011. Quantitative Atomic Force Microscopy Characterization and Crystal Plasticity Finite Element Modeling of Heterogeneous Deformation in Commercial Purity Titanium. Metall. Mater. Trans. A 42, 636-644.

Yoo M.H., 1981. Slip, twinning, and fracture in hexagonal close-packed metals. Metall. Mater. Trans. A 12, 409-418.

Yoo M.H., Morris J.R., Ho K.M., Agnew S.R., 2002. Nonbasal deformation modes of HCP metals and alloys: Role of dislocation source and mobility. Metall. Mater. Trans. A 33, 813-822.

Yu Q., Shan Z.W., Li J., Huang X.X., Xiao L., Sun J., Ma E., 2010. Strong crystal size effect on deformation twinning. Nature 463, 335-338.

Zaefferer S., 2003. A study of active deformation systems in titanium alloys: dependence on alloy composition and correlation with deformation texture. Mater. Sci. Eng. A. 344, 20-30.

Zaefferer S., Wright S.I., Raabe D., 2008. Three-Dimensional Orientation Microscopy in a Focused Ion Beam Scanning Electron Microscope: A New Dimension of Microstructure Characterization. Metall. Mater. Trans. A 39, 374-389.